Lehrstuhl für Elektrische Antriebssysteme und Leistungselektronik
der Technischen Universität München

The Performance Improvements of Self-sensing Control for Permanent Magnet Synchronous Machines

Xiaocan Wang

Vollstaendiger Abdruck der von der Fakultät für Elektrotechnik und Informationstechnik der Technischen Universität München zur Erlangung des akademischen Grades eines

Doktor-Ingenieurs

genehmigten Dissertation.

Vorsitzender: Univ.-Prof. Dr.-Ing. Hans-Georg Herzog
Prüfer der Dissertation:
1. Univ.-Prof. Dr.-Ing. Ralph M. Kennel
2. Univ.-Prof. Dr.-Ing. Dieter Gerling
Universität der Bundeswehr München

Die Dissertation wurde am 30.09.2014 bei der Technischen Universität München eingereicht und durch die Fakultät für Elektrotechnik und Informationstechnik am 03.02.2015 angenommen.

Acknowledgments

This dissertation is a cumulative work involving the contributions of many people. Without their support, this dissertation would not have come to completion. This research work has been carried out during the years 2010-2014 in the Institute for Electrical Drive Systems and Power Electronics, Technical University of Munich. First, I would like to express my sincere thanks to my supervisor, Prof. Dr.-Ing. Ralph M. Kennel, for his valuable comments and guidance throughout the work as well as for allowing me a high degree of freedom in my research activities. His inspiring guidance and encouragement have been of enormous significance to me.

I am indebted to my another advisor, Prof. Robert D. Lorenz, for the opportunities and guidance that he has given. His unselfish support and training have greatly enhanced my skills in almost every aspect of my professional life. I have truly enjoyed my time at WEMPEC, University of Wisconsin-Madison in November 2013. Many brilliant people including, Wei, Chen-Yun, Larry and Kang as well as the other students have made it a pleasure to learn and work there.

I am appreciate the help of Prof. Dr.-Ing. Dieter Gerling in University of Federal Defense Munich, that he is very kind to provide the lab equipments of the Department of Electrical Drives and Actuators free to me. He gives us the permission to enable the collaboration and also pays much attention about my doctoral thesis.

In addition, I wish to send my warmest thanks to Peter, Fengxiang, Zhixun, Dr. Gao, Dr. Dajaku and all our EAL and EAA team members during these years, for their close co-operation, for making the time spent in Munich worthwhile and help in every day life.

The financial support of the Chinese Council Scholarship is gratefully acknowledged.

I am deeply indebted to my big family for giving me all best for a good life basis and encouraged me during my work. The help of my mother taking care of my son make my Ph.D research work to be continued on. Finally, I would like to thank my husband Wei for his love, understanding and support, and our lovely son Leon for his big smiles.

Abstract

This thesis presents a general solution for the problem of position self-sensing with surface-mounted permanent magnet synchronous machines at zero and low speeds using high frequency signal injection, and introduces two different novel designs of interior permanent magnet synchronous machines with concentrated windings which are attractive to the self-sensing control system and have been verified by respective experimental results. Furthermore, considering the efficiency optimization, the extra losses in a permanent magnet synchronous machine resulting from the high frequency injection are analyzed. By using the proposed observer-based model predictive torque control scheme, the closed-loop self-sensing technology of a permanent magnet synchronous machine can be achieved.

Kurzzusammenfassung

Diese Arbeit zeigt eine funktionsfähige Lösung für die Geberlose Positionserfassung bei niedrigen Drehzahlen und im Stillstand für permanenterregte Synchronmaschinen mit Oberflächenmagneten mit Hilfe der Einspeisung hochfrequenter Signale. Zwei unterschiedliche neuartige Maschinendesigns von Synchronmaschinen mit vergrabenen Magneten und konzentrierten Wicklungen die für die Geberlose Regelung geeignet sind wurden vermessen. Weiterhin wurden die zusätzlichen Verluste, die in der permanenterregten Synchronmaschine aufgrund der hochfrequenten Signale entstehen analysiert mit dem Ziel der Wirkungsgradoptimierung. Durch die vorgestellte Methode der modellprädiktiven Drehmomentregelung wird ein Geberlose Regelung für die permanenterregte Synchronmaschine realisiert, die auf einem Beobachter basierend.

Contents

CHAPTER 1

Introduction

1.1 Background

Permanent magnet synchronous machines (PMSMs) are widely used in low and medium power applications such as computer peripheral equipments, robotics, adjustable speed drives and electric vehicles. PMSMs have numerous advantages in comparison to other machines that are conventionally used for AC motor drives. The stator current of the induction machines contains magnetizing as well as torque-producing components. The use of permanent magnets in the rotor of PMSMs makes it unnecessary to supply magnetizing current through the stator for constant air-gap flux, and the stator current is only needed to produce the torque. Hence for the same torque output, PMSMs will operate at a higher power factor (because of the absence of magnetizing current), and will be more efficient than induction machines. The development of PMSMs aims to remove the foregoing disadvantages of the excited synchronous machines by replacing the field coils, DC power supply and slip rings with the permanent magnet [1] [2].

Control strategies of electrical machines are the key points of high-performance servo-drive systems. Since PMSMs are widely used in industrial applications, the control system of PMSMs has become a focus research topic for the last decades [3].

Nowadays the control performance of the electric drives still has space of improvements [4]. The traditional control methods field-oriented control (FOC) and direct torque control (DTC) are the most popular high-performance control strategies, and position sensors such as the resolver or the absolute encoder are required in the high-performance electric drive system in order to determine the rotor position. However, in industrial applications, the presence of such a position encoder

reveals several disadvantages in the areas of cost, reliability, machine size, and noise interference. Therefore, there has been much research on eliminating the position encoder mounted to the rotor of the electric machines by obtaining the rotor position information indirectly. This control method without a position sensor in the electric drives is called sensorless control, and is named as self-sensing control in this thesis, i.e. using the motor itself as the sensor [5].

Self-sensing control methods can be divided into three categories:

- Based on the back electromotive force (back-EMF) or extended EMF methods;
- Based on the mathematical models of electrical machines using state observers;
- Based on the high-frequency (HF) injection.

The self-sensing control with HF injection method shows good rotor position/speed estimation results at zero & low speed [6] [7]. The HF injection signal (current or voltage) is superimposed to the fundamental excitation. The applied signals interact with the rotor saliency or magnetic anisotropy of the motor, and the resulting response (voltage or current) is tracked to extract rotor position information.

Self-sensing control methods are applied in only a small fraction of all motor drive and actuator applications. A lot of schemes and concepts for self-sensing AC drive control providing good operation during standstill are already published in [8] [9] [10] [11] [12]. Acceptance by industry, however, is not very extended. The main reasons for hesitations in industry are enhanced processing performance being necessary for the controller or signal processor additional sensors or hardware parameters to be adjusted with respect to self-sensing control.

Self-sensing control of different kinds of PMSMs in the whole speed range is still a challenge [13]. The industry is concerned regarding about the excellent performance of the self-sensing control at each operation point [14] [15] [16] [17]. The estimated position and speed need to be very accurate in some areas, such as the aircraft industry, textile industry and so on.

Self-sensing control of PMSMs is attractive for the industry communities since the additional encoder can be relieved from the rotor, which is a kind of modern electrical drive systems. More than half of the electrical energy provided is used to produce mechanical motion by electric drives. Unfortunately, most of these drives are based on old technology and dissipate 25% to 40% of the supplied energy which could be saved by modern electrical drive systems and power electronics. This shows the importance and significance of the efficiency optimization of the electric drives using modern control methods. However, for the self-sensing control of

PMSMs based on the HF injection method, there are some extra losses due to the injection signals. How to make a balance between the cost of the position encoder and the extra losses consumption is a new topic for the modern industry. The losses in PMSMs resulting from the HF injection are need to be researched.

1.2 Contributions

In this thesis, the mainly two types of PMSMs: surface-mounted permanent magnet synchronous machines (SPMSMs) and interior permanent magnet synchronous machines (IPMSMs) are investigated and analyzed. In order to realize the self-sensing control of PMSMs in the whole speed range, HF injection method is used at zero & very low speed, and the observer-based self-sensing model predictive torque control method is implemented at medium and high speed.

The SPMSMs do not have the saliency phenomena in their geometry resulting in difficulties to implement the sailency-tracking self-sensing control strategies. Commercial SPMSM has been adapted for self-sensing applications by using the rotating and pulsating HF voltage vector injection methods. The experimental results verify that the SPMSM can reach very high performance with good self-sensing properties regarding the accuracy of the estimated position/speed of electric drives.

The IPMSMs have highlights due to the geometric saliency especially for the self-sensing control based on HF injection method. Two different novel designs of IPMSMs with concentrated windings (CW-IPMSMs) having lower space harmonic contents are tested and analyzed. Based on the machine design and HF injection self-sensing control method, the investigation insight the advantages and future application of the new designed CW-IPMSMs, which are essential and have not been done before. On the machine design side, these two novel designed machines have been proven to have lower losses even when including the eddy current losses. On the control performance side, it has been analyzed that HF current responses of PMSMs, with and without considering eddy current effects, are significantly different. Thus, due to the significant eddy current loss reduction, it is a promising topic to apply the self-sensing method for the new machines in order to get the optimal efficiency and control performance of the electric drives.

Considering the efficiency optimization, the losses in IPMSMs resulting from the HF injection for the self-sensing control are analyzed. The conventional losses calculation is mainly based on the finite element method (FEM), which are exhausted time consuming. A analytical solution is proposed to design the eddy current loss model. This technology can be used both with and without the HF injection in the machine, and also is meaningful when the machine is operated under extra high

speed.

When the machines are operated under medium and high speed, the back-EMF which is proportional to the speed can be utilized to do the position & speed estimation. The self-sensing control method of IPMSMs is implemented by the enhanced Luenberger-style back-EMF tracking observer. Furthermore, the self-sensing control strategy is based on the model predictive control with finite control set (FCS-MPC), and the Gopinath-style stator flux linkage observer is used to do the flux estimation which has not been done before.

CHAPTER 2

The State-of-the-Art Review

2.1 Overview of Permanent Magnet Synchronous Machines

Permanent magnet synchronous machines (PMSMs) have been widely used in various motion control applications. To maximize the power conversion performance, PMSMs need a systematic design. The objective of this section is to initiate a general review of PMSMs. PMSMs mainly can be classified into two types: surface-mounted permanent magnet synchronous machines (SPMSMs) and interior permanent magnet synchronous machines (IPMSMs). The general topologies of SPMSMs and IPMSMs are shown in Fig. 2.1. Usually, IPMSMs are used for high speed application because of the reluctance torque, and also for big torque response application because the high permanent-magnets mechanical strength; SPMSMs are used for constant speed application because of the smooth air-gap flux density [18].

2.1.1 Surface-mounted PMSMs

The simplest and probably the cheapest rotor construction of PMSMs can be obtained by using surface-mounted permanent magnets [20]. The SPMSM is also the most commonly used model nowadays. Most motors for servo drives are SPMSMs. The armature reaction of this machine type is remarkably small, and the magnets have a relative permeability similar to that of air, thus the effective air-gap length is large and the magnetizing inductances are very low. This means that the stator flux-linkage is almost equal to the flux linkage created by the permanent magnets,

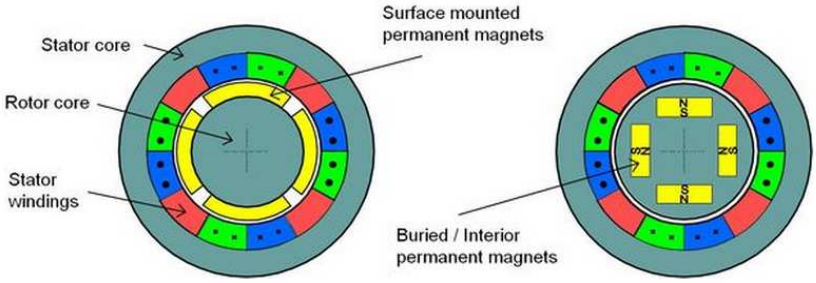

Figure 2.1: Cross section of permanent magnet synchronous machines with surface mounted magnets (SPMSM-left) and interior magnets (IPMSM-right) [19].

see Fig. 2.2.

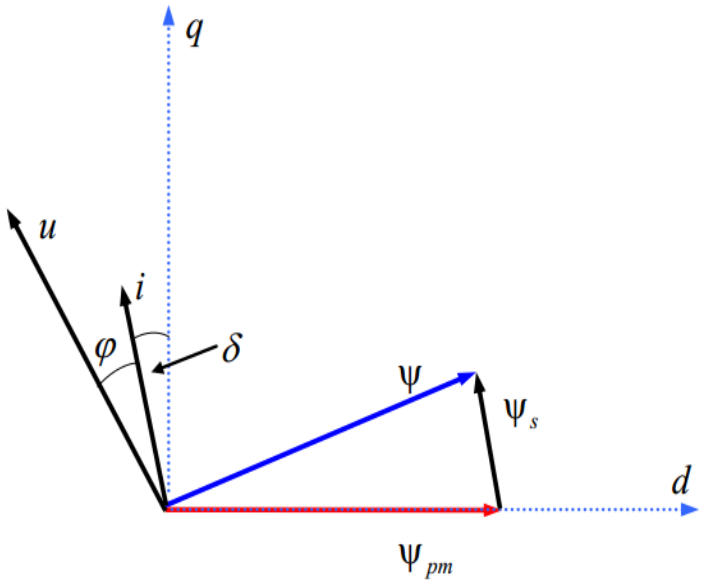

Figure 2.2: Vector diagram of surface-mounted PMSMs [20].

It is not always a helpful factor that the inductances are small, because field weakening might be very problematic [20]. In the field weakening area the speed may still increase, although the voltage has already achieved its maximum value. Field weakening is made possible by increasing the negative $d-$ (direct) axis stator current component. Due to low inductances the field weakening can be obtained only by a high demagnetizing current and a low load. The magnetization of the magnets can be done easily after mounting.

Because the magnets should be located on the curved rotor surface, they have to be either shaped or built out of small magnetic pieces, which are glued together. At higher speeds, the magnets will not be hold due to the centrifugal forces; the magnets can be bound up to the rotor with fiberglass bands or with a non magnetic stainless steel cylinder, thus to ensure sufficient mechanical strength of the rotor construction at the maximum speed. However this may not be desirable electromagnetically as it increases the effective air-gap length. If a stainless steel cylinder is used, eddy currents are induced in the cylinder and the construction may no more be adaptable for the converter because of its high harmonic current components [20].

The PMSMs with surface-mounted magnets on the rotor can be considered to have a smooth electromagnetic air-gap. A PMSM having magnets fixed on its surface in principle corresponds to the non-salient pole machine. The $d-$ (direct) and $q-$ (quadrature) magnetizing inductances of a PM machine with surface magnets are almost equal (linear case). This hypothesis is correct if it is possible to neglect the iron saturation due to the rotor field. However, when the high field magnets are mounted on the rotor surface, different saturation conditions could occur in the stator iron along $d-$ and $q-$axes, and therefore different values of $d-$ and $q-$axes inductances have to be taken into account.

2.1.2 Interior PMSMs

Permanent magnets can be buried in the rotor as shown in the right of Fig. 2.1, and there are a lot of variants of rotor constructions. The rotor design with buried magnets seems to be more complex and more expensive than a machine with surface-mounted magnets. However, IPMSMs still have several advantages. Because of the high air-gap flux density, in some specific designs the IPMSMs produce more torque per rotor volume compared with SPMSMs. The danger of permanent magnet material demagnetization remains smaller, the configuration is mechanically rugged and even higher rotational speeds are achievable. Furthermore, the magnets can be rectangular and there are no fixing and bounding problems with magnets, and the magnets are easy to mount into the holes of the rotor. The most considerable benefit of this construction is that the air-gap flux density can be easily made sinusoidal which makes it possible to achieve a very low cogging torque. A sinusoidal rotor magnetomotive force (MMF) is very helpful in the case of a low speed multi-pole machine. Because it often has a low number of stator slots per pole and phase of multi-pole IPMSMs, the stator MMF is non-sinusoidal. The torque ripple is caused by the interaction of the stator and the rotor MMF harmonics. In order to get a small torque ripple, the rotor MMF should preferably have a sinusoidal waveform [20].

In contrast to the non-salient pole machines where the $q-$axis inductance is

nearly equal to the $d-$axis inductance ($L_q \approx L_d$), in the IPMSMs the $d-$ and $q-$axes inductances are not equal ($L_q > L_d$). The reason is that in the magnetic circuit of IPMSMs on the $q-$axis of the rotor there is only iron, but a part of the magnetic circuit on the $d-$axis of the rotor consists of the magnets whose permeability is approximately equal to that of air. This property is known as saliency and such machines are classified as salient-pole machines. IPMSMs are attractive for applications where the operation of a wide speed range is required (e.g. traction). Because of the different inductances in the $d-$ and $q-$axes, the machines produce a reluctance torque component. Unfortunately, greater inductances, especially the $q-$inductance, lead to the higher armature reaction than that in SPMSMs as shown in Fig. 2.3 and Fig. 2.2.

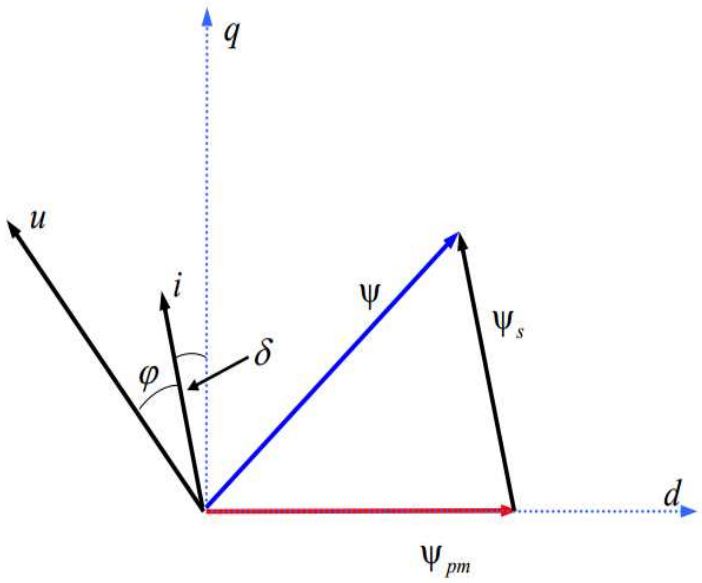

Figure 2.3: Vector diagram of interior PMSMs [20].

2.1.3 Stator Winding Types

In order to improve the machine efficiency and reduce the cost, different winding types have been investigated and analyzed. The stator windings can be classified into two types: distributed windings (DW) and concentrated windings (CW). The topologies of DW and CW are shown in Fig. 2.4.

A promising approach for the optimization of the electric motor efficiency is the concept of asynchronous motors with CW. Unlike a conventional induction motor

with DW, where the coils are wound around multiple lamination teeth, the windings use only a single tooth. Although this technique has been known about for some time, it has not previously been practically applied because of the interfering harmonics that can occur [21]. Generally, because of less end winding, on the points of efficiency and power density, CW will be better than DW.

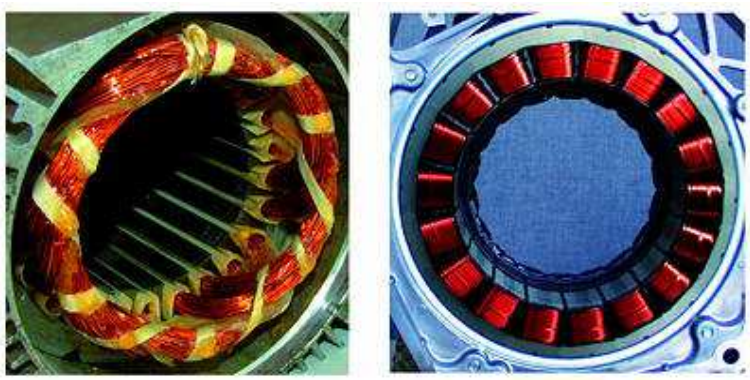

Figure 2.4: Overview of different winding types. Left: Distributed Winding; Right: Concentrated Winding [21].

Recently, PMSMs with fractional slot concentrated windings (FSCW) are widely used in several industry applications. The use of CW offers the advantages of short and less complex end-windings, high slot filling factors, low cogging torques, greater fault tolerances, and low manufacturing costs. The stator coils may be wound either on each tooth (double-layer winding) or only on each alternate tooth (single-layer winding) and the manufacturing of these windings may be much cheaper because they contain simple coils that can be wounded automatically different to distributed windings (DW). Further, FSCW with different combinations of numbers of poles and slots are possible [22].

However, the magnetic field of CW has more space harmonics, including subharmonics. For the PMSMs, the torque is developed by the interaction of a specific high stator space harmonic with the permanent magnets. On the other side, the rest of others sub- and high- harmonics which rotate with the different speed and also in opposite directions, lead to undesirable effects, such as localized core saturation, additional stator and rotor iron losses, eddy current loss in the magnets, noise and vibration which are the main disadvantages of CW [23] [24] .

Nowadays a widely used tooth CW for the PMSMs is illustrated. To improve the MMF winding performances of the FSCW regarding to power losses and noise problems, several methods and techniques are developed and investigated in [25] [26] [27] [28] [29]. References [25] [27] show different efficiency methods for the

reduction of winding sub-harmonics such as using winding coils with different turns per coil-side or using magnetic flux barriers in the specific stator core locations. However, another new solution for reduction simultaneously the sub- and high-MMF harmonics of the FSCW is presented in [26]. An alternative technique for reduction simultaneously the sub- and high- MMF harmonics is presented in [30].

2.2 Traditional Control Strategies

In industry, the field-oriented control (FOC) and direct torque control (DTC) are the two most widely used control strategies for AC drives. Until now, both control methods can provide good dynamic control performance of air gap torque, which is usually the primary input to the process or system that the motor is driving.

2.2.1 Field-Oriented Control

Vector control of AC drives was raised up in the early 1970s, which has epoch - making meaning to the industry in the beginning mainly for induction machines. In order to improve the performance of machine control, it is characterized by a smooth rotation over the entire speed range of the machine, full torque control at zero speed, fast accelerations, and decelerations. Vector control techniques are used for three-phase AC motors to achieve these control objectives. The vector control techniques are also called as field-oriented control (FOC). The basic idea of the FOC algorithm is to decompose a stator current into a magnetic field-generating part and a torque-generating part. Both components can be controlled separately after decomposition. The structure of the motor controller is then as simple as a DC machine [11].

The overview block diagram of the implemented field-oriented control algorithm of PMSM is illustrated in Fig. 2.5. To achieve the high control performance of PMSMs in real-time, the algorithm needs the feedback signals. The essential feedback signals are three-phase stator currents. For the stator voltage, the regulator output is used. For correct operation, the control structure presented requires rotor position and speed information. The slow control loop executes the speed controller and lower priority control tasks. The output of the PI speed controller sets a $q-$axis current reference for the torque producing. The fast control loop is the PI current controller, outputs of which are voltages in rotating reference frame.

FOC selects the $d-$ and $q-$axes stator current vector components as control feedback variables and then uses slip with the closed loop currents as ”effective” manipulated inputs to achieve decoupling state feedback (or feed-forward) on estimated

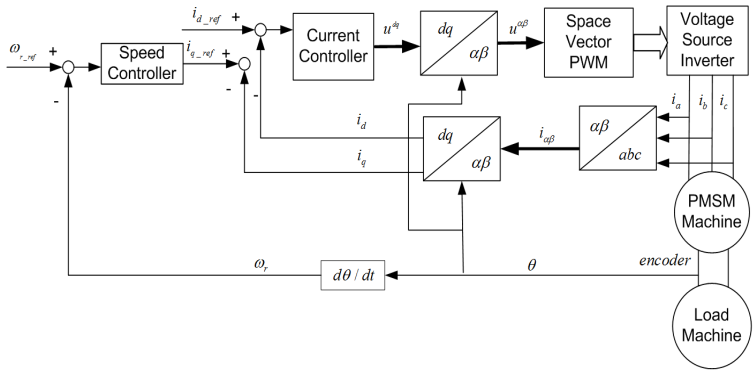

Figure 2.5: PMSM vector control algorithm overview.

rotor (or stator) flux for induction machines [3]. If the state feedback decoupling is reasonably well done, well-behaved open loop control of air gap torque is achieved. Since FOC generally leaves rotor (or stator) flux linkage as open loop states, the dynamic ability to vary flux linkage to optimize bus voltage utilization is generally more limited.

In general, the current vector command from FOC for PMSMs is not linearly related to electromagnetic air gap torque or stator flux linkage. Since FOC generally leaves stator flux linkage as an open loop state, the dynamic ability to vary flux linkage for fast torque performance is mainly limited by the bandwidth of the current regulator.

In addition, the dynamic performance of PMSM drives using current vector control degrades when operating near or at the voltage limit due to voltage saturation in the current regulator. Many approaches have been presented to modify the current regulator to deal with the voltage-limited operation of the PMSM drives, including anti-windup schemes [31]. Many different over-modulation methods have been proposed to improve the dynamic current control performance of FOC at voltage-limited operation [32] [33].

2.2.2 Direct Torque Control

Direct torque control (DTC) has become a widely acceptable alternative to FOC, initially published for induction machines by Takahashi and Noguchi [34] in 1986. DTC selects estimated stator flux magnitude and estimated air gap torque as the two control state variables and applies a closed loop feedback control structure to regulate these states. The closed-loop feedback controller uses the applied stator voltage vector as the sole manipulated input. The DTC use of the stator voltage

vector as its manipulated input is advantageous since it is the only actual physical manipulated input in the system.

The first implementation of DTC by [34] and [35] used a hysteresis control strategy to manipulate the stator flux linkage. Limit switches from lookup table is employed to dictate the appropriate voltage vector applied to the system to achieve the torque and flux control for given torque and flux commands. The block diagram of this bang-bang hysteresis based DTC is shown in Fig. 2.6.

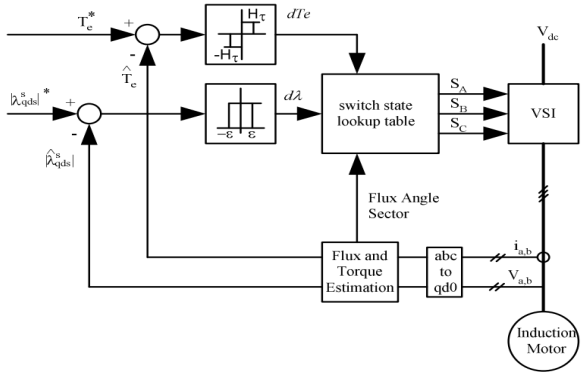

Figure 2.6: DTC block diagram showing hysteresis controller [35].

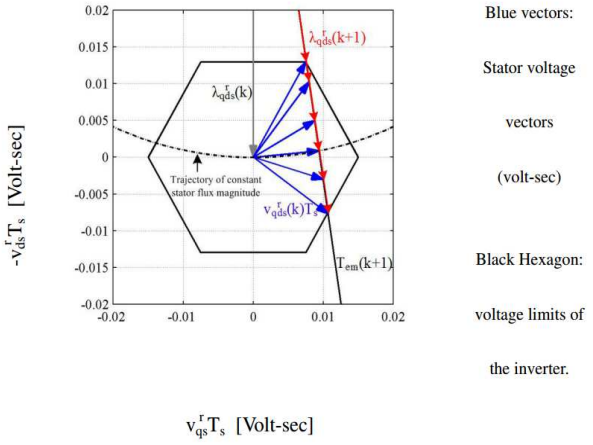

Figure 2.7: Graphical representation of DB-DTFC for IPMSMs [36].

DTC is a technology to control the torque and flux directly by a hysteresis band controller [35] [37]. In spite of simplicity, DTC also has a good torque control on both of steady-state and transient-state operation. On the other hand, it is well

known that DTC presents some disadvantages that can be summarized in the following points [38]:

- Difficulty to control torque and flux at very low speed;
- High current and torque ripple;
- Variable switching frequency behavior;
- High noise level at low speed;
- Lack of direct current control.

In past decades, numerous schemes have been proposed to reduce the torque ripple of conventional DTC. Pulse width modulation (PWM) and space vector modulation (SVM) are employed to produce continuous voltage vectors and smaller torque ripple (compared with conventional DTC) with fixed switching frequency [39] [40]. However, despite the merits aforementioned, due to the using of rotary coordinate transformation and space modulation, this method is usually complicated and relies much on the machine parameters. Another strategy has been proposed to use multilevel inverter or multi-level voltage sectors (12 or 18 sectors) to reduce the torque ripple [38]. But the complexities of hardware or switching table are increased. Fuzzy logic control (FLC) is also proposed to reduce the torque ripple and achieve excellent performance by overcoming the drawback of conventional hysteresis controller. However, the membership function and the system adaptability are difficult to achieve.

A complete modeling and implementation of deadbeat-direct torque and flux control (DB-DTFC) with stator flux linkage observer was first proposed by B. Kenny and Lorenz for induction machine control [41]. This DB-DTFC is a significant improvement on the classical DTC methods. Recently, DB-DTFC is transplanted to IPMSM control in [36]. DB-DTFC uses an inverse IPMSM model to calculate the desired voltage vector based on the commanded air gap torque and stator flux linkage magnitude. With the applied voltage vector, the desired torque and stator flux linkage can be achieved only in one switching interval if the torque and stator flux commands are feasible corresponding to the capability of power supply. Since deadbeat control is the fastest possible control law in discrete system, it is the best solution to obtain the fastest dynamic torque tracking performance in IPMSM control. In addition, like PI-DTC, fixed constant switching frequency is achieved in DB-DTFC, which increases the system control stability and makes it possible to integrate the self-sensing control. The graphical DB-DTFC solution is presented in the synchronous reference frame where the stator flux vector remains stationary at each time step in Fig. 2.7.

2.3 Self-sensing Control

In the high quality control system of electric drives, there is a mechanical sensor in the rotor of the electric machine to measure the position and speed. There are many problems related to the mechanical sensor in the real application, such as the high cost of the high accuracy and quick response sensor, the error with the actual rotor position when the concentrically problem appears after the installation of the sensor, the reliability of the system is reduced by using the sensor and so on. In order to reduce the cost and improve the robustness of the drive system, the mechanical sensors (tachometers, position encoders) need to remove from the control system of electric drives. In large-scale production, the absence of the position sensor implies a worthwhile cost reduction. In addition, the presence of a position sensor represents a possible source of fault. This is not desirable in applications like transportation systems and electrical vehicles, in which a high grade of fault immunity is required.

Self-sensing control of PMSMs is known since 1990s and has became popular since the first decade of this century. The modern self-sensing control methods for PMSMs can be divided into two categories: the first one is based on back electromotive force (back EMF) information [8] [9] [10] and the mathematical models of PMSMs using state observers; the second one is based on tracking of position-dependent spatial saliency using high-frequency(HF) injection [14] [15] [42].

2.3.1 Back-Electromotive Force and State Observers

Within the last decades, several improvements have been made in the technology of closed-loop self-sensing control. The basis of back-electromotive force (back-EMF) for self-sensing control methods are based on the integration of the machine back-EMF to estimate the flux position [9] [10]. The overview block diagram of the implemented self-sensing control algorithm of PMSM is illustrated in Fig. 2.8. The position information in back-EMF can be extracted from the voltage equation 2.1 of the machine in stationary reference frame.

$$\mathbf{u}_s = R_s \mathbf{i}_s + \frac{d}{dt}(\mathbf{L}_s \mathbf{i}_s) + j\omega_r \mathbf{\Psi}_{pm} \tag{2.1}$$

where $\mathbf{\Psi}_{pm} = \psi_{pm} e^{j\theta}$, and $j\omega_r \mathbf{\Psi}_{pm}$ is called the back-EMF including the position information .

It is noteworthy that the parameters of resistance and inductance have to been known in order to estimate the position of the PM flux linkage, $\mathbf{\Psi}_{pm}$. This implies that the flux estimation accuracy is dependent on these two parameters. In addition,

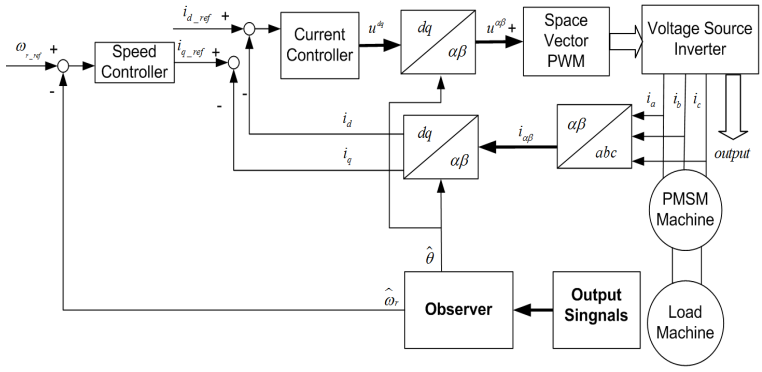

Figure 2.8: Back-EMF Self-sensing control algorithm overview.

the magnitude of the back-EMF is proportional to the machine electrical frequency ω_r. As a result, the performance of back-EMF-based position estimation is speed dependent [43] [44] [45]. Under these effects, the back-EMF-based closed-loop control should have the limitation at zero and low speeds [46]. Several estimation methods have been published to improve the performance at this region. They can be categorized as on-line parameter identification, estimation based on Kalman filter and flux linkage observer, which will be discussed as follows.

To improve the estimation performance at low speed, [47] [48] [49] proposed the on-line parameter identification and adaptive control strategy based on the machine voltage model in the estimated synchronous frame. In addition to the parameter sensitivity, it is also found that the magnetic saturation also affects the accuracy of back EMF-based position estimation. By using the on-line resistance identifications, the estimation error in the back-EMF can be reduced by the adaptive parameter adjustment of the controller [47]. This is similar to the technology of model reference adaptive system (MRAS). For simplicity, the adaptive strategy is a PI controller which manipulates gains with respect to the machine speed. In [48] [49], both closed-loop control of SPMSMs and IPMSMs at the speed of 500 rpm under full-loaded operation are demonstrated. In [47], the closed-loop performance can be enhanced down to the speed of 100 rpm in a IPMSM for full-loaded operation.

Another improvement is to use the theory of Kalman filter for the estimation of back-EMF voltage [50] [51] [52] [53]. In general, Kalman filter is one type of state observer which will continuously change its bandwidth in order to minimize the estimated error covariance, based on the error between the estimated and measured output. Thus, it can be assumed as an optimal algorithm with the least-square method for state estimations. It is supposed that the observer gain decreases when the system noise increases. A detail discussion about the implementation of Kalman

filter can be found in [50]. Some limitations on position estimation at low speed are also mentioned. The important caveat for using Kalman filter is the selection of the coefficients to achieve the optimal estimation performance. It is essential to combine the Kalman filter with some on-line system identification techniques to demonstrate the most effective mode in the back-EMF-based closed-loop system.

The position estimation based on the flux linkage observer has been demonstrated the improved performance at low speeds. Because the flux linkage does not change with respect to the speed, the low speed estimation performance can be improved comparing to the conventional back EMF estimation technique [54] [55] [56]. However, this technique still has the limitation at very low speed. In [54], a SPMSM closed-loop control was limited to speeds greater than 10 rpm. Although a nonlinear flux observer is developed, zero speed closed-loop control still cannot be achieved. The flux estimation technique can have better performance in IPMSMs drives. In [55] [56], the zero and low speed closed-loop control is achieved in an IPMSM. The resistance estimation and decoupling are the key points for low speed closed-loop control using flux linkage observer. However, resistance decoupling at zero and low speed is more difficult in SPMSMs because the resistance component is primarily dominant since the inductance component is quite low. It can be seen that the estimation of flux linkage can have the deterministic impact on the position estimation. When the speed is sufficient high, the flux observer can precisely predict the flux property because the back EMF is sufficient high. In contrast to low speed operation, the current model can be included to improve the flux estimation accuracy [57] [58].

However, since the amplitude of back EMF is proportional to the rotor speed, it fails in the very low-speed region. The small or zero back-EMF voltage will have serious effects on the accuracy of the estimated rotor position. In summary of the back-EMF-based estimation method, it can achieve better estimation performance at the medium and high speed range.

2.3.2 High-Frequency Injection Control

Further researchers have found that the machine anisotropic properties provide additional information on the field angle or the position of the rotor. This inherent property makes it possible to use transient excitations by injected signals having other frequencies than the fundamental. HF injection self-sensing control shows good rotor position estimation results at low speed and zero speed. Unlike back-EMF estimation techniques, the injection-based saliency-tracking techniques use machine spatial saliencies for the position estimation. Recently, it appears more popular because of the capability to overcome the limitation of closed-loop control

at low speed.

A. Rotating Vector Injection

The trajectory of carrier stator current i_c^s with rotating vector carrier voltage signal injection of PMSMs is shown in Fig. 2.10 which is a ellipse. It is difficult to get the position information from the ellipse directly. The proportion between the long and minor axes of the ellipse is $L_q \,/ L_d$. If the value is approaching to 1, the ovality is low and it is very difficult to realize the position extraction. Therefore, the modulation method is used to recover the position information from the carrier stator current i_c^s.

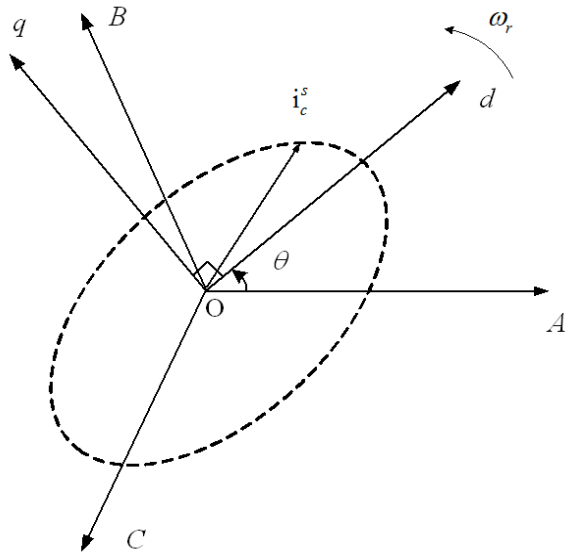

Figure 2.9: The trajectory of carrier stator current i_c^s .

Rotating vector carrier voltage signal injection of PMSMs have first been reported in [59] [60] [61]. These present a new standstill rotor position detecting algorithm for PMSMs without any position sensor. By injecting high frequency current to the stator of the machine, the proposed algorithm provides the standstill rotor position with reasonable accuracy as well as the direction of magnetization.

The position information in the spatial saliency can be extracted by measuring either negative sequence current [62] [63] [64] [14] [15] [65] or neutral voltage [66] [16]. For the negative current measurement, the estimation signal processing can

be classified into $arctan$ current calculation [67], current peak value detection [65], phase locked loop (PLL) state filter and tracking observer [62] [63] [64] [14] [15].

Kim et. al [68] compare different estimation methods for the self-sensing control. It is concluded that both $arctan$ calculation and current peak value detection are sensitive to noise unless an extensive low-pass filter is applied after the estimated signals. The performance of state filter and tracking observer are all based on the vector cross-product. The main difference between them is that the tracking observer included a mechanical model including an estimated moment of inertia and the command feed-forward (CFF) of estimated torque. As a result, the tracking observer can provide the parameter insensitive zero phase lag tracking performance within the observer bandwidth, and the parameter sensitive zero phase lag tracking beyond its bandwidth. However, it is not possible to achieve this lag tracking in the state filter.

B. Pulsating Vector Injection

Pulsating vector carrier voltage injection is firstly proposed by Corley and Lorenz in 1998 [12]. Instead of a constant amplitude rotating in the stationary frame (rotating vector injection), a pulsating vector superimposes an amplitude-modulated voltage or current in the estimated $d-$ or $q-$axis synchronous frame is illustrated in Fig. 2.10. $\hat{d}\hat{q}$ means the rotor position estimation axes.

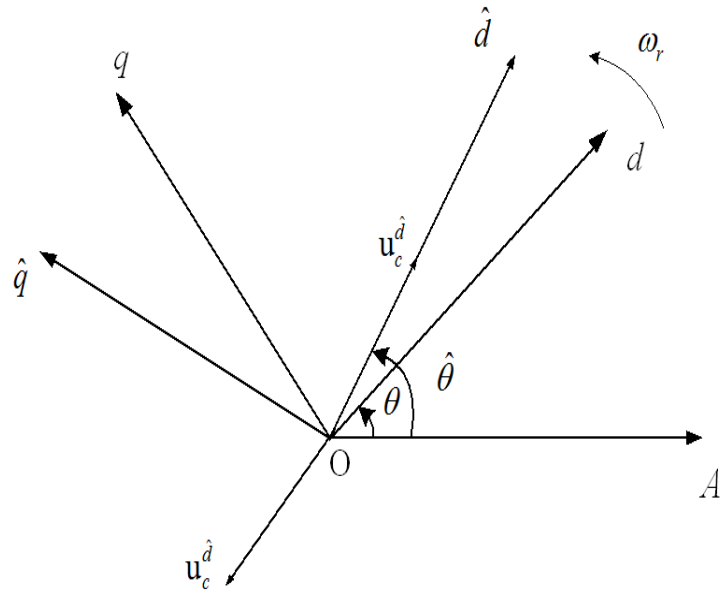

Figure 2.10: Pulsating voltage injection algorithm overview.

Since the pulsating vector voltage can be injected either in rotor $\hat{d}-$ or $\hat{q}-$axis, it is interesting to investigate the estimation performance in both of them. For $\hat{d}-$axis voltage injection, it can produce less torque ripple because the carrier vector does not contribute to any torque production [69]. The same authors have also proposed a two-step injection process for the purpose of polarity identification [70]. It is concluded that $\hat{d}-$axis injection can be better to preserve power conversion performance.

However, the $\hat{q}-$axis pulsating injection has been found to have a unique advantage for reducing the inverter dead-time harmonics because the induced $\hat{d}-$axis current must be zero at the steady state. In other words, the challenge of inverter compensation, parasitically capacitor charging and discharging [71], and zero current clamping [72] as phase currents cross the zero, is avoided if the injection angle is perpendicular to the magnetic axis of the machine [73]. A switching injection method between $\hat{d}-$ and $\hat{q}-$axes based on the operating condition has been proposed by [74]. This injection strategy is suitable for SPMSMs, in which the $d-$axis fundamental current is always zero.

Very recently, a new signal injection method based on the voltage type of square wave has been simultaneously proposed by [75] [76] and [73]. The authors claim that no low-pass filter is required by using a very high frequency (5 kHz) square wave voltage injection to successfully separate the fundamental and carrier components. Especially in [76], the speed controller bandwidth can be enhanced to 50 Hz in a IPMSM drive using the proposed square-wave voltage injection.

2.4 Model Predictive Control

Although PMSM has many advantages like high torque density, high efficiency and so on, it still has many problems in drive system for example coupling, nonlinear and time-varying of parameters and so on. Thus the traditional methods cannot get the expected control performance. The modern control strategies are the new developing directions.

Cascaded control is the state of the art in power electronics and drives since several decades. It is not possible to expect serious changes within a short time, because cascaded control is easy to realize, easy to implement and robust in operation. Furthermore industry seems to be satisfied with the performance of cascaded control there is no strong pressure to improve performance from that side. There are, however, serious drawbacks of cascaded control: its linear concept, the need of an extremely fast operating inner loop, etc. Academics should look out for a better concept to have it available, when the demand for better performing control schemes

occurs again from industry. Conventional DTC has an obvious disadvantage: the torque ripple is considerable. To tackle this drawbacks, many research efforts have been performed.

Predictive control methods are developed to improve the performance of the drive system. Predictive control is a very wide class of controllers that have found rather recent application in the control of power converters and drive systems. Research on this topic has been increased in the last years due to the possibilities of today's microprocessors used for the control.

Model predictive control (MPC) is an alternative optimization and predictive control strategy. It is widely used in the industry communities both for electric drives and power electronics, because it's easy to do implementation [77] [78]. The MPC techniques normally have been classified into two main categories: MPC with continuous control set and MPC with finite control set (FCS-MPC) [79]. The MPC with continuous control set can avoid the cascaded control and provides fixed switching frequency, but the pulse width modulation (PWM) or space vector modulation is still needed. The FCS-MPC utilizes the inherent discrete nature of the power converter without modulator to solve the optimization problem using a single cost function, and has variable switching frequency. The MPC scheme is described as Fig. 2.12.

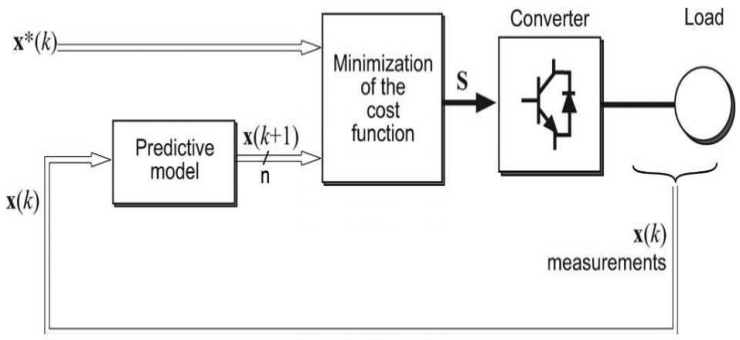

Figure 2.11: Model predictive control scheme [79].

MPC also referred to as receding horizon control, is the one among the so-called advanced control techniques (usually understood as techniques more advanced than a standard PID control) which has been extremely successful in practical applications in recent decades, exerting a great influence on research and development directions of industrial control systems. Applications and theoretical results are in the books [77] [80] [81] and survey papers [82] [83] [84] [85]. An attractive feature of MPC is that it can handle general constrained nonlinear systems with multiple

inputs and outputs in a unified and clear manner. Considering all the possible combinations of switching functions, seven distinct voltage vectors are obtained. These are shown in Fig. 2.12.

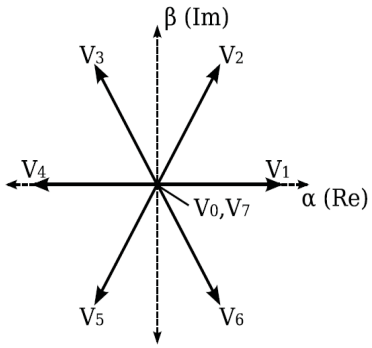

Figure 2.12: Voltage vectors generated by the voltage source inverter.

2.5 Loss Minimization Control

Efficiency optimization has always been an essential problem in energy considerations for electric drives [86] [87] [88] [89]. The operating efficiency depends on the control strategies and the losses can be minimized by the optimal control strategy. There are many methods proposed to reach a high efficiency drive system based on FOC and DTC [90] [91]. However, there is almost no such kind of loss minimization research for MPC [92] and self-sensing control especially with high-frequency injection method. It is necessary to analyze the efficiency of the drives system with optimal control strategy for MPC and self-sensing control. The losses types of PMSMs is shown in Fig. 2.13.

More than 50% of the electrical energy produced worldwide is used by motors [93]. In the applications of continuous long time operation such as electric vehicles and compressor drives, the efficiency is one of the most important performances. The PMSM is suitable for such application due to the high efficiency, high power factor and high power density compared with the DC motors and induction motors.

Regarding the efficiency optimization strategies, there are mainly two kinds of strategies for electric drives: loss model control (LMC) and search control [93] [94] [95] [96] [97]. Both of the strategies can be classified as offline or online (real-time). Offline techniques try to achieve minimum power losses by restructuring the motor or setting its optimal operating point based on pre-determined values. The

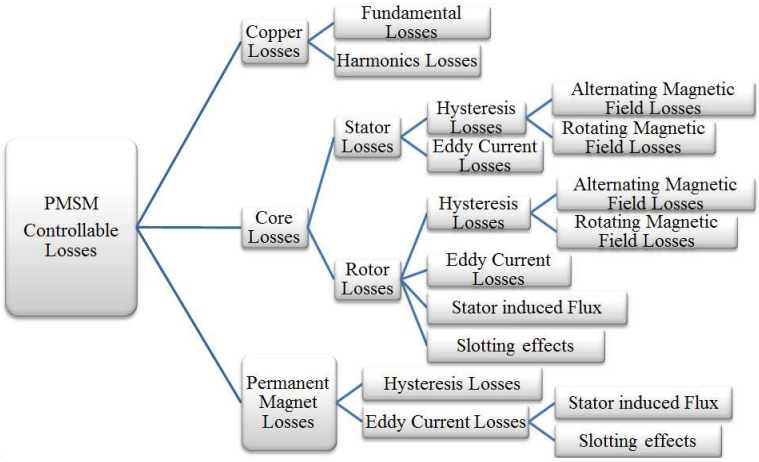

Figure 2.13: The losses types of PMSMs.

drawback of offline techniques is that the losses or the loss model cannot be affected any more by the loss minimization techniques while the motor is running, unless the motor is stopped, restructured, or the operating point is reset. The difference is that the loss model of LMC is only built according to machine parameters, while the loss model of SC also takes into account the losses of the power electronics.

The principle of LMC is that an accurate machine model should be built and it includes the machine losses over the full operating speed range. Based on the speed and current signals, the minimum losses can be achieved by using optimal armature current or optimal flux linkage. Based on LMC method, the machine parameters are nearly known, thus the accuracy of the iron loss and PM loss become a key point of the accuracy of LMC. In [95] [97] the authors model the iron loss of electrical machines, predict and analyze the possible parameters of iron loss, but finally it do not give a clear and fixed strategy for optimizing iron loss. Reference [93] introduces an optimization method to get the optimal $d-$ axis current based on vector control strategy. However, it does not introduce how to get the accurate resistance R_{Fe} parameter for the iron loss in order to fix at the rated operation. Some researchers analyze the iron loss and PM loss based on finite element method (FEM). However, most of them do not take into account the influence of control strategies.

The loss minimization control can be combined with the modern control strategies such as MPC and self-sensing control. For example, the self-sensing control method based on the HF injection, there are some extra losses due to the injection signals. The losses resulting from the HF injection are needed to be analyzed. It is difficult to find a loss minimization control algorithm for HF injection-based self-

sensing control scheme directly. The best way is to analyze the additional losses in the machines, in order to find a balance between the cost of the position encoder and the extra losses consumption.

CHAPTER 3

Self-sensing Control of SPMSMs Based on Different High-Frequency Injection Methods

The magnetic and mechanical design of the PMSMs has impact on the performance of self-sensing control with HF injection [13]. The surface-mounted PMSMs do not have the saliency phenomena in the structure compared with the interior PMSMs. The experimental results of the SPMSM presented in this chapter show the self-sensing control scheme having no limitations with respect to a minimal speed; the drive is able to provide full torque in self-sensing operation even at standstill. The control behavior of position and speed control is equal to a servo drive with resolver feedback. Future developments and possibilities will be discussed.

3.1 Mathematical Model of PMSMs

In order to build the mathematic model of PMSMs, the presumptions are shown as following:

- The positive direction of electromotive force (EMF) and the positive direction of the current is opposite;
- The positive direction of the speed and electromagnetic torque is the counter-clockwise direction;
- Ignoring of the iron saturation effects and the eddy current & hysteresis losses;
- The conductivity of the permanent magnet is zero;
- There is no amortisseur winding in the rotor;

- The electromotive force (EMF) of phase winding is sinusoidal [1].

Fig. 3.1 is a schematic diagram for a two-poles PMSM and the positive direction of the winding current for each phase is specified [98].

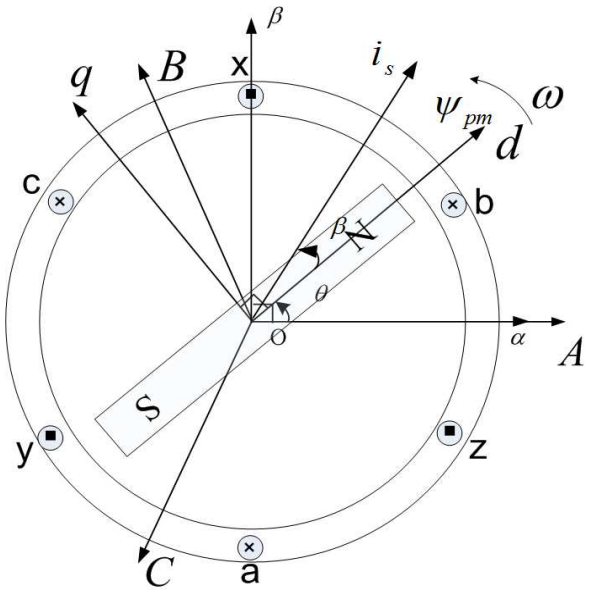

Figure 3.1: Schematic diagram of a two-poles PMSM

In the ABC reference frame, the stator current space vector is defined as (3.1).

$$\boldsymbol{i}_s = \sqrt{\frac{2}{3}}(i_A + a i_B + a^2 i_C) \tag{3.1}$$

In Fig. 3.1 the permanent-magnet excitation magnetic space vector $\boldsymbol{\Psi}_{pm}$ is rotating with the rotor, and its phase is defined by the electrical angle θ.

The stator voltage vector equation based on ABC reference frame can be written as:

$$\boldsymbol{u}_s = R_s \boldsymbol{i}_s + \frac{d}{dt}(\boldsymbol{L}_s \boldsymbol{i}_s) + \frac{d}{dt}(\psi_{pm} e^{j\theta}) \tag{3.2}$$

where, $\boldsymbol{u}_s$ is the stator voltage vector; R_s is the stator phase resistor; $\boldsymbol{L}_s$ is the equivalent synchronous inductance.

In the electromagnetic field, the air-gap is always considered as smooth in SPMSMs, but not smooth in IPMSMs. The equivalent synchronous inductance $\boldsymbol{L}_s$ is not constant, and it makes the machine model difficult to analyze. It is popular to do the transformation to the two-axis reference frame to solve the machine problems. The

axis of the fundamental of the permanent-magnet excitation magnetic field is defined as $d-$axis, and q-axis has a phase lead 90° to d-axis along with the direction of the rotating in Fig. 3.1. The dq-axis reference frame can be seen as the rotating complex plane, where, the d-axis is the real-axis and the q-axis is the imaginary-axis.

Transformation (3.2) to the rotor fixed direct and quadrature axis (dq-axis) results in (3.3).

$$\begin{aligned} u_d &= R_s i_d + \tfrac{d}{dt}\psi_d - \omega_r \psi_q \\ u_q &= R_s i_q + \tfrac{d}{dt}\psi_q + \omega_r \psi_d \end{aligned} \tag{3.3}$$

The electromagnetic torque equation of the PMSMs is shown as (3.4).

$$T_e = P\boldsymbol{\Psi}_s \times \boldsymbol{i}_s \tag{3.4}$$

where, the flux linkage and the current in the dq-axis can be expressed as (3.5).

$$\begin{aligned} \boldsymbol{\Psi}_s &= \psi_d + j\psi_q \\ \boldsymbol{i}_s &= i_d + j i_q \end{aligned} \tag{3.5}$$

Substituting (3.5) into (3.4), the electromagnetic torque equation in the dq-axis result in (3.6).

$$T_e = P[\psi_d i_q - \psi_q i_d] \tag{3.6}$$

The mechanical equation of the PMSMs is (3.7).

$$T_e - T_L = J\frac{d\omega_m}{dt} + R\omega_m \tag{3.7}$$

3.2 High-Frequency Model of SPMSMs

Compared with the salient-pole PMSMs, the SPMSMs do not have the saliency phenomena in the structure. When under the main flux path saturation condition, SPMSMs have the saliency phenomena effects. It is important to point out that saturation saliency is also exist in IPMSMs, but for SPMSMs there is only the saturation saliency in the mostly conditions [61] [98].

In the dq-axis reference frame as shown in Fig. 3.1, the flux leakage function can be described as following:

$$\begin{aligned} \psi_d &= L_d i_d + \psi_{pm} \\ \psi_q &= L_q i_q \end{aligned} \tag{3.8}$$

There is a permanent-magnet excitation magnetic field vector $\mathbf{\Psi}_{pm}$ in the $d-$axis direction. If this magnetic field is big enough, the magnetic flux path in the $d-$axis will have saturation. When the machine is under load condition, due to the superimposing of the armature magnetic field, the saturation of the $d-$axis will increase or decrease.

ψ_{pm} can be described as:

$$\psi_{pm} = L_{md} i_f \tag{3.9}$$

where L_{md} is the excited inductance of the d-axis main magnetic flux path; i_f is the equivalent excited current.

Substituting (3.9) into (3.8), the flux linkage of $d-$axis can be rewritten as:

$$\begin{aligned} \psi_d &= (L_{md} + L_{s\sigma}) i_d + L_{md} i_f \\ &= L_{s\sigma} i_d + L_{s\sigma}(i_d + i_f) \end{aligned} \tag{3.10}$$

For the excited magnetic field of the main magnetic flux path of the $d-$axis, it can be described as:

$$\psi_{md} = L_{md}(i_d + i_f) \tag{3.11}$$

When designing a machine, normally the main magnetic flux path under zero load condition is close to saturation situation. If the directions of the current i_d and i_f are equal, the saturation of the main magnetic flux path of the $d-$axis will increase, and the inductance L_{md} will decrease that could be seen from the Fig. 3.2. On the contrary, if the directions of the current i_d and i_f are opposite, the saturation of the main magnetic flux path will decrease, even then the saturation situation will disappear and the inductance L_{md} will increase.

Therefore the current i_d of the stator current plays an important role in main magnetic flux path of the machine to get the saliency phenomena; it is called the saturation saliency. Obviously, whether the main flux path has saturation or not and how big is the saturation depends on the direction and amplitude of the current i_d, it also depends on the angle β between the stator current vector $\boldsymbol{i}_s$ and $\mathbf{\Psi}_{pm}$ and the amplitude of the current $|\boldsymbol{i}_s|$ (see in Fig. 3.2). When the directions of $\boldsymbol{i}_s$ and $\mathbf{\Psi}_{pm}$ are equal ($\beta = 0°$) and $|\boldsymbol{i}_s|$ is big enough, it will get sufficiently saturation saliency. When the directions of $\boldsymbol{i}_s$ and $\mathbf{\Psi}_{pm}$ are opposite ($\beta = 180°$), the saturation saliency phenomena will disappear. Under the two extreme situations, the difference between the excited inductance L_{md} is the biggest. When $\beta = 90°$ which means the stator current vector $\boldsymbol{i}_s$ is totally the torque component, there is no saturation effect of the main magnetic flux path of the $d-$axis and the difference between the excited inductance L_{md} is 0. When the stator current vector $\boldsymbol{i}_s$ affects the main magnet pole in the two different positive and negative directions, there is a difference between the excited inductance L_{md} and the rotor position information is included in it.

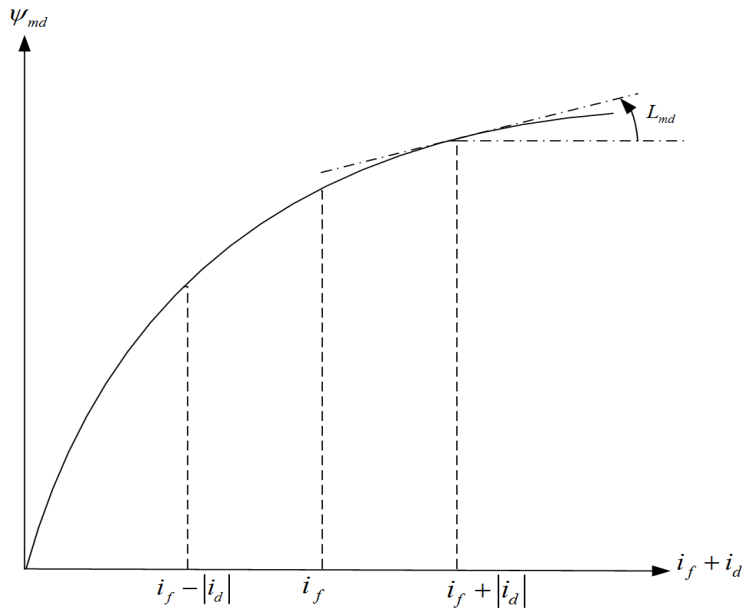

Figure 3.2: The magnetization curve of the main magnetic flux path of the $d-$axis.

The equation of the stator voltage of PMSMs based on $dq-$ axis in fundamental frequency can be rewritten from (3.3):

$$\begin{aligned} u_d &= R_s i_d + L_d \frac{di_d}{dt} - \omega_r L_q i_q \\ u_q &= R_s i_q + L_q \frac{di_q}{dt} + \omega_r L_d i_d + \omega_r \psi_{pm} \end{aligned} \tag{3.12}$$

When a HF voltage or current vector signal is injected, the carrier stator voltage equation normally ignores the resistance and the electromotive force (EMF), because these are much lower than the inductance voltage for high frequencies and can therefore be changed as:

$$\begin{aligned} u_d &= L_d \frac{di_d}{dt} \\ u_q &= L_q \frac{di_q}{dt} \end{aligned} \tag{3.13}$$

3.3 Rotating Vector Injection Method for SPMSMs

The high-frequency injection signal (current or voltage) is superimposed on the fundamental excitation. The applied signals interact with the rotor saliency or magnetic

anisotropy of the motor, and the resulting response (voltage or current) is tracked to extract rotor position information. The persistent high frequency injection signal can be classified as rotating vector or pulsating vector [63] [12].

For the rotating vector injection approach, a rotating voltage vector is injected in the stationary reference frame. A high frequency component is superposed to the current control output signal resulting in a high frequency current response, which can be used for detecting the orientation of the rotor. The position dependent high frequency currents can be measured with the standard current sensors available in industrial drives anyway. There is no need for any additional hardware being not available in standard industrial drives. The self-sensing control scheme using the rotating high-frequency voltage vector is shown in Fig. 3.3.

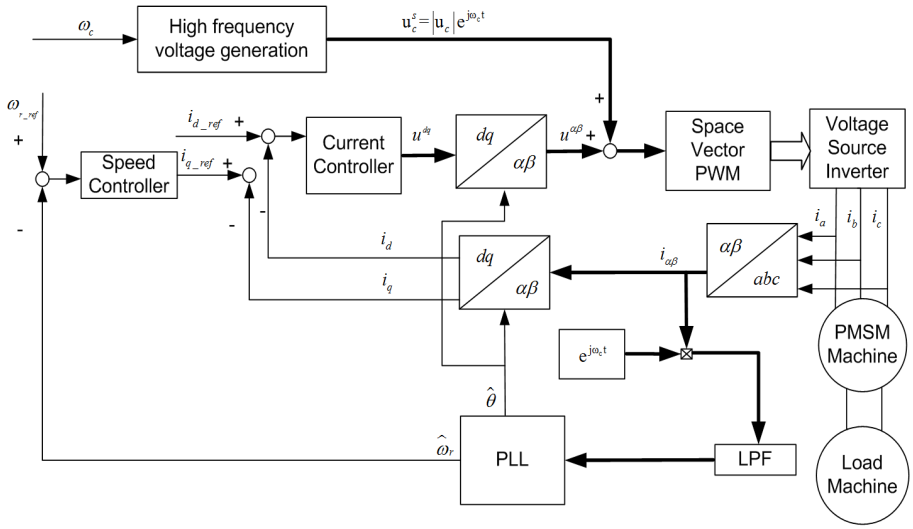

Figure 3.3: Self-sensing control scheme using rotating HF voltage injection

If inject three-phase high frequency sine voltage signal into the SMPM, there will be rotating space voltage vector with constant amplitude and high frequency in the motor. The injection voltage can be described like:

$$\boldsymbol{u}_c^s = |\boldsymbol{u}_c| \left(\cos \omega_c t + j \sin \omega_c t\right) = |\boldsymbol{u}_c| \, e^{j\omega_c t} \tag{3.14}$$

where ω_c is the injection AC voltage frequency; $|\boldsymbol{u}_c|$ is the amplitude of the rotating voltage vector. Subscript s means in the stator stationary ABC frame, subscript $_c$ means the carried (injection) signals.

The voltage vector $\boldsymbol{u}_c^s$ can be transformed to the rotational dq- reference frame:

$$\boldsymbol{u}_c^{dq} = |\boldsymbol{u}_c| e^{j\omega_c t} e^{-j\omega_r t} = |\boldsymbol{u}_c| e^{j(\omega_c - \omega_r)t} \tag{3.15}$$

The known stator voltage (3.2) normally ignores the resistance and the electromotive force (EMF) when a HF voltage vector signal is injected and can therefore be changed as [14]:

$$\boldsymbol{u}_s = \frac{d}{dt}(\boldsymbol{L}_s \boldsymbol{i}_s) \tag{3.16}$$

The voltage vector $\boldsymbol{u}_c^{dq}$ can be rewritten as:

$$\boldsymbol{u}_c^{dq} = \boldsymbol{L}_{dq} \frac{d\boldsymbol{i}_c^{dq}}{dt} \tag{3.17}$$

where

$$\boldsymbol{L}_{dq} = \begin{bmatrix} L_d & 0 \\ 0 & L_q \end{bmatrix} \tag{3.18}$$

Therefore

$$\frac{d\boldsymbol{i}_c^{dq}}{dt} = \boldsymbol{L}_{dq}^{-1} |\boldsymbol{u}_c| e^{j(\omega_c - \omega_r)t} \tag{3.19}$$

The carrier stator current in dq-axis derived from (3.19) results in:

$$\boldsymbol{i}_c^{dq} = \frac{-j\,|\boldsymbol{u}_c|}{\omega_c L_d L_q} [\frac{1}{2}(L_d + L_q) e^{j(\omega_c - \omega_r)t} + \frac{1}{2}(L_d - L_q) e^{-j(\omega_c - \omega_r)t}] \tag{3.20}$$

Transformation (3.20) to the stationary reference frame results in:

$$\boldsymbol{i}_c^s = \boldsymbol{i}_c^{dq} e^{j\omega_r t} \tag{3.21}$$

then

$$\begin{aligned} \boldsymbol{i}_c^s &= \frac{-j\,|\boldsymbol{u}_c|}{\omega_c L_d L_q} [\frac{1}{2}(L_d + L_q) e^{j\omega_c t} + \frac{1}{2}(L_d - L_q) e^{j(-\omega_c + 2\omega_r)t}] \\ &= -j\,|\boldsymbol{i}_p|\, e^{j\omega_c t} - j\,|\boldsymbol{i}_n|\, e^{-j(\omega_c t + 2\theta)} \end{aligned} \tag{3.22}$$

where

$$\begin{aligned} |\boldsymbol{i}_p| &= \frac{L_d + L_q}{2 L_d L_q} \frac{|\boldsymbol{u}_c|}{\omega_c} = \frac{\Sigma L}{\Sigma L^2 - \Delta L^2} \frac{|\boldsymbol{u}_c|}{\omega_c} \\ |\boldsymbol{i}_n| &= \frac{L_d - L_q}{2 L_d L_q} \frac{|\boldsymbol{u}_c|}{\omega_c} = \frac{\Delta L}{\Sigma L^2 - \Delta L^2} \frac{|\boldsymbol{u}_c|}{\omega_c} \end{aligned} \tag{3.23}$$

$$\Sigma L = 1/2(L_d + L_q) \qquad \Delta L = 1/2(L_q - L_d) \tag{3.24}$$

Equation (3.23) describes that the superimposed stator current vector can be departed into two components: one vector $\boldsymbol{i}_p$ is rotating in positive direction according

to the injection angular speed ω_c ; the other vector $\boldsymbol{i}_n$ is rotating in negative direction according to the angular speed $-\omega_c + 2\omega_r$ ($\omega_r = \dfrac{d\theta}{dt}$), and the rotational speed information ω_r only is included in the vector $\boldsymbol{i}_n$ [5].

In order to get the estimated rotor position information, at first using (3.23) to multiply $e^{j\omega_c t}$ will get

$$\boldsymbol{i}_c^s e^{j\omega_c t} = -j\,|\boldsymbol{i}_p|\,e^{j2\omega_c t} - j\,|\boldsymbol{i}_n|\,e^{j2\omega_r t} \tag{3.25}$$

The sensorless control scheme in Fig. 3.3 uses only the second term on the right-side of (3.25), because only this part includes the speed information.

The second step is using a low-pass filter (LPF) in order to extract ω_r from the high frequency carrier current. After the LPF (3.23) will be changed as

$$(\boldsymbol{i}_c^s e^{j\omega_c t})_{LPF} = -j\,|\boldsymbol{i}_n|\,e^{j2\omega_r t} \tag{3.26}$$

The third step is using the phase-locked loop (PLL) block in Fig. 3.4 to estimate the speed and the rotor position information. The input of PLL is (3.26), and multiply with $[\cos 2\hat{\theta}\ \sin 2\hat{\theta}]^T$ will get

$$|\boldsymbol{i}_n|\sin(2\hat{\theta} - 2\theta) \approx 2\,|\boldsymbol{i}_n|\,\hat{\theta} - 2\theta \tag{3.27}$$

Then use the PI controller to get the estimate speed and use the integral part to get the estimated angle in the closed-loop self-sensing control system.

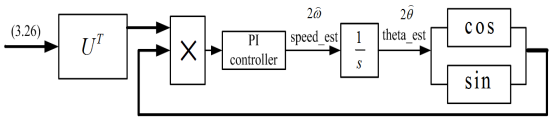

Figure 3.4: The PLL block

3.4 Pulsating Vector Injection Method For SPMSMs

For the rotor design of the surface-mounted PMSMs, the value of $d-$axis inductance L_d and $q-$axis inductance L_q can be considered as unequal when the machine is tested. The saliency ratio of SPMSMs is very small when the machine is under tested. The pulsating injection is carried out by superimposing a voltage or current vector at the estimated synchronous reference frame, and it would be robust to local saliency [6].

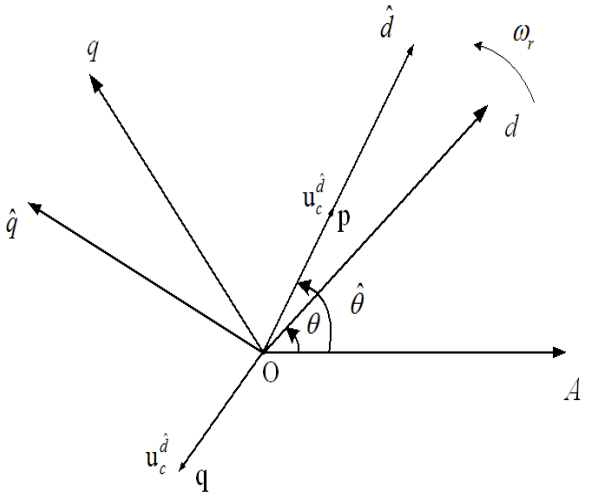

Figure 3.5: Pulsating voltage injection into the estimated $d-$axis.

If the high frequency voltage is injected into the estimated $\hat{d}-$axis in the $\hat{d}\hat{q}$ reference frame shown as Fig.3.5, the voltage vector can be written like:

$$\boldsymbol{u}_c^{\hat{d}} = U_c \cos(\omega_c t) \tag{3.28}$$

where, ω_c and U_c is the pulsating frequency and the amplitude of the voltage, respectively. It can be seen in Fig.3.5, the pulsating voltage vector $\boldsymbol{u}_c^{\hat{d}}$ is located in the $\hat{d}-$axis and its pulsating range is $|\bar{po}| = |\bar{oq}| = U_c$.

Transformation (3.28) to the $dq-$axis reference frame results in:

$$\boldsymbol{u}_c^{d} = U_c \cos(\omega_c t) e^{j(\hat{\theta}-\theta)} \tag{3.29}$$

If $\hat{\theta} = \theta$, the pulsating voltage vector $\boldsymbol{u}_c$ is directly along with the $d-$axis and its resulting pulsating magnetic filed is added with the excited magnetic filed Ψ_{PM}. Therefore it induces the saliency saturation of the excited magnetic flux path and result in the modulation effects for $\boldsymbol{u}_c^d$ [15]. When $\boldsymbol{u}_c$ deviates the $d-$axis, the modulation effects are changed and these will affect the carrier current. The position information is included in the current and is derived as [74]:

$$\boldsymbol{i}_c^{dq} = \frac{U_c}{\omega_c} \sin \omega_c t [\frac{1}{L_d} \cos(\hat{\theta} - \theta) + j \frac{1}{L_q} \sin(\hat{\theta} - \theta)] \tag{3.30}$$

It demonstrates $|\boldsymbol{i}_c^{dq}|$ the amplitude of the carrier current is connected with the pulsating voltage, frequency and the estimation error.

Transformation (3.30) to the stationary reference frame results in:

$$\begin{aligned} \boldsymbol{i}_c^s &= \boldsymbol{i}_c^{dq} e^{j\theta} \\ &= \frac{-jU_c}{4\omega_c L_d L_q}\{[(L_d+L_q)e^{j(\omega_c t+\hat{\theta})} - (L_d-L_q)e^{j(\omega_c t+\hat{\theta}-2\gamma)}] \\ &+ [-(L_d+L_q)e^{j(-\omega_c t+\hat{\theta})} + (L_d-L_q)e^{j(-\omega_c t+\hat{\theta}-2\gamma)}]\} \\ &= \boldsymbol{i}_p + \boldsymbol{i}_n \end{aligned} \tag{3.31}$$

where $\gamma = \hat{\theta} - \theta$, $\boldsymbol{i}_p$ and $\boldsymbol{i}_n$is the positive and negative current component, respectively.

In order to get the position information, the carrier current $\boldsymbol{i}_c^s$ need to be demodulated. Making the transformation, it means using (3.31) multiply $e^{-j(\omega_c t+\hat{\theta})}$:

$$\boldsymbol{i}_p e^{-j(\omega_c t+\hat{\theta})} = \frac{-jU_c}{4\omega_c L_d L_q}[(L_d+L_q) - (L_d-L_q)e^{j(2\theta-2\hat{\theta})}] \tag{3.32}$$

$$\boldsymbol{i}_n e^{-j(\omega_c t+\hat{\theta})} = \frac{-jU_c}{4\omega_c L_d L_q}[(L_d-L_q)e^{j(-2\omega_c t-2\gamma)} - (L_d+L_q)e^{j(-2\omega_c t)}] \tag{3.33}$$

Obviously the current in (3.33) is the high frequency component and can be easily filtered by the low pass filter (LPF). These is only the estimation error $2\Delta\theta$ in (3.32), where

$$\Delta\theta = \theta - \hat{\theta} \tag{3.34}$$

Equation (3.32) can be rewritten as:

$$\boldsymbol{i}_p e^{-j(\omega_c t+\hat{\theta})} = \frac{U_c}{4\omega_c L_d L_q}\{-(L_d-L_q)\sin 2\Delta\theta - j[(L_d+L_q) - (L_d-L_q)\cos 2\Delta\theta]\} \tag{3.35}$$

3.5 Implementation and Experimental Results

3.5.1 Hardware Description

The proposed self-sensing control methods have been tested on an experimental test bench. It consists of a surface-mounted permanent-magnet synchronous machine and a 2.2 kW squirrel-cage induction machine. The IM driven by a commercial LTi inverter, is used as load machine. The SPMSM is driven by a modified SEW 11.2 kVA inverter which provides full control of IGBT gates. A self-made 1.4 GHz

(a) The machines (b) The inveters (c) The front view

Figure 3.6: The test bench of the SPMSM

Table 3.1: Parameters of the SPMSM

Nominal power	$2.7KW$
Rated torque	$8.8Nm$
Rated current /voltage(rms)	$6.3A/330V$
Pole pair	3
Phase inductance	$15.2mH$
Phase resistance	1.7Ω
Rated speed	3000 rpm

real time Pentium computer system is used [99]. The rotor position is measured by a 1024 lines incremental encoder and the switching frequency of the PWM is 16 kHz. The current is processed by the standard 12-Bit A/D converter to modulate the estimated position and speed. The parameters of the SPMSM are given in Table 3.1. Fig. 4 shows the picture of the test bench.

3.5.2 Experimental Results

The self-sensing performance of the SPMSM in transient-state and steady-state with different load torque is investigated. The rotating voltage injection with high frequency of 1 kHz is used, with the amplitude of 30 V. Several tests with different operating points are observed in the closed-loop control scheme without the position encoder. The self-sensing control strategy applied in the experiments is the normal rotating high-frequency injection method seen in Fig. 3.3.

The very low speed steady-state experimental results of the SPMSM can be seen in Fig.3.7. The speed is 1 rpm. Fig.3.7 shows the estimated speed, estimated position and estimation error between the estimated position and the encoder position.

The value of errors has small variability in the constant speed. It is important to point out that the SPMSM at the very low speed operation is under no load. The second test is to verify the performance of self-sensing control of the SPMSM run at the low speed 60 rpm when the load is constant as 100% rated torque. Fig. 3.8 shows the estimated speed, estimated position and estimation error between the estimated position and the encoder position. It can be seen that the value of errors is bigger than that of no load.

The step-speed state experimental results of the SPMSM can be seen in Fig.3.9. The speed increases from 60 rpm to 90 rpm while the torque is constant as 50% rated torque. Fig. 3.9 shows the estimated speed, estimated position and estimation error between the estimated position and the encoder position. The value of errors has small variability in the constant speed. The big variability shows up with the speed step-up from 60 rpm to 90 rpm, which is the dynamic disadvantage of self-sensing control.

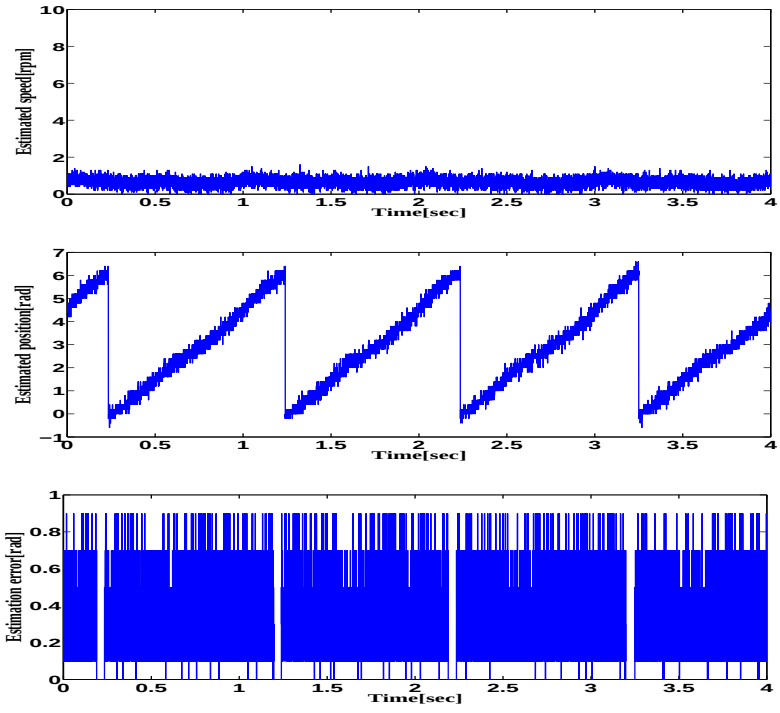

Figure 3.7: The self-sensing control of SPMSM with 30 V carrier voltage at $\omega_c = 1000Hz$ operate at very low speed 1 rpm.

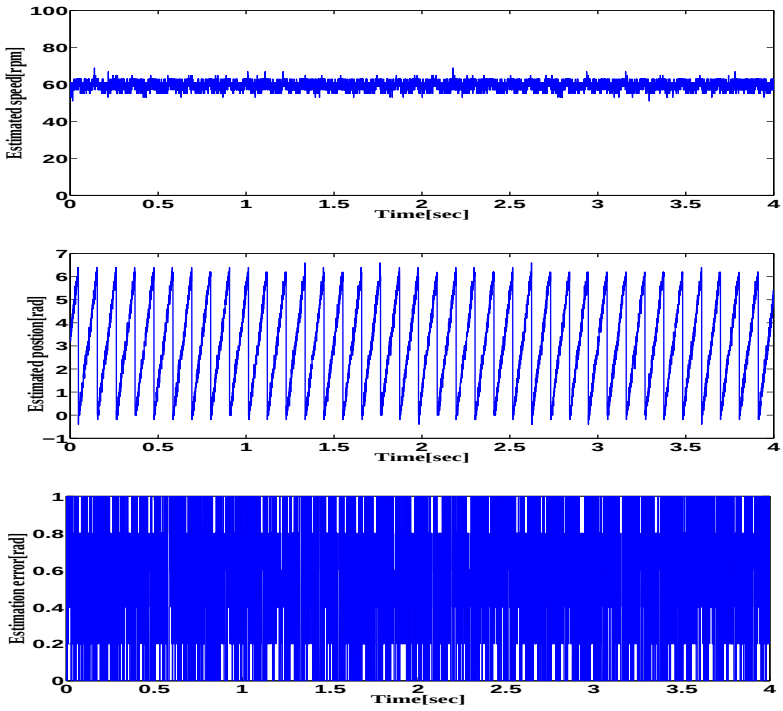

Figure 3.8: The self-sensing control of SPMSM with 30 V carrier voltage at $\omega_c = 1000Hz$ operate at 60 rpm.

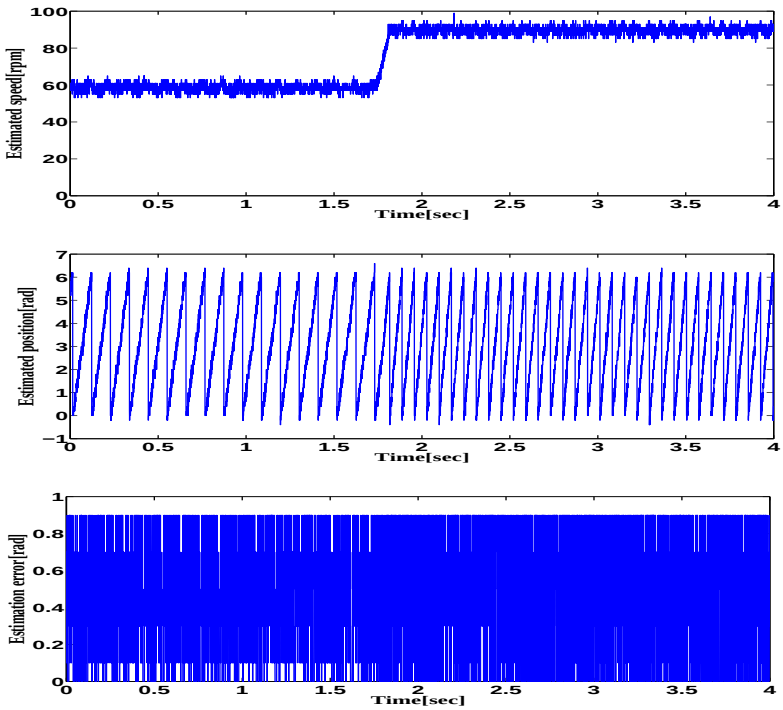

Figure 3.9: The self-sensing control of SPMSM with 30 V carrier voltage at $\omega_c = 1000Hz$ step-up from 60 rpm to 90 rpm.

3.6 Summary

Over the last decade, several solutions have been proposed for both speed and position self-sensing methods for PMSMs. Initial rotor position estimation for PMSMs has been an ongoing topic of research. In industrial and automotive products, the self-sensing control with a high-frequency (HF) injection method shows good rotor position/speed estimation results at zero & low speed. The HF injection signal (current or voltage) is superimposed to the fundamental excitation. The applied signals interact with the rotor saliency or magnetic anisotropy of the motor, and the resulting response (voltage or current) is tracked to extract rotor position information. The persistent high frequency injection signal can be classified as rotating vector or pulsating vector. In the first approach, a rotating voltage vector is injected into the stationary reference frame. The pulsating injection is carried out by superimposing a voltage vector at the estimated synchronous reference frame.

The requirement of using HF injection method is that the rotor has the saliency, which can modulate the high frequency voltage signal. For standard produced induction machines, there is no saliency because the symmetry of cage rotor structure. There are two reasons to cause the rotor saliency: one is the saturation saliency induced by the saturation of the flux path; the other one is the special design of the rotor to lead to the structural saliency. For PMSMs, the SPMSM regarded as a non-salient machine for general applications, it still has some saliencies due to the magnetic saturation in the stator iron caused by the PM flux. The magnets of IPMSMs fixing inside of the rotor lead to the structural saliency.

The rotating and the pulsating vector injection methods both can be used to estimate the initial position and are adapted for the low speed area. They are not available in the high speed area, because the Back-EMF is very big and the high frequency model of the machine is not exactly any more. They are relied on the saliency but not the parameters of the machines. and this is the big advantage of the injection methods. However, the two methods have difference. The pulsating vector injection method can get the estimation error directly, whereas, the rotating vector injection method gets the estimated position. It induces the different modulation strategies between the two injection methods.

Generally, the pulsating vector injection method is more suitable for the SPMSM, since the SPMSM has no structure saliencies and this method is more robust. In this chapter, the rotating vector injection method is applied to the SPMSM, and it can be seen the experimental results achieve the good self-sensing performance at low speeds. That proves the saturation saliencies of this SPMSM is signification.

CHAPTER 4

Estimation Accuracy Analysis for Injection-based Self-sensing Control of IPMSMs

Overall the IPMSMs are much more suitable for self-sensing control based on HF injection due to the significant saliency in comparison to SPMSMs. IPMSMs have highlights due to the structure saliency especially for the self-sensing control based on HF injection method [100] [101] [102]. Generally the standard design of IPMSM with distributed windings (DW) is extremely qualified to be controlled without a position sensor. IPMSMs using concentrated windings (CW) offer the advantages of shorter and less complex end-windings, higher slot filling factors, lower cogging torques, greater fault tolerances, and low manufacturing costs. The stator coils may be wound either on each tooth (double-layer winding) or only on each alternate tooth (single-layer winding) and the manufacturing of these windings may be much cheaper because they contain simple coils that can be wound automatically different to DW. However CW-IPMSMs also have more space harmonics, including sub-harmonics, which lead to undesirable effects, such as additional stator and rotor iron losses, as well as eddy current loss in the magnets [103] [104]. Self-sensing control of CW-IPMSMs in the industrial community is still a challenge, and the performance is still needed to be improved. Newly designed CW-IPMSMs [27] and [30] with lower space harmonic contents will be tested and analyzed in this chapter.

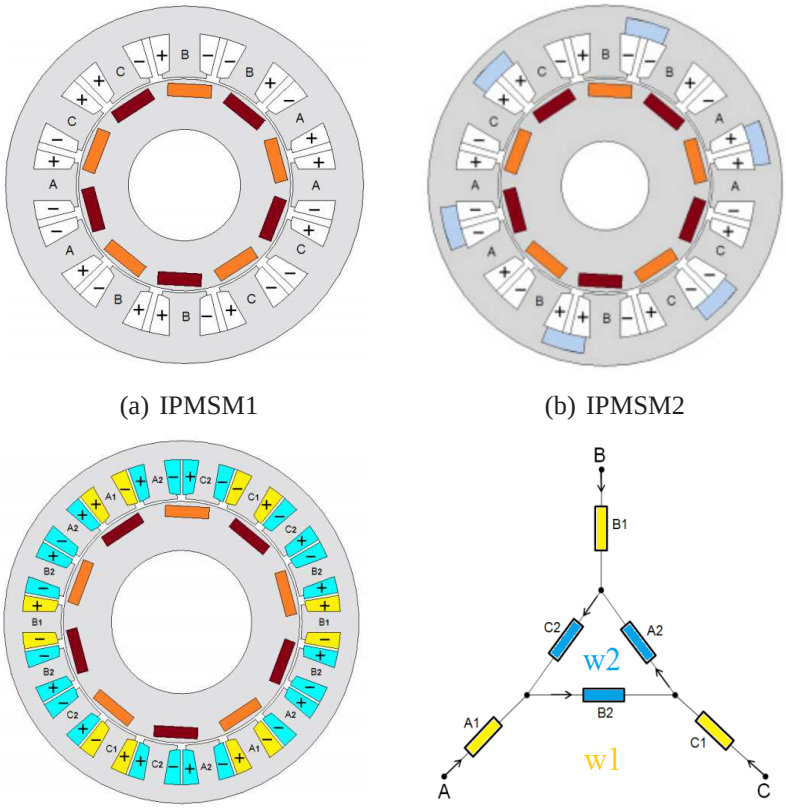

(a) IPMSM1 (b) IPMSM2

(c) IPMSM3 (d) IPMSM-3 *Star*& *Delta* winding connection

Figure 4.1: Winding layout topology of three IPMSMs

4.1 Novel CW-IPMSMs Design

Two novel designed CW-IPMSMs will be analyzed and tested in the chapter. In order to compare these with the conventional machines, three CW-IPMSMs with different stator design are comparatively demonstrated, which are shown in the following Table 4.1. All the three IPMSMs contain concentrated double-layer windings, and their winding topology can be seen in Fig. 4.1. The technical parameters of the two novel CW-IPMSMs are shown in Table 4.2. The IPMSM-1 without technical date is only the simulation model in purpose to do the comparison.

There are many possible slot number and pole number combinations for PM machines with concentrated windings.The winding layout and the winding factor of a PM machine with concentrated winding depend on its combination of pole and slot

Table 4.1: Three CW-IPMSMs

IPMSM1	conventional 12-teeth /10-poles
IPMSM2	novel 12-teeth /10-poles
IPMSM3	novel 18-teeth /10-poles

Table 4.2: Parameters of novel IPMSMs

Parameters	IPMSM2	IPMSM3
Nominal power	425W	31KW
Rated torque	2Nm	200Nm
Rated current /voltage(rms)	50A/8.5V	100A/310V
Pole pair	5	5
d / q-axis inductance	0.05 mH/0.095mH	0.76 mH/1.168mH
Resistance	10$m\Omega$	32$m\Omega$
Rated/maximum speed	2000/4000 rpm	4000/14000 rpm

number. Therefore, this combination should be chosen carefully in order to maximize the fundamental (magnetomotive force (MMF) working harmonic) winding factor and minimize the eddy current losses. Single-layer windings are preferred to double-layer windings when a high fundamental winding factor and high fault-tolerance are required. Otherwise, double-layer windings are preferable to limit the losses and torque ripple. The air-gap flux density sub-harmonics of IPMSM-2 can be reduced since the fractional slot tooth concentrated windings use magnetic flux barriers in the stator yoke [27], The 5th air-gap flux density harmonic of IPMSM-2 induces the torque as the fundamental, and the flux density harmonics spectrum comparison results with conventional 12 teeth/10-poles can be seen in Fig. 4.2. It can be seen that the low- and high- specific harmonics such as the 1^{st} and 11^{th} of IPMSM-2 can be reduced or completely canceled. It's proved for IPMSM-2: the sub-harmonics can be reduced more than 60%, power loss can be reduced up to 40.6% for the stator iron losses, 60% for the rotor iron losses and up to 80% for the magnet losses.

A novel method for reducing simultaneously the sub- MMF-harmonics of the fractional slot concentrated windings (FSCW) is presented in [30]. The well known 12-teeth/10-poles winding is considered during the optimization of its MMF characteristics. The reduction of unwanted harmonics is performed by increasing the

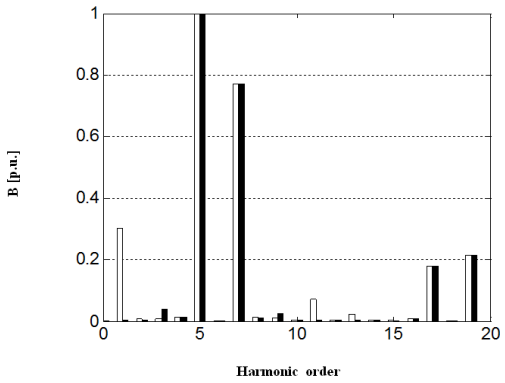

(a) Air-gap flux density; (Hollow □) IPMSM-1,(Solid □) IPMSM-2

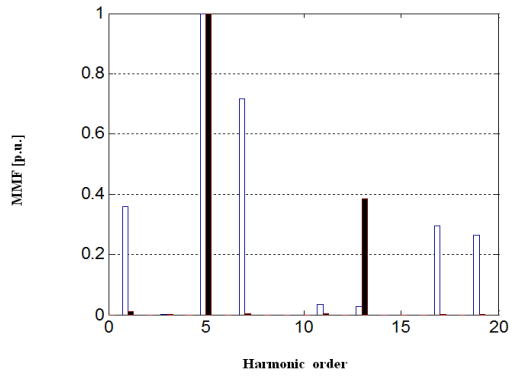

(b) MMF; (Hollow □) IPMSM-1,(Solid □) IPMSM-3

Figure 4.2: The harmonics spectrum comparison of CW-IPMSMs [27] [30]

number of stator slots and using two different winding systems which are shifted in space and time. Fig. 4.1(d) shows the new winding topology and connection designed according to this new technique. The index 1 and 2 donate the first and second winding systems (A1, B1, C1 and A2, B2, C2), respectively. Where index 1 indicates $Star$ connection and index 2 indicates $Delta$ connection. The first winding system is similar with the 12 teeth/10-poles single-layer winding (yellow winding), and the second winding system is similar with the 12-teeth/10-poles double-layer winding, however with unwound teeth lying in-between coils (blue winding). Using the winding distribution and choosing for a proper relation between N_{w1} and N_{w2} (winding number) $\delta_{w1} = 0^\circ$, $\delta_{w2} = 90^\circ$ (current load angle), the specific MMF harmonics such as the 1^{st}, 7^{th}, 17^{th}, and 19^{th} can be reduced or completely cancelled. It is important to point out that the 5th MMF harmonic induces the torque

as the fundamental. Fig. 4.2 compares MMF harmonics spectrum results for the conventional 12 teeth/10-poles and the new 18 teeth/10-poles winding. It can be seen that most of the sub- and high- MMF harmonics of IPMSM-3 are cancelled. IPMSM-3 with the new winding type the radial force modes of low order (mode-2) the sub-harmonics of which are reduced about 70%, the stator and rotor iron losses are reduced 30% and the magnet losses are reduced 80%.

The advantage of novel designed machines with reduced sub-harmonics bringing eddy current reduction is not only a great benefit to the machine loss, but also attractive to the self-sensing control with HF injection. This chapter focuses on the HF injection-based self-sensing method of these two new designed CW-IPMSMs, in order to evaluate the control performance of self-sensing technology.

4.2 Machine Modeling and HF Injection Method

A summary of the used symbols is given in appendix. The stator flux linkage vector equation of IPMSMs can be expressed as

$$\boldsymbol{\Psi}_s = \boldsymbol{L}_s \boldsymbol{i}_s + \boldsymbol{\Psi}_{pm} \tag{4.1}$$

where

$$\boldsymbol{L}_s = \begin{bmatrix} \Sigma L + \Delta L \cos 2\theta & \Delta L \sin 2\theta \\ \Delta L \sin 2\theta & \Sigma L - \Delta L \cos 2\theta \end{bmatrix} \tag{4.2}$$

$$\Sigma L = 1/2(L_d + L_q) \qquad \Delta L = 1/2(L_q - L_d) \tag{4.3}$$

The stator voltage vector equation can be expressed as

$$\boldsymbol{u}_s = R_s \boldsymbol{i}_s + \frac{d\boldsymbol{\Psi}_s}{dt} \tag{4.4}$$

When a HF voltage or current vector signal is injected, the stator voltage equation normally ignores the resistance and the electromotive force (EMF), because these are much lower than the inductance voltage for high frequencies and can therefore be simplified to

$$\boldsymbol{u}_s = \boldsymbol{L}_s \frac{d\boldsymbol{i}_s}{dt} \tag{4.5}$$

If a three-phase HF sine voltage signal is injected into the IPMSMs, a rotating space voltage vector with constant amplitude and high speed in the machines will be achieved. The injection voltage can be described as

$$\boldsymbol{u}_c^s = |\boldsymbol{u}_c|(cos\omega_c t + j sin\omega_c t) = |\boldsymbol{u}_c| e^{j\omega_c t} \tag{4.6}$$

where ω_c is the injection AC voltage frequency, $|\boldsymbol{u}_c|$ is the amplitude of rotating voltage vector.

The induced carrier current vector $\boldsymbol{i}_c^s$ can be calculated as

$$\boldsymbol{i}_c^s = -j|\boldsymbol{i}_p|e^{j\omega_c t} + -j|\boldsymbol{i}_n|e^{j(-\omega_c t+2\theta)} \tag{4.7}$$

where

$$|\boldsymbol{i}_p| = \frac{\Sigma L}{\Sigma L^2 - \Delta L^2}\frac{|\boldsymbol{u_c}|}{\omega_c} \tag{4.8}$$

$$|\boldsymbol{i}_n| = \frac{\Delta L}{\Sigma L^2 - \Delta L^2}\frac{|\boldsymbol{u_c}|}{\omega_c} \tag{4.9}$$

Equation (4.7) describes the superimposed stator current vector composed two components: one vector $\boldsymbol{i}_p$ is rotating in positive direction according to the injection angular speed ω_c ; the other vector $\boldsymbol{i}_n$ is rotating in negative direction according to the angular speed $-\omega_c + 2\omega_r$ ($\omega_r = \dfrac{d\theta}{dt}$), and the rotational speed information ω_r only is included in the vector $\boldsymbol{i}_n$.

This chapter focuses on the rotating HF voltage injection method, but in the case of pulsating signal injection with different signal processing the performance would be different. Especially, pulsating signal injection would be robust to local saliency and cross saturation. In order to prove the novel machine design is attractive to the self-sensing control, the less robust injection method is used.

4.3 Analysis of Estimation Accuracy

There are many sources which affect the estimation accuracy in the self-sensing system of IPMSMs based on HF injection, these are saturation, eddy current, HF rotor/stator resistance, temperature, carrier voltage distortion, inverter-nonlinearity and so on. One of the major issues is saturation effects [16] [42] [105] which include: 1) signal-to-noise-ratio (SNR) changing with the saliency ratio of the machine; 2) cross saturation depending on the stator rotor design when the machine is under load; 3) harmonic distortion caused by secondary saliencies and saturation-induced saliencies.

These saliencies depend on the flux waveform in the air gap that is a function of the stator and rotor design, and they can be reduced by a proper machine design. Due to the new designed IPMSMs have the advantage of lower sub- & high- MMF harmonics and lower eddy current loss. These characteristics are investigated to prove the new machines being more qualified to be controlled without an encoder.

4.3.1 Saliency Analysis

Inductances analysis based on 2-D finite element method (FEM), and the characteristics of non-linear machine parameters are investigated and analyzed. Fig.4.3 and Fig. 4.4 show the inductances of the new designed IPMSM2 and IPMSM3 without HF injection. The calculation of inductances at different loaded conditions has been performed by modifying the current components i_d and i_q in a wide range.

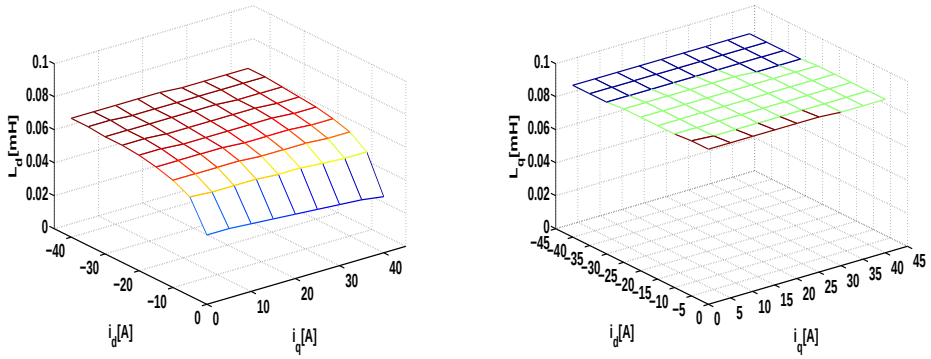

(a) L_d (b) L_q

(c) $L_q - L_d$ (d) L_{dq}

Figure 4.3: Inductances analysis of IPMSM-2

Fig. 4.3(a) and Fig. 4.3(b) show the $d-$ and $q-$axis inductances of IPMSM2 for the load varying from 0% to 100% rated. This novel IPMSM2 is a special high current, low voltage, and very low inductance machine, so it's not easy to analyze higher than 100% rated load condition compared with IPMSM3. The $q-$axis inductance L_q is more stable than the $d-$axis inductance L_d. Furthermore, L_d doesn't change very significantly when the current i_d is constant and the load is changing,

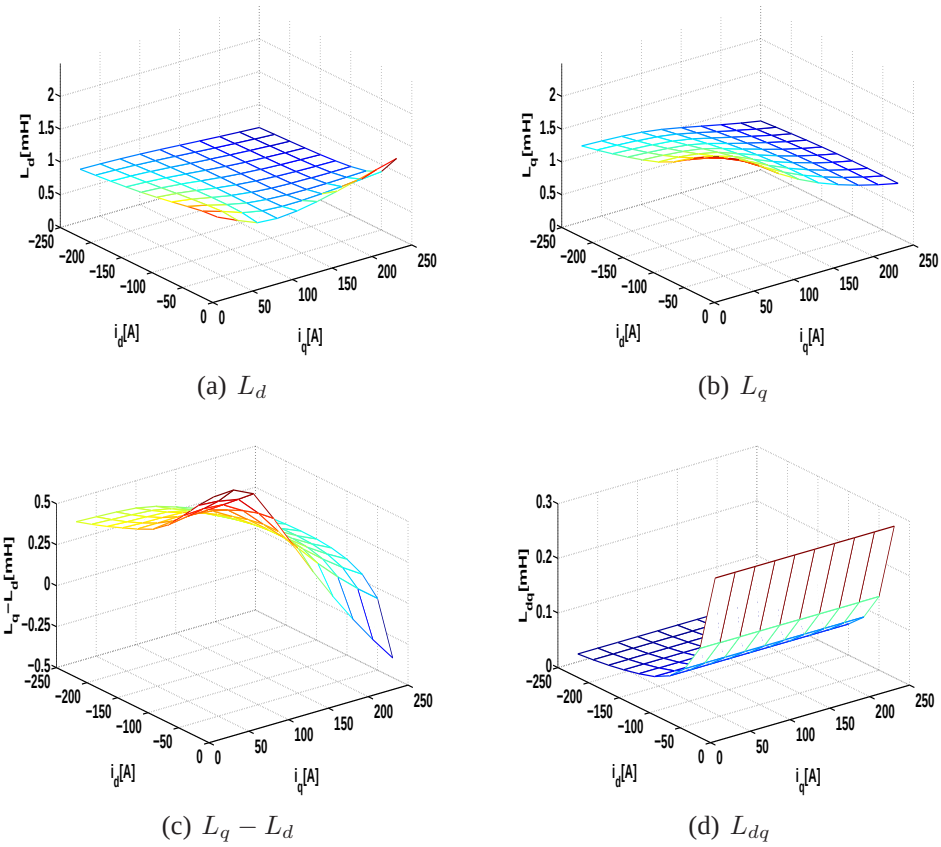

(a) L_d (b) L_q

(c) $L_q - L_d$ (d) L_{dq}

Figure 4.4: Inductances analysis of IPMSM-3

whereas, L_d changes rapidly for the conventional CW IPMSMs. Wide variability is generally an unattractive property for sensorless control [12], and this novel IPMSM2 with small inductance variability is really attractive for sensorless control. Fig. 4.3(c) shows the inductance value $L_q - L_d$ which is double value of ΔL, and there is no a point of zero saliency which is unattractive for sensorless control. When the current i_d is between 0A and -15A, the saliency is much more significant.

Fig. 4.4(a) and Fig. 4.4(b) show the $d-$ and $q-$axis inductances of IPMSM3 for the load varying from 0% to 200% rated. Both L_d and L_q are more stable than the conventional CW IPMSMs, and this novel IPMSM3 is also attractive for sensorless control. Fig. 4.4(c) shows the inductance value $L_q - L_d$, and there is also no a point of zero saliency. When the current i_q is between 0A and 125A which means the load is between 0% and 100% rated, the saliency value is positive. When the current i_q is between 125A and 250A which means the load is between 100% and 200% rated,

the saliency value is negative. The saliency value is much more significant when the current i_d is between 0A and -125A.

When the IPMSM-3 is operated under high load between 100% and 200% rated, some of the flux paths are changed. The $q-$axis inductance L_q is substantially decreased due to the changes of the flux paths. Therefore, the $d-$axis inductance L_d is larger than the $q-$axis inductance L_q because some fluxes pass through the highly saturated part of the stator where the $q-$axis winding is located.

4.3.2 Cross Saturation Effect

If the cross coupling between d and q axis is considered, it means the mutual inductance L_{dq} is introduced in the machine model. When the saturation effect is considered in the machine model, the inductance matrix of IPMSMs can be expressed as (4.10) with L_{dq} being the cross-coupling transient inductance.

$$\boldsymbol{L}_s^{dq} = \begin{bmatrix} L_d & L_{qd} \\ L_{dq} & L_q \end{bmatrix} \tag{4.10}$$

The induced carrier current which is changed with the cross-saturation can be described as

$$\boldsymbol{i}_c^s = -j|\boldsymbol{i}_p|e^{j\omega_c t} - j|\boldsymbol{i}_n|e^{j(-\omega_c t+2\theta)} - |\boldsymbol{i}_{ndq}|e^{j(-\omega_c t+2\theta+\pi/2)} \tag{4.11}$$

where

$$|\boldsymbol{i}_p| = \frac{\Sigma L}{\Sigma L^2 - \Delta L^2 - L_{dq}^2}\frac{|\boldsymbol{u_c}|}{\omega_c} \tag{4.12}$$

$$|\boldsymbol{i}_n| = \frac{\Delta L}{\Sigma L^2 - \Delta L^2 - L_{dq}^2}\frac{|\boldsymbol{u_c}|}{\omega_c} \tag{4.13}$$

$$|\boldsymbol{i}_{ndq}| = \frac{L_{dq}}{\Sigma L^2 - \Delta L^2 - L_{dq}^2}\frac{|\boldsymbol{u_c}|}{\omega_c} \tag{4.14}$$

If the cross coupling between $d-$ and $q-$axis is considered, the mutual inductance L_{dq} is need to be calculated. Based on 2-D FEM the inductance is calculated from the flux linkage.

Fig. 4.3(d) shows the mutual inductance value L_{dq} of IPMSM-2. Because the inductance L_d and L_q is very small respectively, the L_{dq} is much smaller proximately 10% of the L_d value. When the current i_d is between $0A$ and -$15A$, the L_d value is much more significant.

Fig. 4.4(d) shows the mutual inductance value L_{dq} of IPMSM-3. The maximum of L_{dq} is also proximately 10% of the L_d value. When the current i_d is between 0A and -100A, the L_d value is much more significant.

Fig. 4.5(a) shows the mutual inductance L_{dq} of IPMSM-2 is changing with the injected current and rotor position. The results are obtained by FE (finite-element) simulations under various HF currents. The fundamental stator current is set as 50 A. The magnitude of the HF current has been set to 2, 4, 6 and 8 A, and the rotating current vector are injected directly into the stator of IPMSM-2. It can be seen that the mutual inductance L_{dq} changes very slowly based on different frequency.

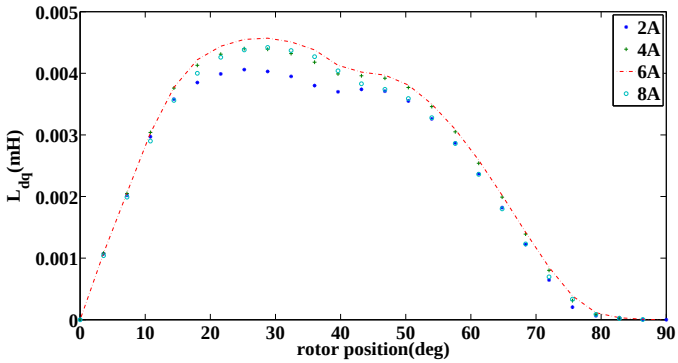

(a)

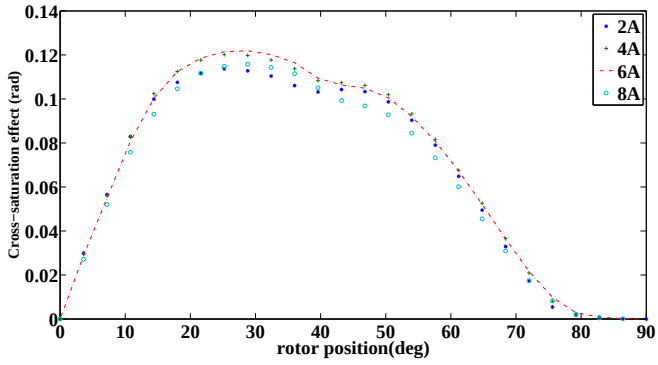

(b)

Figure 4.5: Cross-saturation effect of IPMSM-2 by FEM

Fig. 4.5(b) shows the cross-saturation effect of IPMSM-2 calculated by (4.15). For the novel IPMSMs, the cross-saturation effect in the induced carrier current

(4.11) is very small and the resulting position estimated error is also not significant.

$$\Phi = sin^{-1}(\frac{L_{dq}}{\Sigma L^2 - \Delta L^2 - L_{dq}^2}) \tag{4.15}$$

4.3.3 High Frequency Inductance Effect

If using the HF injection method for self-sensing control of IPMSMs, it is necessary to analyze the frequency response of inductances. Fig. 4.6 shows the results measured by the $Bode100$ which is a vector network analyzer. This impedance analyzer can get the transient impedances in a frequency range from 1 Hz to 40 MHz, when machines are operated at stand still.

Fig. 4.6(a) shows that the phase inductance between the phase endpoint and the neutral point for IPMSM-2 changes significantly when the frequency is between 10 Hz and 100 Hz. The inductances decrease slowly when the frequency is between 100 Hz and 1000 Hz, and this period with small variability is generally an attractive property for self-sensing control.

The line inductance between the phase endpoint and another for IPMSM-3 changes very slowly between 100 Hz and 1000 Hz in Fig. 4.6(b). The resonance effects at 35 Hz and 100 Hz can be explained as follows. At lower frequencies the serial stand-still inductance of IPMSM-3 is around 1 mH. The figure shows that the inductance starts decreasing at a frequency around 35 Hz and shows a resonance at 100 Hz. For a frequency higher than the resonance frequency, the coil has a capacitive behavior except within a small frequency range where it regains inductive characteristic. This indicates a parallel resonance as the inductance is active for low frequency whilst the capacitive part is active for high frequency.

The analysis of inductances with different frequency can help in the choice of HF signal which is important for self-sensing. Finally, the carrier frequency of the injected HF voltage needs to be chosen carefully. On the one hand, the frequency of the voltage injected needs to be chosen far from the fundamental machine operating frequency to achieve signal separation with high bandwidth and nearly zero phase distortion. On the other hand, the carrier frequency cannot be set too close to the switching frequency because the sinusoidal waveform injected will be distorted if there are not enough sample points in one sinusoidal cycle of the carrier high frequency voltage. Furthermore, considering the inductance, the choice of HF signal should avoid the wide variability period. In this chapter, 800 Hz is selected to ensure nearly a sinusoidal waveform with smaller harmonics.

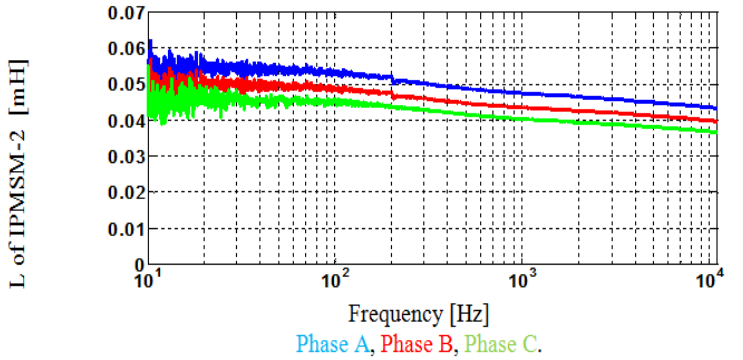

(a)

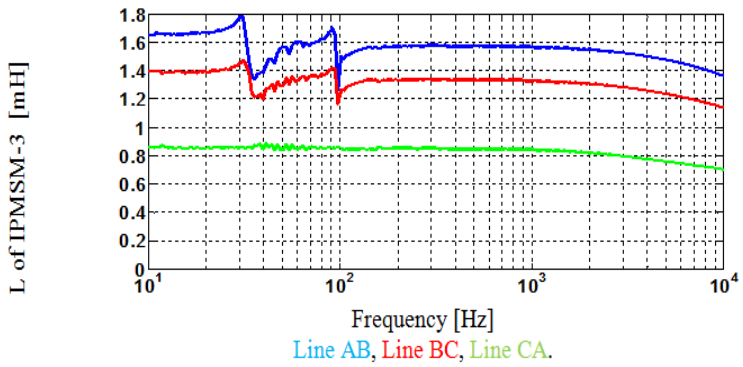

(b)

Figure 4.6: Transient inductances change with different frequency

4.3.4 High Frequency Resistance Effect

High frequency resistance is usually small and neglected in 4.5. However, in some cases, the high frequency resistance can be relatively large and can seriously degrade the estimation accuracy. Therefore, it is important to examine the high frequency resistance effect of IPMSMs.

Fig. 4.7(a) shows the transient resistance changing with different frequency, and it can be seen that the resistance of IPMSM-2 is almost constant when the frequency is between 10 Hz and 100 Hz. The resistance increases slowly when the frequency is between 100 Hz and 1000 Hz, and this period is the interesting area for the HF-based self-sensing control system. The resistance increases rapidly when the frequency is between 1000 Hz and 10000 Hz. The similar result for IPMSM-3 is shown in Fig. 4.7(b).

For the novel IPMSMs in this chapter the resistance effects with 800 Hz HF

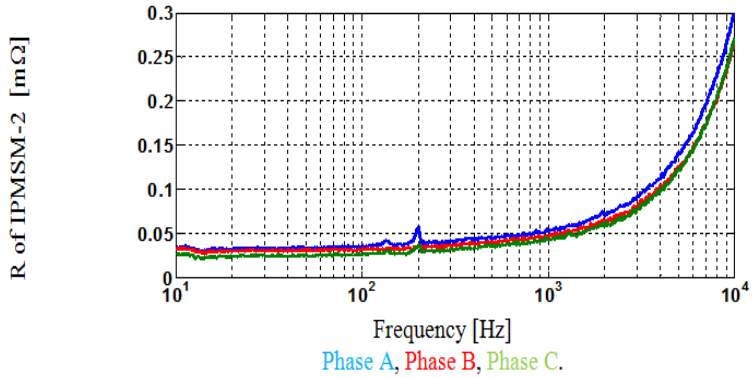

(a)

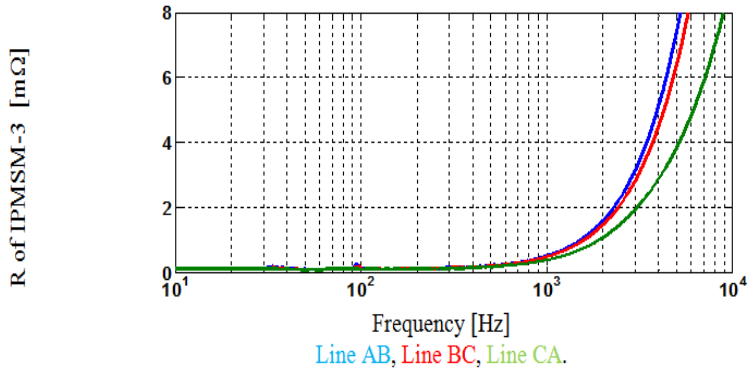

(b)

Figure 4.7: Transient resistance changes with different frequency

injection can be neglected due to the almost constant resistance characteristics.

4.3.5 FEM Results of Harmonic Distortion

It is known that the traditional CW-IPMSMs have the big disadvantage of more spatial harmonics and induce multi-saliencies. There are many reports describing that the harmonic distortion caused by secondary saliencies and saturation-induced saliencies are the main source of the estimation errors [15] [42] [106] [4].

When the harmonic distortion is considered, the induced carrier current can be

modeled as

$$\begin{aligned} \boldsymbol{i}_c^s = -j|\boldsymbol{i}_p|e^{j\omega_c t} + \sum_{i=1}^{n} |\boldsymbol{i}_{ni}|e^{j(-\omega_c t \pm h_i\theta)} \\ + \sum_{k=1}^{n} |\boldsymbol{i}_{nk}|e^{j(-\omega_c t \pm h_k\theta)} \end{aligned} \tag{4.16}$$

where $i = 2, 4, 6...$ are the even saliencies, and $k = 1, 3, 5...$ are the odd saliencies.

In order to make it clear how the multi-saliencies differ from the conventional designed CW-IPMSMs, both of the IPMSMs are analyzed with different load conditions based on 2-D FEM. The rotating current injection with high frequency of 800 Hz is used with an amplitude of 3 A for IPMSM-2, 10 A for IPMSM-3, respectively. The FEM results are analyzed when the machines are operated at stand still in this section.

The source of the even saliencies in (4.16) is magnetic saturation under loaded operation. They can be called saturation-induced magnetic saliencies which are even spatial harmonics. The odd saliencies in (4.16) have been explained by physical asymmetries in stator windings, dynamic eccentricity of the rotor under no-load, inverter switching harmonics and aliasing effects for phase current measurement. Only the even spatial harmonics are considered in FEM since these are load dependent [68].

The FEM results of IPMSM-2 under no-load can be seen in Fig. 4.8(a) and Fig. 4.8(b), that show the fast Fourier transform (FFT) analysis and trajectory of the nagative carrier current after the low pass filter. In Fig. 4.8(a) it includes the mainly useful 2^{nd} harmonic and the small 4^{th} and 6^{th} harmonics anisotropy. The trajectory in Fig. 4.8(b) is a likely circle and it is easy to do self-sensing control. Fig. 4.8(c) and Fig. 4.8(d) represent the current harmonics results of IPMSM-2 under half-load. In Fig. 4.8(c) it includes the mainly useful 2^{nd} harmonic and the small 4^{th}, 6^{th}, 10^{th} and 12^{th} harmonics anisotropy, and the trajectory in Fig. 4.8(d) is a circle with distortion. Fig. 4.8(e) and Fig. 4.8(f) show the current harmonics results of IPMSM-2 under full-load. In Fig. 4.8(e) it includes the mainly useful 2nd harmonic and the small 4^{th}, 6^{th}, 10^{th} , 12^{th} and 14^{th} harmonics anisotropy, and the trajectory distortion in Fig. 4.8(f) is more significant.

The FEM results of IPMSM-3 under no-load can be seen in Fig. 4.9(a) and Fig. 4.9(b), that indicate the nagative carrier current spectrum and trajectory after the low pass filter. In Fig. 4.9(a) it includes the mainly useful 2^{nd} harmonic and a small 4^{th} harmonic anisotropy. The trajectory in Fig. 4.9(b) is almost a circle. Fig. 4.9(c) and Fig. 4.9(d) show the current harmonics results of IPMSM-3 under half-load. In Fig. 4.9(c) it includes the mainly useful 2^{nd} harmonic and the small 4^{th},

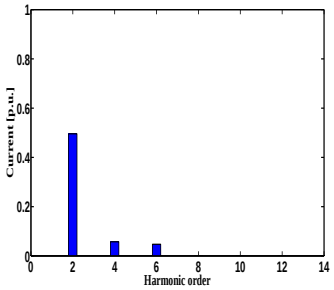

(a) The nagative carrier current spectrum of IPMSM-2 under 0 load

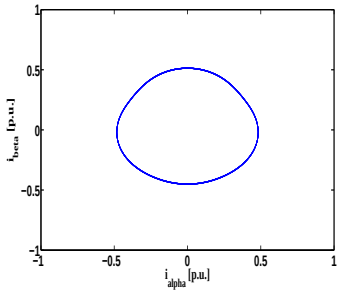

(b) The nagative carrier current trajectory of IPMSM-2 under 0 load

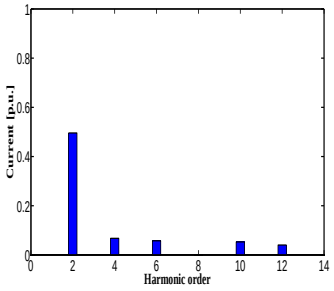

(c) The nagative carrier current spectrum of IPMSM-2 under half load

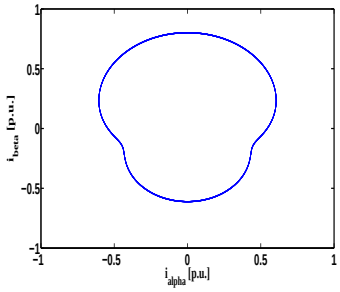

(d) The nagative carrier current trajectory of IPMSM-2 under half load

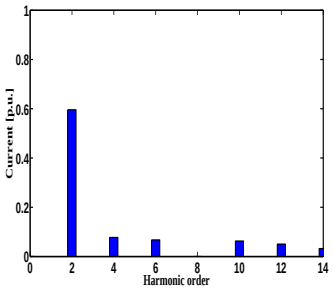

(e) The nagative carrier current spectrum of IPMSM-2 under full load

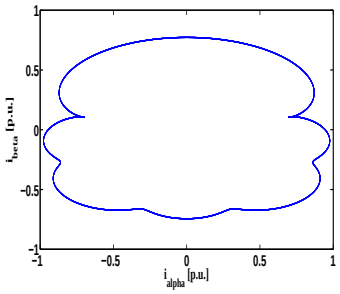

(f) The nagative carrier current trajectory of IPMSM-2 under full load

Figure 4.8: FEM results of the negative carrier current spectrum and trajectory after the low pass filter for IPMSM-2 based on different load conditions

8^{th}, 10^{th} and 12^{th} harmonics anisotropy, and the trajectory in Fig. 4.9(d) is a circle with distortion. Fig. 4.9(e) and Fig. 4.9(f) represent the current harmonics results of IPMSM-3 under full-load. In Fig. 4.9(e) it includes the mainly useful 2nd harmonic

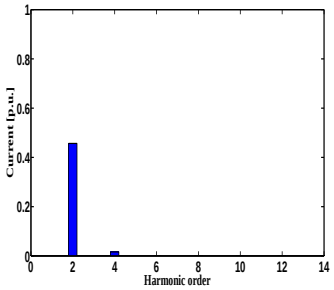

(a) The nagative carrier current spectrum of IPMSM-3 under 0 load

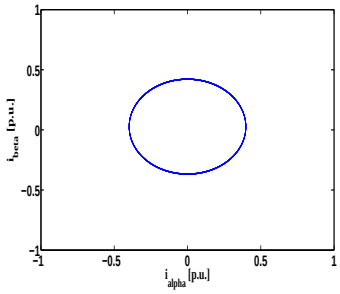

(b) The nagative carrier current trajectory of IPMSM-3 under 0 load

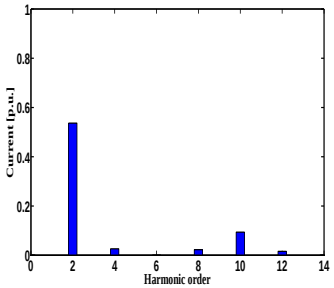

(c) The nagative carrier current spectrum of IPMSM-3 under half load

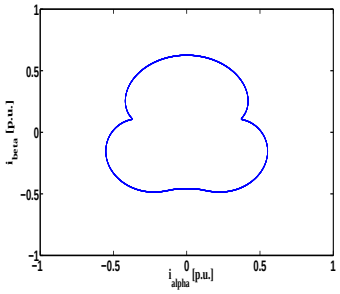

(d) The nagative carrier current trajectory of IPMSM-3 under half load

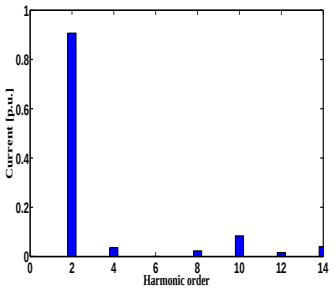

(e) The nagative carrier current spectrum of IPMSM-3 under full load

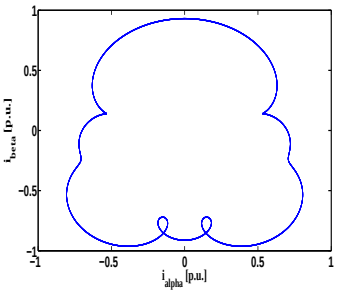

(f) The nagative carrier current trajectory of IPMSM-3 under full load

Figure 4.9: FEM results of the negative carrier current spectrum and trajectory after the low pass filter for IPMSM-3 based on different load conditions

and the small 4^{th}, 8^{th}, 10^{th}, 12^{th} and 14^{th} harmonics anisotropy, and the trajectory distortion in Fig. 4.8(f) is more significant.

The harmonic distortion simulated by FEM is not 100% accurate but this can

show the load dependency characteristics of the novel IPMSMs. It can be seen in Fig. 4.8 and Fig. 4.9 that the different current harmonics affect the current circle trajectory, which affects the estimation accuracy of self-sensing control. For the novel designed machines the distortion is not serious compared with the conventional machines which even can be a triangle trajectory.

4.4 Implementation and Experimental Results

4.4.1 Hardware Description

Both of the CW-IPMSMs test benches are based on the dSPACE real-time control platform, and there is no test bench for IPMSM-1 since it is only a simulation model. The control system utilizes the dSPACE development platform as the controller and generates the real-time code for the control algorithm and motor model. The control parameters can be tuned on-line.

The IPMSM-2 is supplied by a modified MACCON 2 k VA inverter which provides full control over the MOSFETs, and the actual rotor position is measured by a 4096 lines absolute encoder. The IPMSM-3 is supplied by a modified 50 k VA inverter which provides full control over the IGBT gates, and the actual rotor position is measured by a 4096 lines incremental encoder. In the experiments, the switching frequency of PWM for IPMSM-2 is 16 kHz, and for IPMSM-3 is 10 kHz. Fig. 4.10 shows the test benches of IPMSMs, and the technical data of IPMSMs is given in Table 4.2.

4.4.2 Experimental Results of Harmonic Distortion

The harmonic distortion can be easily seen from the experimental results of current. The rotating voltage injection with high frequency of 800 Hz is used with an amplitude of 3 V for IPMSM-2 and 10 V for IPMSM-3, respectively. Both machines are tested and measured at the electrical rotor speed of 4π rad/s (10 Hz) with the position encoder.

Fig. 4.11(a) and Fig. 4.11(b) shows the fast fourier transform (FFT) analysis of the negative current vector $\boldsymbol{i}_n$ under no-load, and the most noticeable secondary saliencies around the negative-sequence component are induced at $(-\omega_c - 2\omega_r)$ and $(-\omega_c \pm 4\omega_r)$. It can be seen the magnitude of the wanted $(-\omega_c + 2\omega_r)$ (780 HZ) component is definitely bigger than the even -2^{nd} and -4^{nd} harmonics. For the half-load condition in Fig. 4.11(c) and Fig. 4.11(d), the harmonic distortion is caused by saliencies that are induced at $(-\omega_c \pm 4\omega_r)$, $(-\omega_c \pm 6\omega_r)$, $(-\omega_c \pm 8\omega_r)$, $(-\omega_c \pm 12\omega_r)$, $(-\omega_c \pm 14\omega_r)$and $(-\omega_c - 2\omega_r)$. Furthermore, the magnitude of

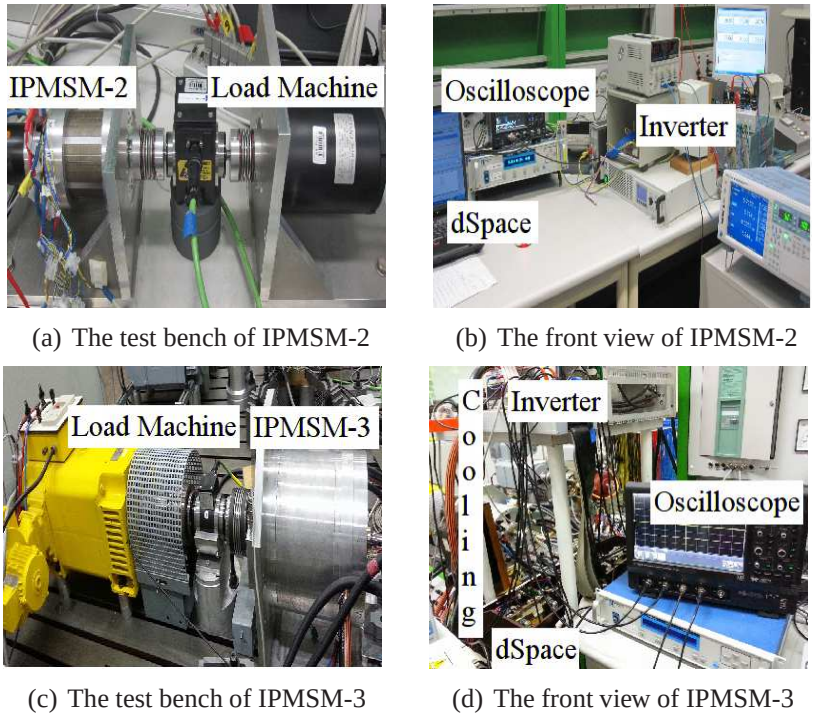

(a) The test bench of IPMSM-2 (b) The front view of IPMSM-2

(c) The test bench of IPMSM-3 (d) The front view of IPMSM-3

Figure 4.10: The test benches of novel IPMSMs

the $(-\omega_c + 2\omega_r)$ (780 HZ) component is bigger than that under no-load, and the magnitudes of the other harmonic orders are also increased. However, the increased harmonics compared with the dominant spatial saliency (780 Hz) are much smaller, whereas, these harmonics are very big in the conventional IPMSMs and have to use the decoupled compensation method.

Fig. 4.12 shows the carrier current sequence rotates at twice the electrical rotor speed with a likely circular trajectory without fundamental current when under no-load and half-load condition. The trajectory is normally not a circle for the conventional design IPMSMs especially under load. The novel designed IPMSMs have the big advantage of lower spatial harmonics, which induces the lower harmonic distortion of the current.

Since the harmonic distortion is not serious in the novel IPMSMs, it again proves that these new design are really attractive for self-sensing control especially based on a HF injection method and it makes accurately self-sensing control easily without decoupling the harmonic distortion. However, if some industry communities need very precisely self-sensing control performances, these novel IPMSMs also need to decouple the multi-saliencies harmonics.

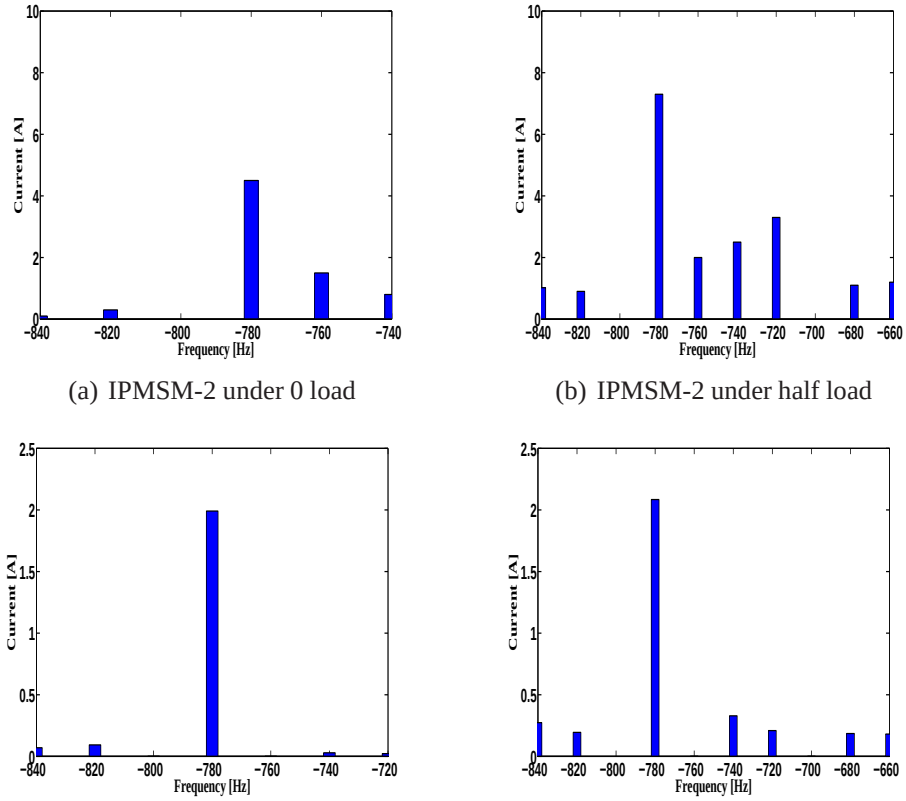

(a) IPMSM-2 under 0 load

(b) IPMSM-2 under half load

(c) IPMSM-3 under 0 load

(d) IPMSM-3 under half load

Figure 4.11: Measured negative carrier current spectrum in the stationary reference frame at ω_r=10 Hz(120rpm) with 3V carrier voltage at ω_c=800 Hz.

4.4.3 Experimental Results of Estimation Accuracy

Self-sensing performance of both machines in transient-state and steady-state with different load torque is investigated. The rotating voltage injection with high frequency of 800 Hz is used, with the amplitude of 3 V and 10 V for IPMSM-2 and IPMSM-3, respectively. Several tests with different operating points are perfected in the closed-loop control scheme without the position encoder. The experimental results of IPMSM-3 are presented here.

The step-speed state experimental results of IPMSM-3 can be seen in Fig.4.13. The speed increases from 0 rpm to 120 rpm and then decreases from 120 rpm to 0 rpm while the torque is constant as 30 Nm. Fig. 4.13 shows the full transient-state torque, estimated speed, estimated position and estimation error between the estimated position and the encoder position. The value of errors has small variability

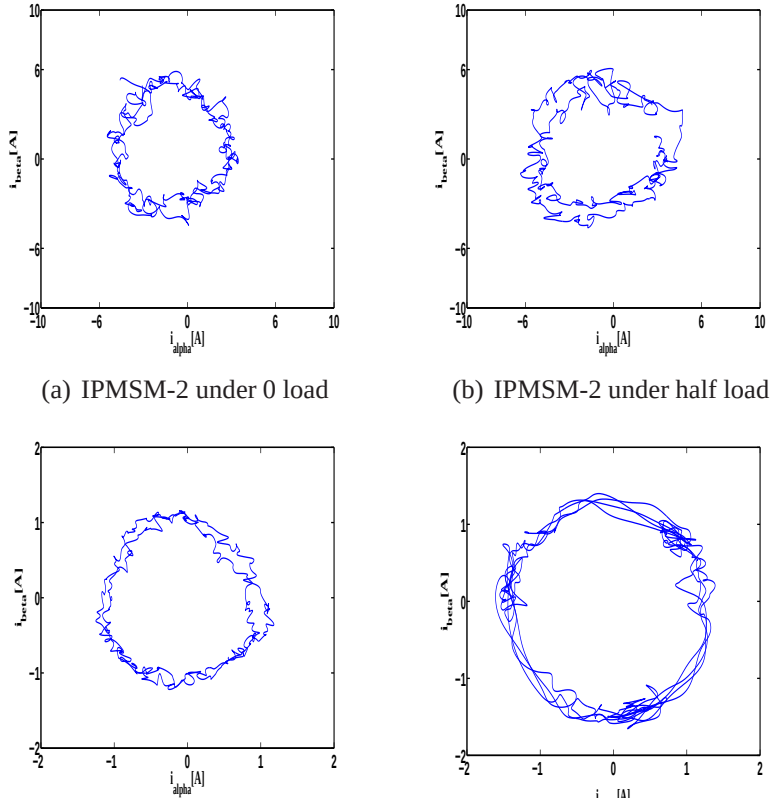

(a) IPMSM-2 under 0 load

(b) IPMSM-2 under half load

(c) IPMSM-3 under 0 load

(d) IPMSM-3 under half load

Figure 4.12: Measured negative carrier current in the negative reference frame at ω_r=10 Hz(120rpm) with 3V carrier voltage at ω_c=800 Hz.

in the constant speed. The big errors show up with the speed step-up from 0 rpm to 120 rpm and step-down from 120 rpm to 0 rpm, which is the dynamic disadvantage of self-sensing control.

It is important to point out that the rated torque of IPMSM-3 is 200 Nm and the experimental condition has limitation of reaching full load. That is why the FEM analysis is done in 4.3.5 based on different load conditions. The harmonic distortion of IPMSM-3 induced by the magnetic saturation under full loaded operation can be seen in Fig. 4.9. Based on the FEM results, the load dependency of IPMSM-3 can be supposed to be not very strong. With the speed step-up and step-down in Fig. 4.13, the estimated torque has a peak value of approximate rated-torque and the estimation error reaches maximum 0.5 rad. It proves the self-sensing control can work at the full load condition with the relative small estimation error.

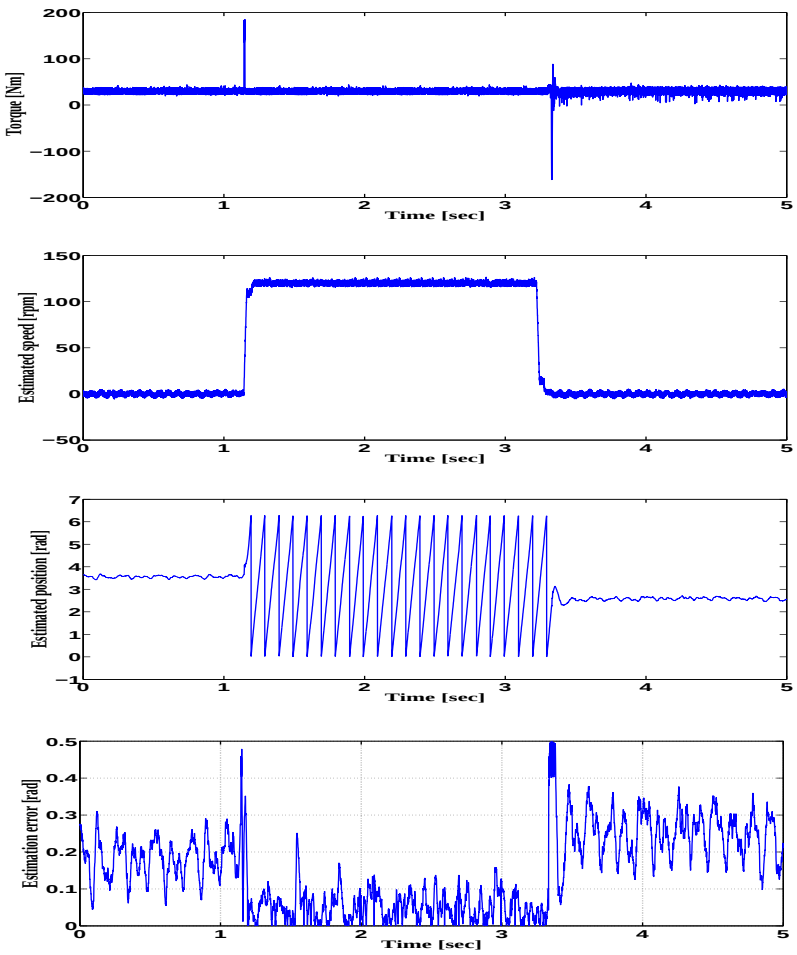

Figure 4.13: The self-sensing control of IPMSM-3 with 10 V carrier voltage at ω_c=800 Hz under 30 Nm load.

The second test is to verify the performance of self-sensing control of IPMSM-3 under the step-torque. The torque increases from 0 to 80 Nm while the speed is constant at 100 rpm. Fig. 4.14 shows the full transient-state torque, estimated speed, estimated position and estimation error between the estimated position and the encoder position. The value of errors has peak values when the load increases from 0 to 80 Nm.

The self-sensing control strategy presented here is the normal rotating high-frequency injection method without multi-saliencies decoupling compensation, and the experimental results show the good performance to prove the new machines are much more qualified to be controlled without an encoder.

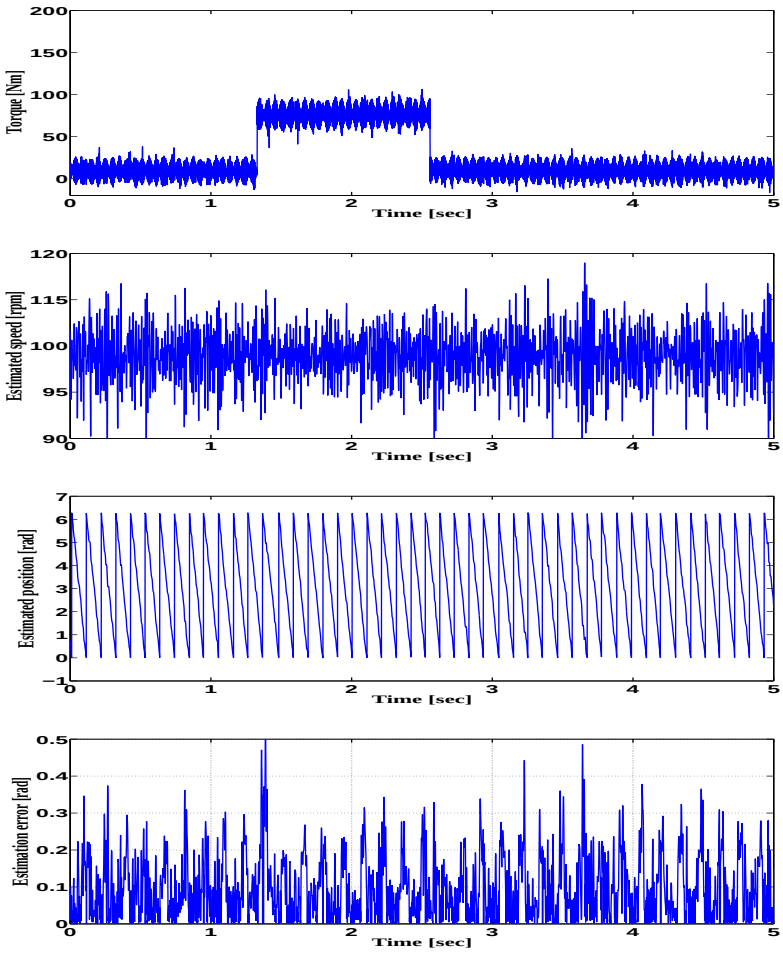

Figure 4.14: The self-sensing control of IPMSM-3 with 10 V carrier voltage at ω_c=800 Hz under step-load.

4.5 Summary

Self-sensing methods based on the tracking of saliencies have been demonstrated to estimate position/speed at zero & very low speed (0.03 p.u.). These methods use various forms of HF injection to estimate the spatial location of asymmetries. The asymmetries can be created specifically for the purpose of self-sensing but are often intrinsic to the magnetic/mechanical design of the machine.

It is important to point out the conventional design of CW-IPMSMs having the inherent disadvantage of more spatial harmonics and multi-saliencies, which are not attractive for self-sensing control based on the saliency-tracing method. This

chapter focuses on how the machine design affects the saliency-based self-sensing method.

There are two novel CW-IPMSM designs, and both of them have lower sub-harmonics content. The IPMSM-2 has fractional slot tooth concentrated windings using magnetic flux barriers in stator yoke. The IPMSM-3 has a new winding type consisting of two winding systems are shifted in space and time to each other for a specific angle, the number of slots per pole and per phase for the winding systems is different, and also the winding systems are characterized with a different number of turns per coil. Using such a combination, the specific MMF harmonics for the considered concentrated winding can be reduced or completely canceled.

According to these new machine design techniques, the two novel CW-IPMSMs for self-sensing application are tested and their characteristics are compared with the conventional machines. Both of them are attractive for self-sensing especially based on the HF injection method at low constant speed & torque with smaller estimation errors. It could be proved that the novel machine design can improve self-sensing capability and the estimation accuracy of self-sensing.

Considering the novel design of the CW-IPMSMs, the evaluation of self-sensing control is done to prove their design merit. The obtained results show that the new stator design brings significant advantages over the conventional design. The self-sensing control connected with the machine design is promising research for industry and will be a popular topic in the future. In order to get more accurate estimated results, especially for the CW-IPMSMs, the improvement of the machine design can be used to do high performance of self-sensing control.

CHAPTER 5

Losses Analysis in IPMSMs Resulting from HF Injection for Self-sensing Control

A novel designed CW-IPMSM with reduction of low space (low-order) harmonics named IPMSM-2 is introduced in Chapter 4. This chapter analyzes the eddy current loss distributions in IPMSM-2 using injection-based self-sensing position estimation. The novel machine design can reduce the influence of the HF signal induced iron and magnet losses for self-sensing control. Firstly, the magnetomotive force (MMF) of CW-IPMSMs with HF Injection between the single-layer and double-layer windings are compared. Secondly, the HF currents harmonics between the IPMSM-2 and the conventional IPMSM are compared. Finally, the general analytical solution is proposed to solve the losses calculation problem in IPMSMs, which is available for investigating the iron and magnet losses resulting from the HF injection.

5.1 New Stator Topology of IPMSM-2

The realization of the new stator core with flux barriers in the stator yoke can be performed by modifying the stator yoke structure in different ways such as using holes of different shapes, using stator slots with different slot depth or dividing completely the stator yoke in specific locations. Of course, as is mentioned previously, the new stator topology is related with different additional advantages receptively [27].

The new stator structure of IPMSM-2 is using different slot depth, and the coil-sides in the corresponding slots can be shift away from the slot-opening region to reduce proximity effect in the winding conductors which is presently mostly near

the slot opening [24]. The main geometry data of IPMSM-2 can be seen in Table 5.1, and the new stator topology is showed in Fig. 5.1.

Table 5.1: Main geometry data of IPMSM-2 [27]

Outer stator/rotor diameter	81mm/47mm
Gap length	0.5mm
Magnet length/width	3mm/10mm
Active length	70mm
Turns per phase	40

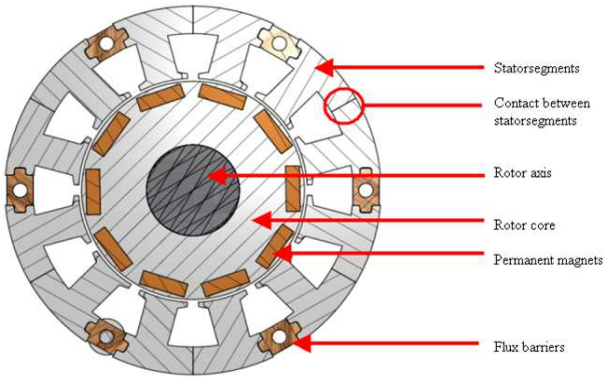

Figure 5.1: Cross section of IPMSM-2 [27]

Due to its special double-layer concentrated winding and notable topology, the IPMSM-2 shows enormous improvements on performances such as reduction of the sub- and high- magnetomotive force (MMF) harmonics more than 60% [30]. It also has the following advantages:

- Low cost (simple manufacturing)
- High efficiency (e.g. short end winding, low copper loss, low cogging torque and low torque ripple)
- High energy density (compact design)

5.2 Analysis of MMF with HF Injection

Since the MMF winding performances of PMSMs influence the power losses, the MMF performances need to be improved to get the machine losses reduction. It

has been proved double-layer windings are more preferable than single-layer ones in order to limit the losses, and IPMSM-2 also choose the double-layer windings to do design. Furthermore, the rotor iron and magnet losses resulting from HF as reported in [103], are primarily induced by spatial harmonics with respect to the flux density in the machines, and losses in the single-layer CW-SPMSMs can be higher than that in the double-layer ones. This section analyzes the MMF winding performances when the high frequency signal is injected into the conventional 12-slot/10-poles CW-IPMSMs with single-layer and double-layer windings.

It is important to point out that for the IPMSMs equipped with CW and fractional numbers, the torque is developed by the interaction of a specific high order of the stator MMF with the PMs. On the other side, the rest of others sub- and high-harmonics, which rotate with the different speed and in opposite directions, lead to additional stator and rotor iron losses, eddy current loss in the magnets, which are the main disadvantages of these winding types [107] [25].

Using Fourier series function the MMF distribution for the 12-slot/10-poles CW-IPMSMs can be described using the following (5.1) [25].

$$\mathbf{\Theta}\,(x,t) = \sum_{v} \frac{m}{2} \frac{2w\,{}^{v}\xi_{w}\,\hat{i}}{\pi v} \cos\left(\omega t - v\frac{\pi}{\tau_p}x + \delta\right) \tag{5.1}$$

with

$${}^{v}\xi_{w} = \cos\left(v\frac{5}{6}\frac{\pi}{2}\right)\sin\left(v\frac{1}{6}\frac{\pi}{2}\right)$$

where, m is number of phases ($m = 3$), ${}^{v}\xi_{w}$is the winding factor, $\hat{i}$ is the phase current amplitude, δ is the load angle, ω is the angular frequency, w is the number of turns per phase, and v is the space (MMF winding) harmonic.

When the rotating HF current injection signal with magnitude 15% of the rated current (I_rate) and frequency 1 kHz, (5.1) mentioned above is used to calculate the MMF. The distribution of MMF and the corresponding MMF spatial harmonics are shown in Fig. 5.2. For the 10-pole machines, only the 5^{th} stator spatial harmonic interacts with the field of the permanent magnets to produce continuous torque. The other MMF spatial harmonics, in particular the 1^{st}, 7^{th}, 17^{th}, etc., which have relatively large magnitudes, are undesirable and in some cases they limit the usefulness of this winding type in different specific applications [25].

It can be seen from the Fig. 5.2, the comparison between the single-layer and double-layer winding 12-teeth /10-poles IPMSM shows the MMF distribution cave of single-layer looks like a sine wave which is very different with double-layer (looks like a square wave). This is the visible difference between the single-layer and double-layer CW-IPMSM. The comparison of the corresponding MMF spectrum proves that double-layer CW IPMSM have smaller low space (low-order) har-

monics. That means the losses of double-layer CW IPMSM resulting from HF injection induced by low-order spatial harmonics are lower than single-layer CW IPMSM.

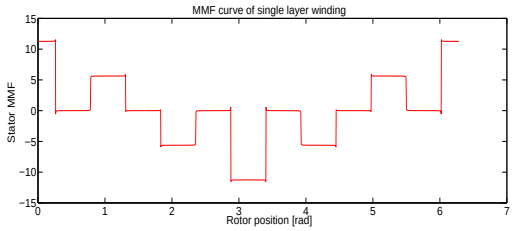

(a) Single-layer IPMSM MMF

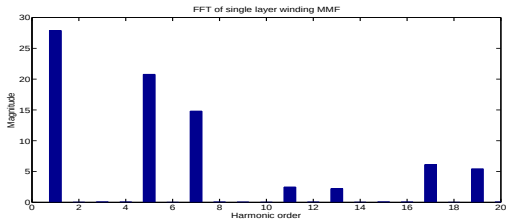

(b) Single-layer IPMSM MMF spectrum

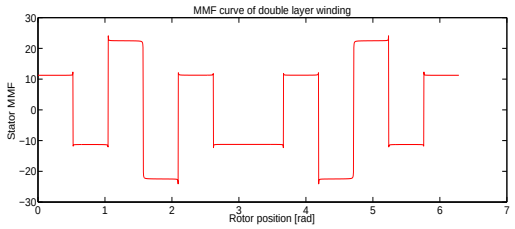

(c) Double-layer IPMSM MMF

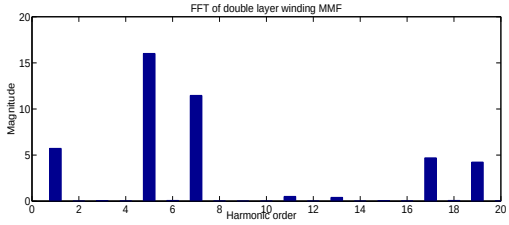

(d) Double-layer IPMSM MMF spectrum

Figure 5.2: MMF distribution and the corresponding MMF spectrum (Rotating HF injection 15% I_rate carrier current at 1 kHz)

5.3 Analysis of Losses by HF Currents Harmonics

The iron losses of electrical machines under conditions of sinusoidal magnetic fields, which is an ideal environment and many effects are ignored, can be roughly categorized as eddy current losses and hysteresis losses.

$$P_{iron}=P_{eddy}+P_{hyst}= k_e f^2 B^2+k_h f^a B^b \tag{5.2}$$

where f and B are the frequency and peak value of the flux density, respectively, whereas k_h, k_e, a and b are material constants.

When minor loops and dc bias on the hysteresis loss and time harmonics on the eddy-current loss are not ignored, eddy current loss and hysteresis loss are different with (5.2).

$$P_{eddy}=\frac{k_e}{2\pi^2} Mean\ Square\left(\frac{dB}{dt}\right)=k_e f^2 \sum_{h\geq 1} |hB_h|^2 \tag{5.3}$$

$$P_{hyst}=k_h f^a B^b(1+\frac{k}{B}\sum_{i=1}^{N} \triangle B_i) \tag{5.4}$$

where B is the peak flux density [T]; B_h is the amplitude of h^{th} flux density harmonic; $\triangle B_i$ is the flux reversal associated with a given minor loop [T]; N is the number of minor loops; and k is a constant in the range of 0.6 to 0.7.

PMSMs are generally considered to have negligible rotor losses, since the rotor rotates in synchronism with the fundamental stator MMF. However, the rotor pole pieces and the permanent magnets of PM synchronous machines are exposed to several time and space harmonics in the air-gap field which rotates at different speed with the rotor. This represents a source of losses which can be significant. Moreover, the high conductivity of permanent magnet materials leads to significant eddy current losses and this may cause the thermal demagnetization of magnets. Accordingly, the harmonic eddy current losses generated at the permanent magnet can be calculated as follows:

$$P_{eddy,mag}=\sum_n \int_V \frac{|J_n|^2}{2\sigma} dV \tag{5.5}$$

where n is the order of the time-harmonics, J_n is the armature current density, σ is the magnet resistivity, $P_{edd,mag}$ is the total magnet eddy current losses. Using the relation for the induced current density,

$$J_n = -\sigma \frac{\partial A_n}{\partial t} \tag{5.6}$$

the eddy current losses can be determined directly from the magnetic vector potential A_n as

$$P_{eddy,mag}=\sum_n \int_V \frac{\sigma}{2}\left(\frac{\partial A_n}{\partial t}\right)^2 dV \tag{5.7}$$

2D finite element method (FEM) formulated are used, and the comparison of air-gap flux density harmonics of conventional IPMSM and novel designed IPMSM-2 is shown is Fig. 5.3(a). According to the above equations, 2D-FEM formulated are used to analyze the stator iron losses, rotor iron losses and the magnet eddy current losses shown in Fig. 5.3(b). The flux barrier depth for the double-layer design is taken to be $0.65 * h_Y$, and h_Y denotes the stator yoke width.

The iron losses in the stator and rotor have direct relationship with the flux density B. The magnet losses have relationship with the current density, that means the time harmonics in the current waveform will effect the magnet eddy current losses.

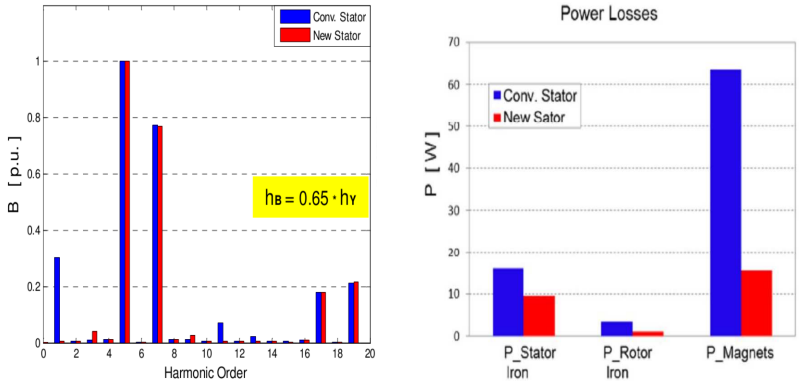

(a) Comparison of air-gap flux density harmonics

(b) Comparison of losses

Figure 5.3: Comparison between the conventional IPMSM and IPMSM-2 based on FEM [25]

All the above losses models and analysis are based on the traditional control drive system without HF injection. When the HF injection is considered, the FE-models also can be used. However, it will take a long time to calculate the HF losses and the dynamics of different frequencies at one simulation time can not be realized.

The HF losses can be analyzed according to the currents harmonics instead. During the experiments, the stator currents are much easier to be measured compared with the air-gap flux density of IPMSMs, and the relationship between flux linkage and stator current of IPMSMs is:

$$\frac{d\boldsymbol{\Psi}_s}{dt} = \boldsymbol{u}_s - R_s \boldsymbol{i}_s \tag{5.8}$$

When the HF signals are injected into the IPMSMs, the measured stator currents are provided by current sensor in the inverter. Fig. 5.4 shows the fast Fourier transform analysis of the stator currents. It can be seen that, the same results are shown as the FEM comparison of air-gap flux density harmonics. The low-oder stator current time harmonics of IPMSM-2 are much smaller than conventional IPMSM. Because the losses are nonlinear proportional to the flux density, and the flux density is nonlinear proportional to the stator current, the low-oder stator current time harmonics of IPMSM-2 are smaller that means the losses are smaller.

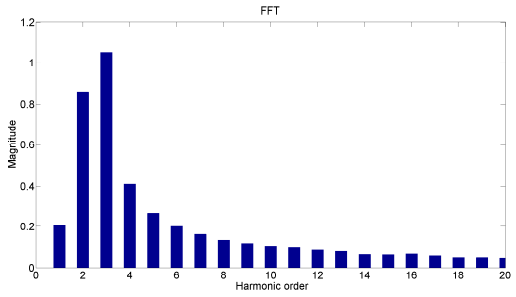

(a) Current harmonics spectrum of conventional IPMSM

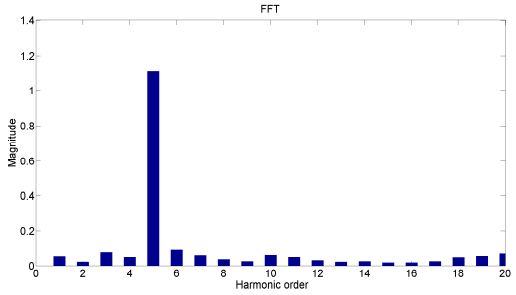

(b) Current harmonics spectrum of novel IPMSM-2

Figure 5.4: Comparison of currents harmonics for the two IPMSMs (Rotating HF injection 3V carrier voltage at 1000Hz)

5.4 Proposed Analytical Solution of Eddy Current Loss with HF Injection

Although the eddy current loss of IPMSMs can be calculated by utilizing 3-D FEM, it need relatively great calculation effort and does not provide as much insight as an analytical solution. Furthermore, the eddy current loss with HF injection in

IPMSMs is necessarily analyzed by analytical techniques, since the eddy current loss with HF injection may cause significant or extra heating of IPMSMs. This section proposes a general and simplified analytical method to calculate or predict the eddy current loss in IPMSMs by field solution.

5.4.1 Specified Boundary of IPMSM-2

To predict the eddy current loss in IPMSM-2, the time-varying field distribution is formulated in 2-D polar coordinates. It is known the magnetic field can only be calculated in the closed area. The IPMSM-2 is divided into 5 closed regions as 5 rings as shown in Fig. 5.5. In order to simplify the calculation and the model of field distribution, the following assumptions are made.

- End-effects are ignored;
- Induced eddy current is axially-directed;
- Each defined region is closed and the permeability variation in each region is neglected.

5.4.2 Loss calculation of IPMSM-2

To calculate the eddy current loss in defined regions, the available analytical method is based on the Poynting's theorem. Poynting's method eases the loss calculation when the model is formulated in polar co-ordinates, since the integration of Bessel functions with complex arguments is often problematic. Therefore, Poynting's theorem is employed, with (5.9) rewritten as:

$$P = \frac{1}{2\sigma} \int_{\theta_1}^{\theta_2} Re(J_z H_\theta^*)_{r=R} L_a R d\theta \tag{5.9}$$

where J is the eddy current density induced in axial direction, H_θ is the tangential component of the magnetic field at the surface of the conducting region of radius R, in which the average eddy current loss is to be calculated. θ_1 and θ_2 define the angle which is spanned by the conducting region, e.g. the pole-arc when calculating the loss per magnet segment, and 2π when calculating the loss in the retaining sleeve [108].

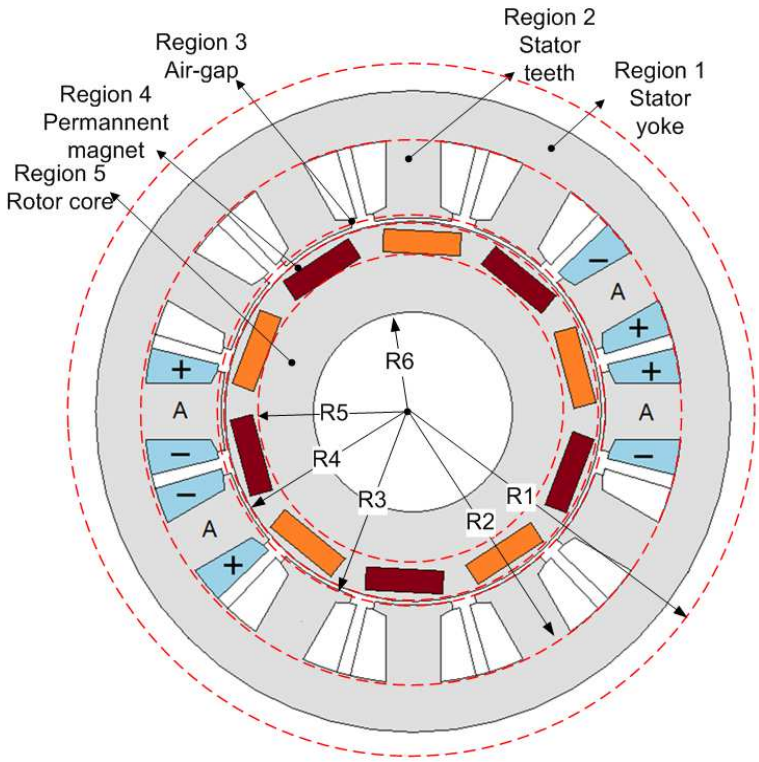

Figure 5.5: Specified boundary of the machine 1.Stator yoke. 2.Stator teeth.3.Air-gap. 4.Rotor magnet. 5.Rotor core.

A. Field Solution of Region Nr.1 (stator yoke)

From Poynting's method (5.9), the real parts of the complex variables magnetic field strength H and the eddy current density J are need to be calculated. The main problem is how to compute radiated fields from magnetic sources, and the relationships between the fields is shown in Fig. 5.6.

In polar cooridinate system, the analytical results of the vector magnetic potential A in the stator yoke can be derived by wave equation or the Laplacian equation which governs the time-varying field distribution in a boundary region (stator yoke region), as described in (5.10).

$$\bigtriangledown^2 A_1 + \beta_\rho^2 A_1 = 0 \tag{5.10}$$

with

$$\bigtriangledown^2 A_1 = \frac{\partial^2 A_1}{\partial r^2} + \frac{1}{r}\frac{\partial A_1}{\partial r} + \frac{1}{r^2}\frac{\partial^2 A_1}{\partial \phi^2}$$

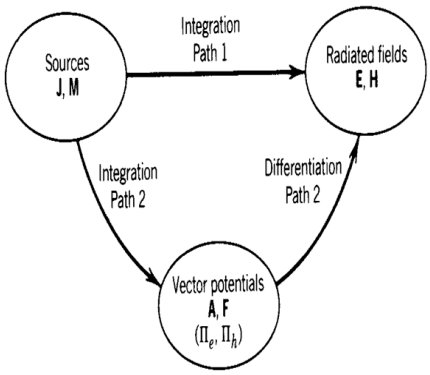

Figure 5.6: The relationships between the fields.

where, r is the radial length $(R1 < r < R2)$; R is the distance between the circle center and the outer border of the relative region shown in Fig. 5.5; β_ρ is the phase constant (rad/m); ϕ means the tangential component, and the subscript $_1$ means the region of Nr.1.

Based on the first and second order solution of Bessel function, the general solution of A_1 can be written as:

$$A_1(r,\phi) = \sum_{m=0}^{+\infty}[aJ_m + bY_m]cos(m\phi) \tag{5.11}$$

where, a and b are constants to be determined from the boundary conditions, and

$$\begin{aligned} J_m(\beta_\rho r) &= \textstyle\sum_{n=0}^{\infty} \dfrac{(-1)^n(\beta_\rho r/2)^{2n+m}}{(m!)((m+n)!)} \\ Y_m(\beta_\rho r) &= \dfrac{J_m(\beta_\rho r)cos(m\pi) - (-1)^n J_m(\beta_\rho r)}{sin(m\pi)} \end{aligned} \tag{5.12}$$

The radial and tangential flux density of region Nr.1 based on Maxwell equation can be expressed as:

$$\begin{aligned} B_{r1} &= \frac{1}{r}\frac{\partial A_1}{\partial \phi} \\ B_{\phi 1} &= -\frac{\partial A_1}{\partial r} \end{aligned} \tag{5.13}$$

The magnetic field can be calculated as:

$$\begin{aligned} H_{r1} &= \frac{1}{\mu_{r1}}B_{r1} \\ H_{\phi 1} &= \frac{1}{\mu_{r1}}B_{\phi 1} \end{aligned} \tag{5.14}$$

where μ_{r1} is the relative permeability of the stator yoke.

The boundary conditions are shown in:

$$\begin{aligned} B_{r1}|_{r=R1} &= 0 \\ B_{\phi 1}|_{r=R1} &= 0 \end{aligned} \tag{5.15}$$

B. Field Solution of Region Nr.2 (stator teeth)

Different with region 1, the area of stator teeth can be seen as an area with loss and excitation source. When the wave equation is used to calculate the vector magnetic potential A_2, the alternative function is described as:

$$\bigtriangledown^2 A_2 + \beta_\rho^2 A_2 = \mu_{r2} J_2 \tag{5.16}$$

where J_2 is the induced eddy current density of stator teeth.

The solution of A_2 is:

$$A_2(r,\phi) = \sum_{m=0}^{+\infty} [aJ_m + bY_m] cos(m\phi) + E_0 \tag{5.17}$$

where, $R2 < r < R3$, a and b are constants to be determined from the boundary conditions; J_m and Y_m are the same as described in (5.12); one may utilize the wave equation and appropriate boundary conditions to yield a specific solution E_0.

The boundary conditions seen in (5.18) can be used to so the anti-solution for coefficient in (5.17).

$$\begin{aligned} B_{r1} &= \frac{1}{r}\frac{\partial A_1}{\partial \phi} = B_{r2} = \frac{1}{r}\frac{\partial A_2}{\partial \phi} \\ B_{\phi 1} &= -\frac{\partial A_1}{\partial r} = B_{\phi 2} = -\frac{\partial A_2}{\partial r} \end{aligned} \tag{5.18}$$

One key point of region 2 is the equivalent excitation current density which can take into account of the space harmonics of the stator MMF due to stator slotting and the time harmonics due to the non-sinusoidal stator phase current. To achieve the equivalent current density, a proposed solution in [109] is employed, which introduces an approximate relationship between the max values of stator winding MMF ($\boldsymbol{\Theta}\ (x,t)_{max}$) and equivalent excitation stator current $\boldsymbol{I}_{v_{max}}$, as expressed in:

$$\boldsymbol{\Theta}\ (x,t)_{max} = \frac{2}{\pi}\boldsymbol{I}_{v_{max}}\frac{\tau_{pv}}{2} \tag{5.19}$$

where,

$$\boldsymbol{\Theta}\ (x,t) = \boldsymbol{\Theta}\ (x,t)_{max}\, cos(v\theta) \tag{5.20}$$

and

$$\boldsymbol{I}_v(\theta) = \boldsymbol{I}_{v_{max}} cos(v\theta) \tag{5.21}$$

where, p is the number of poles, v is the space harmonic order $v = 1, 3, 5, ..., \infty$, and $\tau_{pv} = 2\pi \dfrac{R2}{pv}$.

Based on winding type, the stator winding MMF of IPMSM-2 can be obtained as (5.1), the winding factor for the new 12-slots/10-poles winding with winding coils with different turns per coil side (Fig. 5.7) can be described as,

$$^{v}\xi_{w,new} = \frac{n_2}{n_2 + n_1}[sin(v\frac{\pi}{2}) - sin(v\frac{\pi}{3})] + \frac{n_2 - n_1}{n_2 + n_1} sin(v\frac{\pi}{3}) \tag{5.22}$$

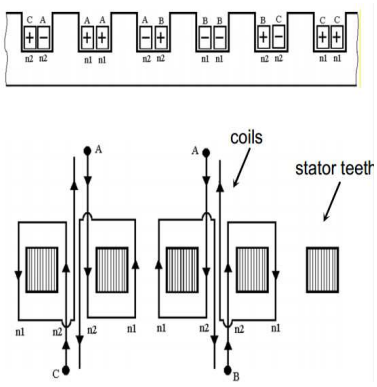

Figure 5.7: 12-teeth /10-poles winding topology with different number of turns per coil side. [25]

The equivalent excite current results in:

$$\boldsymbol{I}_v(\theta) = \frac{(\boldsymbol{\Theta}\ (x,t)\ \pi)}{\tau_{pv}} \tag{5.23}$$

The equivalent excite current density is:

$$J_2 = \frac{I_v(\theta)}{S_2} \tag{5.24}$$

where, S_2 is the acreage of stator teeth area.

C. Field Solution of Region Nr.3 (air-gap)

Boundary region Nr.3 is the air-gap area without loss and source-free, and the wave equation (5.26) is used to solve A_3.

$$\nabla^2 A_3 + 0 = 0 \tag{5.25}$$

i.e.

$$\frac{\partial^2 A_3}{\partial r^2} + \frac{1}{r}\frac{\partial A_3}{\partial r} + \frac{1}{r^2}\frac{\partial^2 A_3}{\partial \phi^2} = 0 \tag{5.26}$$

where, $R3 < r < R4$.

The general solution of A_3 is:

$$A_3(r,\phi) = \sum_{n=1}^{+\infty}\sum_{m=-\infty}^{+\infty}[ar^m + br^{-m}]sin(n\omega_r t + v\alpha + \theta_u) \tag{5.27}$$

where a and b are constants to be determined from the boundary conditions, n is the order of time harmonic, v is the order of spatial harmonic , and θ_u is the phase angle of current harmonic.

D. Field Solution of Region Nr.4 (permanent magnet)

Boundary region Nr.4 ($R4 < r < R5$) is the rotor magnet area with loss and source, and the field solution is the same as that for region Nr.2. However, the analytical method can not get the material properties. Especially based on different frequency the B-H curve is different. Therefore, the flux density of boundary area Nr.4 need to be corrected by using FEM.

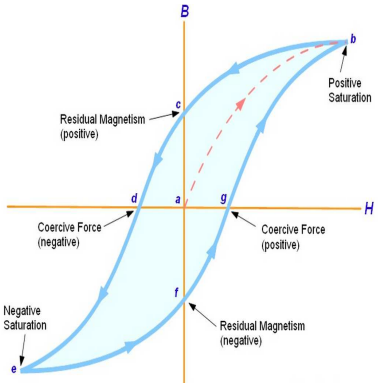

Figure 5.8: A B-H curve for a typical ferromagnetic material [110].

The corrected radial and tangential flux density can be expressed as:

$$\begin{aligned} \hat{B}_{r4} &= \frac{1}{r}\frac{\partial \hat{A}_4}{\partial \phi} \\ \hat{B}_{\phi 4} &= -\frac{\partial \hat{A}_4}{\partial r} \end{aligned} \tag{5.28}$$

5.5 Summary

Based on the HF injection method, two 12-teeth/10-poles PM machines with different windings layer are investigated and their performances are compared. The analysis verified that the conventional 12-teeth/10-poles PM machine with double-layer windings has reduced 1^{st}, 7^{th} and 13^{th} MMF harmonics significantly.

A novel method for reducing the sub-harmonics of the air-gap flux density for the fractional slot tooth (12-teeth/10-poles) concentrated windings using flux barriers in stator yoke is presented. Considering the losses, the obtained results show that the new stator design brings significant advantages of reduced losses over the conventional design. The experimental results of the stator current with HF injection signal prove the efficiency improvement of the novel designed machine.

Since the HF injection method is so attractive for self-sensing control of PMSMs, the HF losses need to be researched. Up to now, the HF losses have not been investigated very much and the analytical method has not been applied in this filed.

The analytical solution of the eddy current loss model for IPMSM is proposed in this chapter. It considers the stator windings type and the non-linear performance of the permanent magnet. The accuracy of the proposed solution can be improved by simplified equivalent exciting stator current method and the iteration of the hysteresis loop of PM.

For the purpose of finding a balance between the cost of the position encoder and the extra HF losses consumption, the novel machine design is considered. It is difficult to find a loss minimization control algorithm for HF injection-based self-sensing control scheme directly. In order to prove the HF losses of the novel machine are reduced compared with the conventional ones, more analysis and experiments need to do in the future.

CHAPTER 6

Observer-based Self-sensing Model Predictive Control of IPMSMs

Although the observer-based self-sensing control techniques are very popular and universal, the model predictive control (MPC) schemes are not developed based on all types of observers. Observer is the key technology for next generation motor drives. Observer-based state filters are in order to reduce parameter sensitivity. Speed-adaptive full-order observers are, arguably, the most popular schemes based on the fundamental excitation, due to their accuracy and versatility. Most adaptive schemes employ the linear time-variable motor model, and are realized as Luenberger observers, sliding mode observers, or Kalman filters. Usually, these observers are realized in a single reference frame and, whatever that frame is, at least one term of the motor model contains the rotor speed. Thus, the observer must be speed adaptive.

This chapter will explain how to use the saliency tracking observer for the position & speed estimations, and introduce the Gopinath-style flux linkage observer for the flux estimation in the model predictive control with finite control set (FCS-MPC) scheme. In implementation, the Gopinath-style observer is considered for obtaining good flux estimation, and the saliency tracking observer can get accurate position & speed estimations. The experimental results confirm that this control strategy has very fast dynamics and it can adapt a very wide speed range and shows good performance both at transient and steady states.

6.1 Model Predictive Torque Control with Finite Control Set of IPMSMs

The electromagnetic torque of IPMSMs is given as

$$T_e = \frac{3}{2}P(\psi_{PM} i_q + (L_d - L_q) i_d i_q) \tag{6.1}$$

For the IPMSMs the relations between the stator and rotor flux, current, speed and electromagnetic torque can be described as the following ordinary differential equations (ODEs):

$$\frac{d\mathbf{i}_s}{dt} = \mathbf{L}_s^{-1}(\mathbf{u}_s - R_s \mathbf{i}_s - \frac{\partial \mathbf{L}_s}{\partial \theta} - j\omega \mathbf{\Psi}_{PM}) \tag{6.2}$$

$$\frac{d\omega}{dt} = \frac{P}{J}(T_e - T_L) \tag{6.3}$$

$$\frac{d\theta}{dt} = \omega \tag{6.4}$$

Internal discrete-time model of the electric drive is necessary, which is used to predict the future evolution of the controlled output variables for a sequence of control inputs over a prediction horizon (one sampling period T_s). The FCS-MPC is based on the Euler method to predict the flux and electromagnetic torque in the electric drives, and the forward Euler discretization is shown:

$$\frac{dx}{dt} = \frac{x(k+1) - x(k)}{T_s} \tag{6.5}$$

Omitting the tedious derivation a standard discrete current function of PMSM can be described as (6.6). The coefficient matrices are described in (6.7), (6.8) and (6.9).

$$\hat{\mathbf{i}}_s(k+1) = A\mathbf{i}_s(k) + B\mathbf{u}_s(k) + C \tag{6.6}$$

where

$$A = \begin{bmatrix} 1 - \dfrac{R_s T_s}{L_d} & \dfrac{L_q T_s \omega_e(k)}{L_d} \\ -\dfrac{L_d T_s \omega_e(k)}{L_q} & 1 - \dfrac{R_s T_s}{L_q} \end{bmatrix} \tag{6.7}$$

$$B = \begin{bmatrix} \dfrac{T_s}{L_d} & 0 \\ 0 & \dfrac{T_s}{L_q} \end{bmatrix} \tag{6.8}$$

$$C = \begin{bmatrix} 0 \\ -\dfrac{-\psi_{PM} T_s \omega_e(k)}{L_q} \end{bmatrix} \tag{6.9}$$

Based on the machine model, the stator flux and electrical torque at $(k+1)^{th}$ sampling period can be predicted as:

$$\hat{\mathbf{\Psi}}_s(k+1) = \mathbf{\Psi}_s(k) + (\mathbf{u}_s(k) - R_s \mathbf{i}_s(k)) T_s \tag{6.10}$$

$$\hat{T}_e(k+1) = \frac{3}{2} P \hat{\mathbf{\Psi}}_s(k+1) \hat{\mathbf{i}}_s(k+1) \tag{6.11}$$

Considering the discrete nature of power converters, it is possible to simplify the optimization problem of MPC by avoiding the use of modulators. Taking into account the finite set of possible switching states of the power converter, which depends on the possible combinations of the on/off switching states of the power switches, the optimization problem is reduced to the evaluation of all possible states and the selection of the one which minimizes the given cost function. In addition to this, if the horizon length is set to $N = 1$, the calculation of the optimal actuation is very simple and easy to implement experimentally, as will be shown in this chapter.

The proposed model predictive torque control method is a FCS-MPC method which is designed by pre-considering a torque-band. An appropriate cost function is defined as following:

$$g = |T_e^*(k) - \hat{T}_e(k+1)| + g||\mathbf{\Psi}_s(k)|^* - |\hat{\mathbf{\Psi}}_s(k+1)|| \tag{6.12}$$

where $T_e^*(k)$ is the reference torque and $\hat{T}_e(k+1)$ is the predicted electrical torque for a given switching state, $|\mathbf{\Psi}_s(k)|^*$ is the reference amplitude for the stator flux, and $|\hat{\mathbf{\Psi}}_s(k+1)|$ is the amplitude of the predicted stator flux. The weighting factor g allows one to adjust the importance of the flux error with respect to the torque error.

The optimization method of FCS-MPC focuses on the flux error. Therefore, accurate flux estimation is very important to this control scheme. In the conventional FCS-MPC method, the flux is calculated directly by the equations of discrete machine model. However, IPMSM state equations contain cross-coupling stator flux linkage. Flux observer which can do the decoupling is necessary for FCS-MPC technology.

6.2 Gopinath-Style Stator Flux Linkage Observer

Since stator flux linkage is not measurable, modified Gopinath-style flux linkage observers have been developed to estimate stator flux linkage in the continuous

time domain for induction machines [58] and IPMSMs [57]. The Gopinath-style flux observers have been developed in the discrete time domain [111] for induction machines. A discrete time model of the Gopinath-style stator flux linkage observer for IPMSMs is proposed in [36] which is shown in Fig. 6.1.

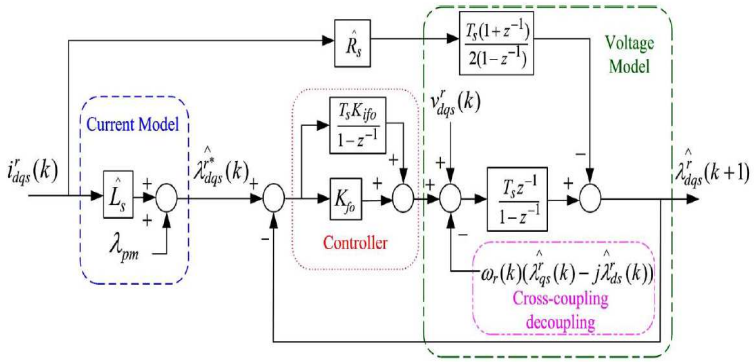

Figure 6.1: Discrete time model of the Gopinath-style stator flux linkage observer [36].

The Gopinath-style stator flux linkage observer is based on a current model and a voltage model. First, the stator flux linkage is estimated through a current model. The current model is developed based on the stator flux linkage and current equation shown as:

$$\psi_d = L_d i_d + \psi_{pm} \tag{6.13}$$

The next step is to estimate the stator flux linkage via a voltage model-based observer; the IPMSMs state equations including the stator flux linkage are repeated for convenience.

$$\begin{aligned} u_d &= R_s i_d + \tfrac{d}{dt}\psi_d - \omega_r \psi_q \\ u_q &= R_s i_q + \tfrac{d}{dt}\psi_q + \omega_r \psi_d \\ u_{dq} &= R_s i_{dq} + \tfrac{d}{dt}\psi_{dq} + j\omega_r \psi_{dq} \end{aligned} \tag{6.14}$$

It can be seen the state equations of IPMSM contain cross-coupling stator flux linkage. The stator flux linkage is decoupled to simplify the stator flux linkage observer model and to eliminate effect of the cross-coupling. Then the voltage model in the continuous time can be approximated as following:

$$\begin{aligned} u_d &= R_s i_d + \tfrac{d}{dt}\psi_d \\ u_q &= R_s i_q + \tfrac{d}{dt}\psi_q \\ u_{dq} &= R_s i_{dq} + \tfrac{d}{dt}\psi_{dq} \end{aligned} \tag{6.15}$$

The Gopinath-style stator flux linkage observer utilizes a controller between the current and voltage models. To estimate the stator flux linkage in a discrete time domain, a discrete time model of the stator flux linkage should be developed seen in Fig. 6.1.

This chapter will combine the Gopinath-style stator flux linkage observer with the FCS-MPC. The estimated stator flux linkage of the next sampling time is used as the flux prediction value to solve the optimization problem, which can be seen in Fig. 6.7.

6.3 Full-order Luenberger Rotor Position Observer

This section develops an effective self-sensing control of PMSM drive by using a full-order Luenberger state observer for the rotor position estimation. The observer is based on the $\alpha\beta$ stator reference frame dynamic model and no mechanical parameters are involved. Its structure is therefore very simple, and it can be realized at a low computation burden.

The circuit equation of a IPMSM in the $\alpha\beta$ reference frame can be transformed from (6.2) in the abc reference frame and results in:

$$\dot{i}_{\alpha\beta} = \frac{1}{L_d}\mathbf{u}_{\alpha\beta} - \frac{R_s}{L_d}\mathbf{i}_{\alpha\beta} - j\omega(L_d - L_q)\mathbf{i}_{\alpha\beta} + \mathbf{e}_0 \tag{6.16}$$

where

$$\mathbf{e}_0 = [\omega\psi_{PM} - (L_d - L_q)\frac{1}{i_q} - \omega(L_d - L_q)i_d]e^{j(\theta+\pi/2)} \tag{6.17}$$

The state and output equations of IPMSMs are

$$\begin{aligned} \dot{\mathbf{x}} &= A\mathbf{x} + B\mathbf{u} \\ \mathbf{y} &= C\mathbf{x} \end{aligned} \tag{6.18}$$

where

$$\mathbf{x} = [i_\alpha \; i_\beta \; \psi_{PM\alpha} \; \psi_{PM\beta}]^T \tag{6.19}$$

$$\mathbf{u} = [u_\alpha \; u_\beta]^T \tag{6.20}$$

$$\mathbf{y} = [i_\alpha \; i_\beta]^T \tag{6.21}$$

$$A = \begin{bmatrix} -\frac{R_s}{L_q} & \omega\frac{L_q}{L_d} & 0 & 0 \\ -\omega\frac{L_d}{L_q} & -\frac{R_s}{L_q} & -\frac{\psi_{PM}}{L_q} & 0 \\ 0 & 0 & 0 & 0 \\ 0 & 0 & 1 & 0 \end{bmatrix} \tag{6.22}$$

$$B = \begin{bmatrix} \frac{cos\theta}{L_d} & \frac{sin\theta}{L_d} \\ -\frac{sin\theta}{L_q} & \frac{cos\theta}{L_q} \\ 0 & 0 \\ 0 & 0 \end{bmatrix} \tag{6.23}$$

$$C = \begin{bmatrix} cos\theta & -sin\theta & 0 & 0 \\ sin\theta & cos\theta & 0 & 0 \end{bmatrix} \tag{6.24}$$

With angular velocity considered to be a slowly varying parameter,6.18 may be used to construct a full order observer [112]. The motivation of the full order observer is to estimate the states which cannot be measured directly in practice. By full order observer, the immeasurable states can be reconstructed by other measurable states. Thereby, a new system can be artificially constructed and it is same to the original system, so the state variables in the reconstructed system can be measured or calculated. The observer structure is shown in Fig. 6.2.

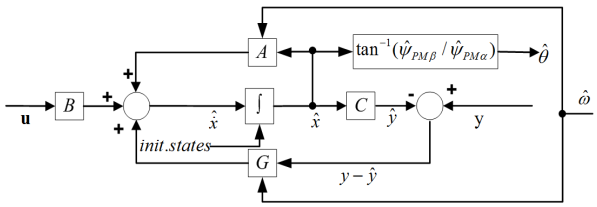

Figure 6.2: The full-order Luenberger rotor position observer.

The observer [113] is used to estimate the state vector $\boldsymbol{x}$ of (6.19) from knowledge of the input vector $\boldsymbol{u}$ and a direct measurement of the output vector $\boldsymbol{y}$. Note that from the estimation of $\psi_{PM\beta}$ and $\psi_{PM\alpha}$, the rotor position estimated value $\hat{\theta}$ may be determined from:

$$\hat{\theta} = tan^{-1}(\frac{\hat{\psi}_{PM\beta}}{\hat{\psi}_{PM\alpha}}) \tag{6.25}$$

Using standard observer design techniques for a linear system, the form of the rotor position observer is:

$$\dot{e} = (A - GC)e \tag{6.26}$$

Here G is the observer gain matrix, $\hat{\boldsymbol{x}}$ indicates the estimated state vector, and e is the state estimation error vector:

$$e = \boldsymbol{x} - \hat{\boldsymbol{x}} \tag{6.27}$$

Convergence of the estimated states toward their actual values is achieved by conventional eigenvalue placement techniques. That is, the eigenvalues of the characteristic equation (6.28) are chosen to have negative real components so that asymptotic state reconstruction is achieved.

$$|\lambda I - (A - GC)| = 0 \tag{6.28}$$

Clearly, observability of the system is a requirement for the estimation of PMSM states. The condition for observability is determined by the rank of the observability matrix:

$$\begin{bmatrix} C & CA & CA^2 & CA^3 \end{bmatrix}^T \tag{6.29}$$

The observability matrix of (6.29) is full rank for nonzero angular velocity so that the system is observable under those conditions. This result supports the well-known drawback of the self-sensing for PMSMs, its inability to estimate rotor angle at zero and low angular velocities.

Given the ill-conditioning of the rotor position observer at standstill, special provisions must be made to start the self-sensing for PMSMs and to operate the system at extremely low angular velocity. To accommodate this, the observer gain matrix G is set to zero at speeds below an experimentally determined low-speed threshold.

The presence of noise on the measured signals results in noisy position estimates when using direct calculation methods such as the $arctan$ i.e tan^{-1} in the full-order Luenberger rotor position observer. To reduce the noise problem, filters have been applied to either the estimated position or the input signals, adding lag to the estimate. It is necessary to improve the estimation method which is introduced in the following section.

6.4 Enhanced Luenberger-style Saliency Tracking Rotor Position Observer

A tracking observer is an alternative estimation method instead of direct calculation using the $arctangent$ of the two input signals. By using an observer, noise on the position signals can be filtered without adding lag to the estimate.

This section shows how to improve the saliency-based EMF methods by using an observer to estimate the motion states. The observer-based back-EMF tracking method proposed by Kim [114]. This method uses a stationary reference frame back-EMF state filter (Fig. 6.3) to estimate the back-EMF $\hat{E}^s_{sal-dqs}$ in cascade with an enhanced Luenberger-style back-EMF tracking observer (Fig. 6.4) for tracking

the mechanical rotor position $\hat{\theta}$ and velocity $\hat{\omega}$. The stationary reference frame back-EMF state filter is based on the extended EMF model, which allows it to be used with both interior and surface PMSMs. The enhanced Luenberger-style back-EMF tracking observer provides estimated rotor position $\hat{\theta}$ and velocity $\hat{\omega}$. It also filters noise from the estimated back-EMF signal but provides zero-phase lag estimation of velocity and position because of the torque command feedforward. Finally, it also provides an estimate of shaft disturbance (load) torque $\hat{T}$, as shown in Fig. 6.4.

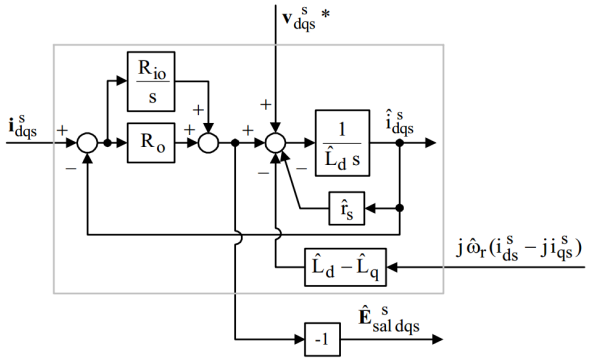

Figure 6.3: Block diagram of the stationary reference frame state filter used to estimate back EMF [114].

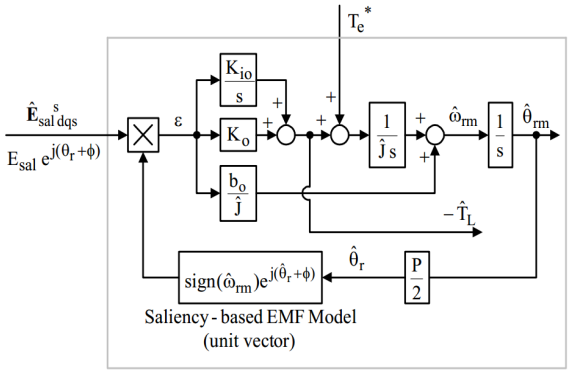

Figure 6.4: Block diagram of the enhanced Luenberger-style back-EMF tracking observer used to estimate position, velocity, and load torque [114].

In the application of standard back-EMF-based methods to IPMSM, transformation of the IPMSM model into an estimated rotor frame results in undesirable terms

due to the saliency. In some methods of position estimation, the terms are ignored, resulting in performance degradation. In order to solve this problem, the IPMSM model in the dq reference frame can be rewritten as

$$\mathbf{u}_{dq} = R_s \mathbf{i}_{dq} + L_d \frac{di_{dq}}{dt} + j\omega L_q \frac{di_{dq}}{dt} + jE_{sal} \tag{6.30}$$

where

$$E_{sal} = \omega\psi_{PM} - (L_d - L_q)\frac{1}{i_q} + \omega(L_d - L_q)i_d \tag{6.31}$$

E_{sal} can be called the extended back-EMF which includes the back-EMF and the terms produced by the saliency.

Equation 6.30 can be transformed into the $\alpha\beta$ reference frame.

$$\mathbf{u}_{\alpha\beta} = R_s \mathbf{i}_{\alpha\beta} + L_d \frac{di_{\alpha\beta}}{dt} - j\omega(L_d - L_q)\mathbf{i}_{\alpha\beta} + E^s_{sal-dqs} \tag{6.32}$$

where

$$E^s_{sal-dqs} = E_{sal} e^{j(\theta+\pi/2)} \tag{6.33}$$

Either a vector tracking observer or state filter (based on phase-locked loop methods) can be used to estimate the motion states from the estimated saliency-based EMF $E^s_{sal-dqs}$ without using the $arctangent$ function. The phase error between the estimated saliency-based EMF (from the previous state filter) and the saliency-based EMF model is fed into the observer controller as shown in Fig. 6.4. The observer is insensitive to mechanical parameter estimation error and torque error within the bandwidth of the observer. These errors will result in position estimation error at frequencies above the observer bandwidth [114].

This chapter utilizes the enhanced Luenberger-style back-EMF saliency tracking observer to estimate the rotor position & speed, in order to realize the closed-loop self-sensing control of IPMSM in the FCS-MPC scheme. The estimated speed value can be used as the feedback for the drive system, which can be seen in Fig. 6.7.

6.5 Simulation Results

The self-sensing FCS-MPC scheme by using a full-order Luenberger state observer is illustrated in Fig. 6.5. To check the feasibility of the proposed rotor position and speed estimation algorithms, a simulation study is carried out with reference to IPMSM-2. The parameter of IPMSM-2 is shown in Table 4.2. The conventional FCS-MPC is used as the controller and the full-order Luenberger state observer is exploited for the position & speed estimation.

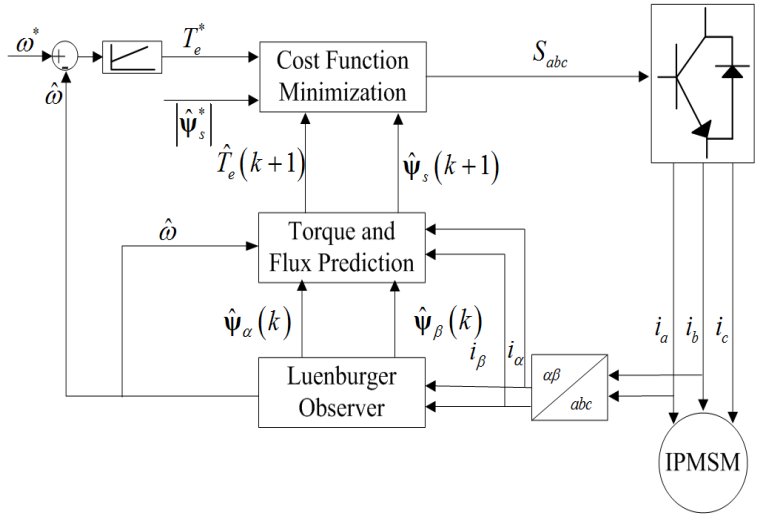

Figure 6.5: Luenberger observer-based self-sensing FCS-MPC scheme.

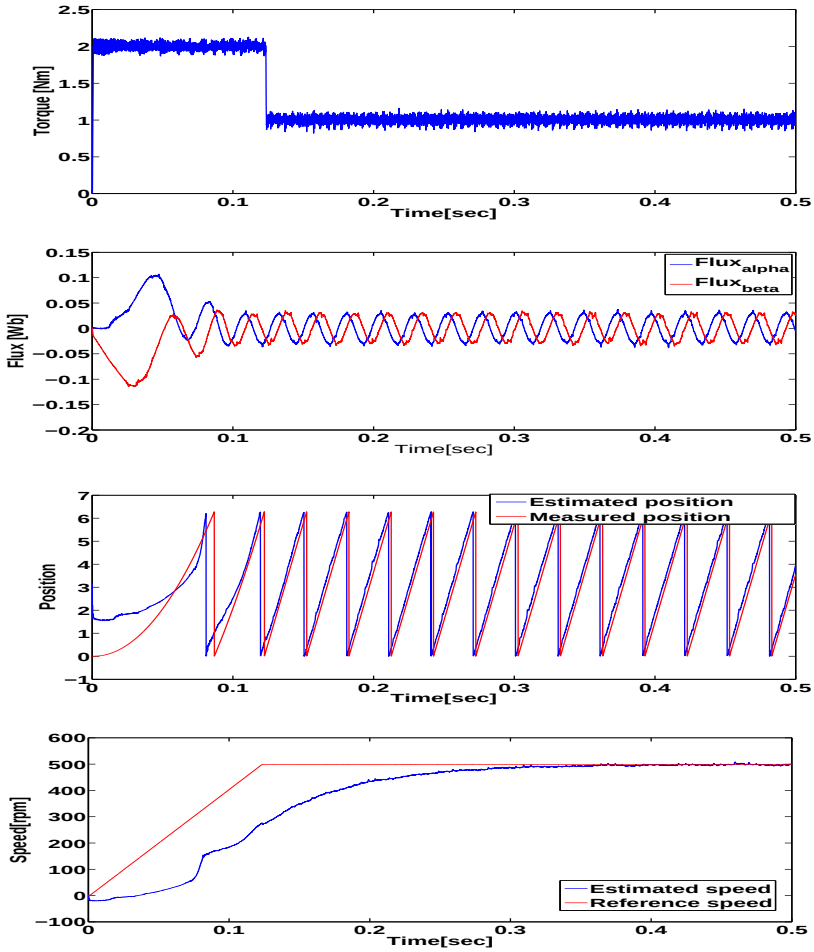

Figure 6.6: The Luenberger observe-based self-sensing FCS-MPC of IPMSM-2.

The transient-state simulation results can be seen in Fig. 6.6. With the proposed estimation algorithm, the reference speed is ramp-up from 0 to 500 rpm while the load torque is set as 1 Nm. Fig. 6.6 shows the full transient-state estimated torque, estimated flux linkage, estimated speed and estimated position. It is important to point out that the estimation speed error tends to zero after 0.3 sec.

6.6 Implementation and Experimental Results

The self-sensing model predictive torque control of IPMSMs is realized by using the saliency tracking observer to get the rotor position & speed estimations, and the conventional PI current controller of FOC is replaced by the model predictive torque control method using the flux prediction value from the Gopinath-style stator flux linkage observer. The full control scheme which avoids the use of modulator and encoder is shown in Fig. 6.7.

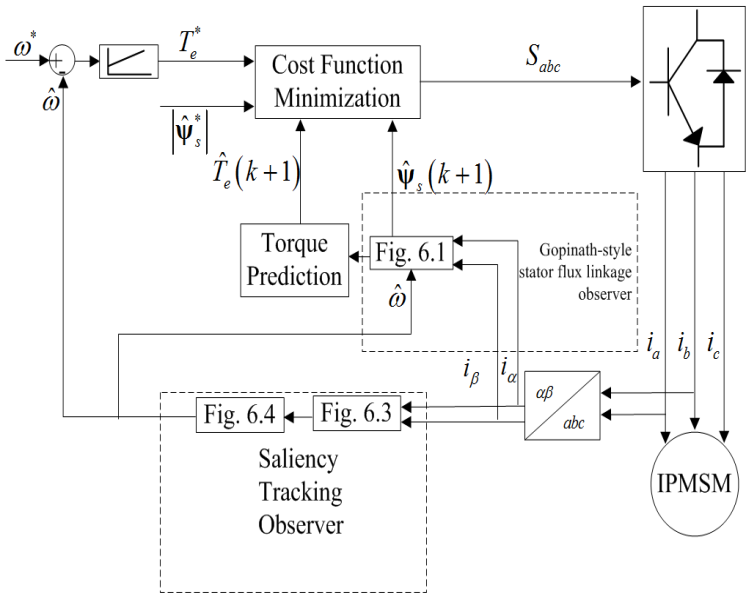

Figure 6.7: Self-sensing Model Predictive Torque Control Scheme.

The self-sensing model predictive torque control scheme was tested on the dSPACE real-time control platform. The IPMSM-2 mentioned in Chapter 4 is used to do the implementation shown in Fig. 4.10(a) and Fig. 4.10(b). Self-sensing performance of IPMSM-2 in transient-state and steady-state with different load torque is investigated.

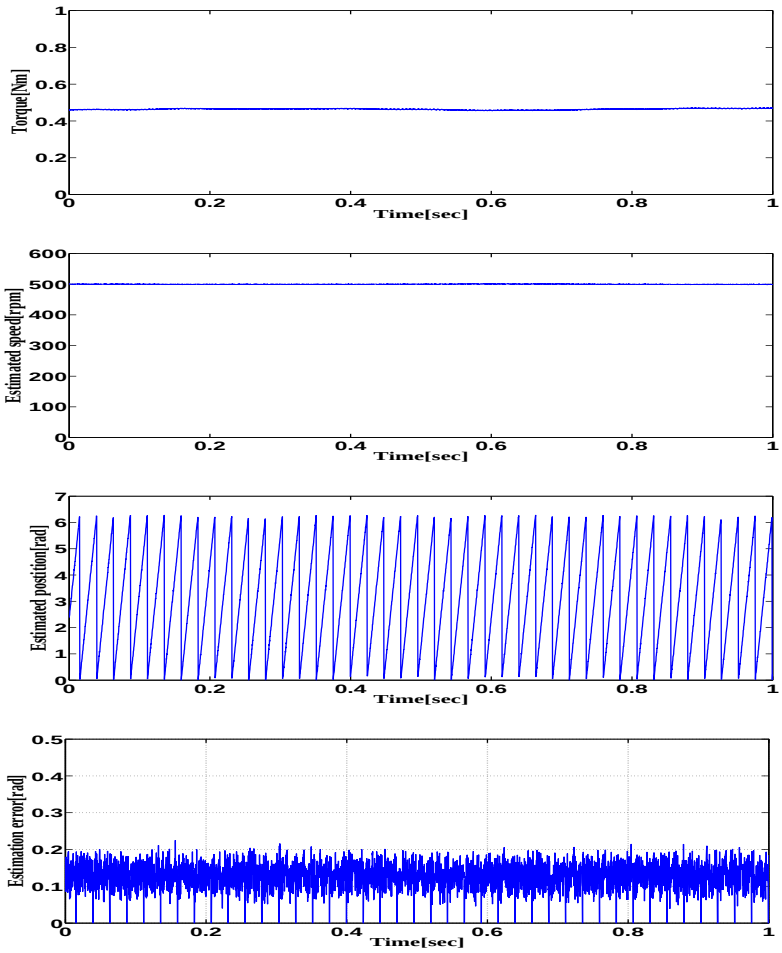

Figure 6.8: The observe-based self-sensing control of IPMSM-3 at $\omega_r = 500rpm$ under 0.5 Nm load.

The steady state experimental results of IPMSM-2 can be seen in Fig.6.8. The speed is constant as 500 rpm while the torque is constant as 0.5 Nm. Fig. 6.8 shows the full steady-state torque, estimated speed, estimated position and estimation error between the estimated position and the encoder position. The value of errors has small variability in the constant speed.

The second test is to verify the performance of self-sensing control of IPMSM-2 when a full load disturbance at the nominal speed. The torque decreases from 1 to 0 Nm while the speed is constant at 500 rpm. Fig. 6.9 shows the full transient-state torque, estimated speed, estimated position and estimation error between the estimated position and the encoder position. The value of errors has peak values

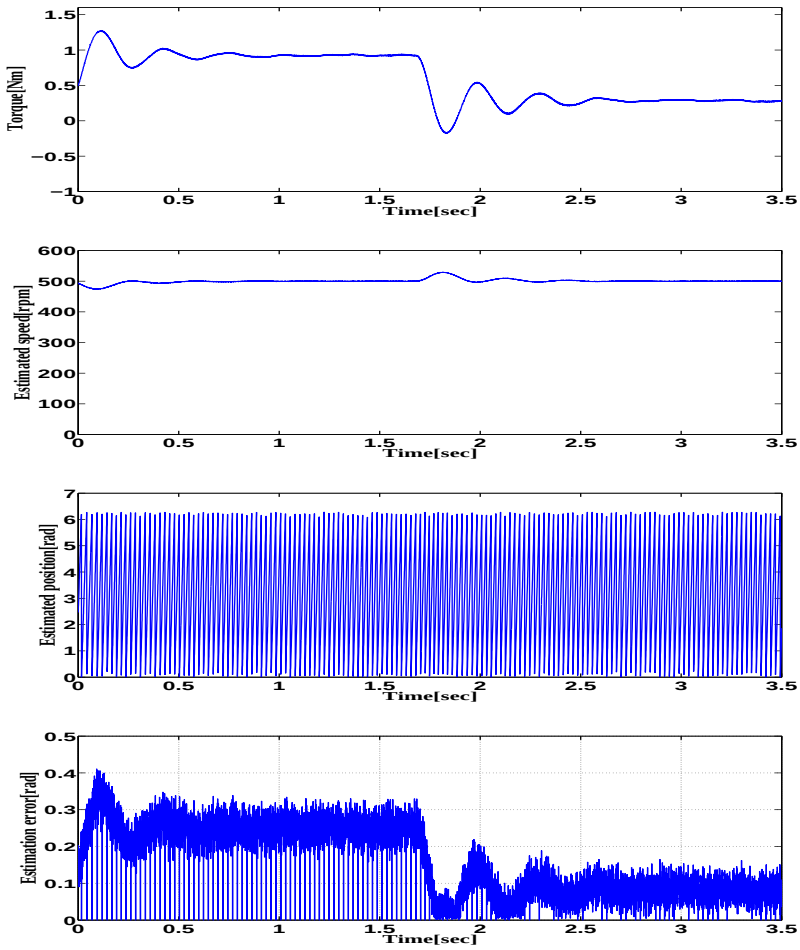

Figure 6.9: The observe-based self-sensing control of IPMSM-3 at $\omega_r = 500rpm$ under step-load.

when the load decreases from 1 to 0 Nm.

6.7 Summary

This chapter presents an improved method of estimating the rotor position using a saliency-based EMF based on the model predictive torque control scheme. A state filter is used to estimate the saliency-based EMF. In cascade, a tracking observer is used to estimate the rotor position. The tracking observer topology does not introduce phase lag to the estimated value. The flux linkage is not calculated directly

by the equations of discrete machine model in the FCS-MPC scheme, which is estimated by the Gopinath-style stator flux linkage observer. The following points summarize the work presented.

- The model predictive torque control of IPMSMs is introduced.
- The full-order Luenburger rotor position observer is explicated based on a continuous IPMSM model.
- The Gopinath-style stator flux linkage observer based on a discrete IPMSM model is used to provide estimated flux value in the FCS-MPC scheme.
- The enhanced Luenberger-style back-EMF tracking observer is implemented to estimate the rotor position and velocity.

CHAPTER 7

Conclusions and Future Work

7.1 Conclusions

Self-sensing control of PMSMs has been very popular in the industry for many years and it still has space to do performance improvements. This thesis is focus on the self-sensing control topic and demonstrate the state-of-the -art review in Chapter 2.

In Chapter 3, the mathematical model of PMSMs is introduced firstly. Secondly, the high-frequency model of the surface-mounted PMSMs is built. There are mainly two kinds of high-frequency injection methods: rotating and pulsating vector injection. Both methods are elaborated. Furthermore, the advantages and disadvantage are discussed. The implementation and experiments are done by an commercial SPMSM. The experimental results show the high frequency injection method has good estimation performance at very low & zero speed.

In chapter 4, two novel interior PMSMs are introduced and are applied to do the self-sensing control strategy. At first the machine design and the IPMSMs model are present. Secondly, the IPMSMs model with high-frequency is built. There are many effects will decrease the estimation accuracy: saliency, cross Saturation, high frequency inductance, high frequency resistance and harmonic distortion. All the possible reasons based on the two novel IPMSMs are analyzed in this chapter. The implementation and experiments are done by using the conventional high frequency rotating vector injection method. It proved that the novel IPMSMs have very high estimation accuracy.

In chapter 5, the new stator topology of IPMSM-2 is demonstrated. Firstly, losses in this IPMSM-2 resulting from high frequency injection for self-sensing control is analyzed by MMF calculated. Secondly, the high frequency losses are analyzed

by the currents harmonics from the experimental results of injection-based self-sensing control of IPMSM-2. Finally, the new high frequency losses analytical method based on Poynting's theorem is proposed in this chapter. It will take a short computational time to calculate the HF losses by the analytical method.

In chapter 6, the self-sensing control of PMSMs is implemented using the back-EMF at medium and high speed. Firstly, the conventional model predictive torque control method is introduced, which is an alternative control method from FOC and DTC. Secondly, the Gopinath-style stator flux linkage observer is applied to do the flux estimation in the model predictive torque control scheme. Thirdly, the full-order Luenberger rotor position observer is built and the simulation results can be seen in this chapter. The enhanced Luenberger-style saliency tracking rotor position observer is achieved by calculating the back-EMF. Finally, the implementation and experiments are done based on the conventional model predictive torque control method, and the Gopinath-style stator flux linkage observer is realized to do the flux estimation, and the enhanced Luenberger-style saliency tracking rotor position observer is completed the self-sensing control.

The conclusion and the recommended future work is shown in this chapter 7.

7.2 Recommended Future Work

Based on the work presented, the following topics have been identified for further investigation:

- Integration of the saliency-based high frequency injection self-sensing method into the low switching frequency MPC with continuous control set.

Since MPC with continuous control set achieves desired torque and stator flux with constant switching frequency, the high frequency injection-based self-sensing method can be integrated into MPC with continuous control set. For high switching frequency operation, the frequency of injected voltage has a wide range of options. In contrast, for low switching frequency operation, the frequency of the injected sinusoidal voltage needs to be set low to ensure enough points for one cycle of the injected sinusoidal voltage. However, a torque pulsation will be introduced when the injected voltage has the frequency compatible to the fundamental frequency. Thus, the PWM switching frequency signal injection based self-sensing method should be integrated to the low switching frequency MPC to achieve desired torque and flux without position sensor. The performance of the low switching frequency, self-sensing, MPC with continuous control set needs to be investigated for both normal and deep field weakening operation with low switching frequencies.

- Evaluation of the power losses generated from different high frequency injection methods.

In this thesis, the calculation of losses from high frequency injection effects is proposed by a new analytical method, however, in order to get the accurate results more research need to do. Saliency-based self-sensing method can be implemented based on either rotating or pulsating high frequency voltage injection. Lots of papers have been published on comparison of different injection methods in terms of the position estimation accuracy. However, the power losses from different high frequency injection methods have not been discussed or investigated. Since dynamic loss modeling has the capability of capturing the dynamic loss generated from the high frequency voltage injection in self-sensing methods, it should be utilized to evaluate the performance of different injection methods, such as sinusoidal wave injection and square wave injection, in terms of power losses.

- Investigation of different flux observers can be used in the conventional model predictive torque control method.

Flux observer is the key point of the electric drives and not very popular used in the FCS-MPC scheme. This thesis proposes a Gopinath-Style observer for the flux estimation in IPMSM under both steady state and transient operations. It would be better if this observer be changed to such as sliding mode observers, or Kalman filters, in order to find a optimization solution of the most accurate flux estimation.

- Investigation of excess loss and rotor loss based on FEM for different classes of electrical machines.

In this thesis, the stator iron losses, rotor iron losses and the magnet eddy current losses of IPMSM-2 based on FEM is shown. However, the excess loss and the rotor loss due to the leakage flux are not taken into account. The experimentally estimated iron loss coefficients can partially cover the excess loss and rotor loss. However, the detailed investigation of these losses has not been performed. FEM could be a good method to investigate the both losses for different machines.

APPENDIX A

List of Nomenclature and Abbreviations

A.1 Nomenclature

The following list only contains relevant symbols and bold symbol means space vector.

$\boldsymbol{i}, \boldsymbol{I}$	current space vector
$\boldsymbol{u}$	voltage space vector
$\boldsymbol{\Psi}$	flux linkage space vector
R	resistance
$\boldsymbol{L}$	inductance
θ	rotor position angle
δ	current load angle
ω	speed
N	number of turns per coil
P	pole pair number or power
$\boldsymbol{\Theta}$	magnetomotive force
J	induced current density
A	magnetic vector potential
B	flux density
r, R	radial length
T_e	electromagnetic torque
T_L	load torque
T_s	sample period

The following list only contains relevant subscripts.

$\hat{}$	estimated quantity
$\dot{}$	time derivative operator d/dt
*	reference quantity
s	stator
r	rotor
c	carrier (injection) signals
α, β	stator fixed Cartesian axis
d, q	rotor fixed direct and quadrature axis
Σ, Δ	mean and difference value
p, n	positive and negative direction
$w1, w2$	winding system 1 and 2 of IPMSM-3
pm, mag	permanent-magnet
$eddy$	eddy-current
$hyst$	hysteresis

A.2 Abbreviations

PMSMs	Permanent magnet synchronous machines
SPMSMs	Surface-mounted permanent magnet synchronous machines
IPMSMs	Interior permanent magnet synchronous machines
CW	Concentrated windings
DW	Distributed windings
HF	High frequency
FEM	Finite element methods
MMF	Magnetomotive force
FFT	Fast Fourier transform
FS	Fractional slot
CFF	Command feed-forward
EMF	Electromotive Force
MRAS	Model reference adaptive system
PWM	Pulse width modulation
SVM	Space vector modulation
FLC	Fuzzy logic control
DTC	Direct torque control
FOC	Field-Oriented Control
DB-DTFC	Deadbeat-direct torque and flux control
PID	Proportional-integral-derivative
LMC	Loss model control
FCS-MPC	Model predictive control with finite control set

APPENDIX B

List of Publications

B.1 Published Conference Papers

- Xiaocan Wang, R. Kennel, Zhixun Ma and Jianbo Gao, ”Analysis of permanent-magnet machine for sensorless control based on high-frequency signal injection,” Power Electronics and Motion Control Conference (IPEMC), 2012 7th International , vol.4, pp.2367,2371, 2-5 June 2012.

- Xiaocan Wang, Wei Xie, R. Kennel and D. Gerling, ”Sensorless control of a novel IPMSM based on high-frequency injection,” Power Electronics and Applications (EPE), 2013 15th European Conference on , pp.1,8, 2-6 Sept. 2013.

- Wei Xie, Xiaocan Wang, G. Dajaku, D. Gerling and R. Kennel, ”Improvement and comparison of efficiency and low cost drive system based on DTC and DTC-SVM,” Electric Machines & Drives Conference (IEMDC), 2013 IEEE International , pp.1261,1266, 12-15 May 2013.

- Wei Xie, Fengxiang Wang, Xiaocan Wang, G. Dajaku, D. Gerling and R. Kennel, ”Analysis of high efficiency and low cost drive system of IPMSM by using two-steps model predictive torque control,” Control Conference (CCC), 2013 32nd Chinese, pp.4114,4119, 26-28 July 2013.

- Wei Xie, Xiaocan Wang, G. Dajaku, D. Gerling and R. Kennel, ”Analysis and improvement of high efficiency and low cost drive system based on direct torque control,” Power Electronics and Applications (EPE), 2013 15th European Conference on, pp.1,10, 2-6 Sept. 2013.

- Xiaocan Wang, R. Kennel, Wei Xie and D. Gerling, ”Analysis of losses in a novel IPMSM resulting from high-frequency injection for sensorless control,”

Sensorless Control for Electrical Drives and Predictive Control of Electrical Drives and Power Electronics (SLED/PRECEDE), 2013 IEEE International Symposium on, pp.1,5, 17-19 Oct. 2013.

B.2 Published Journal Papers

- Xiaocan Wang, Wei Xie, G. Dajaku, R. Kennel, D. Gerling and R. D. Lorenz, ”Position Self-Sensing Evaluation of Novel CW-IPMSMs with a HF Injection Method,” Industry Applications, IEEE Transactions on , vol.50, no.5, pp.3325,3334, Sept.-Oct. 2014

B.3 Submitted Journal Papers

- Wei Xie, Xiaocan Wang, Fengxiang Wang, D. Gerling and R. Kennel, ”Dynamic Loss Minimization of Finite Control Set Model Predictive Torque Control for Electric Drive System,” IEEE Transactions on Power Electronics.
- Wei Xie, Xiaocan Wang, Fengxiang Wang, Wei Xu, D. Gerling, R. Kennel and R. D. Lorenz,, ”Deadbeat Model Predictive Torque Control for Permanent Magnet Synchronous Machines,” IEEE Transactions on Industrial Electronics.

Bibliography

[1] D. Novotny, T. Lipo, and T.M.Jahns, *Introduction to electric machines and Drives*. WisPERC Administrator, 2009.

[2] P. Guglielmi, M. Pastorelli, G. Pellegrino, and A. Vagati, "Position-sensorless control of permanent-magnet-assisted synchronous reluctance motor," *Industry Applications, IEEE Transactions on*, vol. 40, no. 2, pp. 615–622, 2004.

[3] D. Novotny and T. Lipo, *Vector Control and Dynamics of AC Drives*. New York: Oxford Univ, 1996.

[4] A. Faggion, E. Fornasiero, N. Bianchi, and S. Bolognani, "Sensorless capability of fractional-slot surface-mounted PM motors," *Industry Applications, IEEE Transactions on*, vol. 49, no. 3, pp. 1325–1332, 2013.

[5] C.-Y. Yu, J. Tamura, D. Reigosa, and R. Lorenz, "Position self-sensing evaluation of a FI-IPMSM based on high-frequency signal injection methods," *Industry Applications, IEEE Transactions on*, vol. 49, no. 2, pp. 880–888, 2013.

[6] L. A. S. Ribeiro, M. Degner, F. Briz, and R. Lorenz, "Comparison of carrier signal voltage and current injection for the estimation of flux angle or rotor position," in *Industry Applications Conference, 1998. Thirty-Third IAS Annual Meeting. The 1998 IEEE*, vol. 1, 1998, pp. 452–459.

[7] M. Linke, R. Kennel, and J. Holtz, "Sensorless speed and position control of synchronous machines using alternating carrier injection," in *Electric Machines and Drives Conference, 2003. IEMDC'03. IEEE International*, vol. 2, 2003, pp. 1211–1217 vol.2.

[8] R. Wu and G. Slemon, "A permanent magnet motor drive without a shaft sensor," in *Industry Applications Society Annual Meeting*, vol. 1, 1990, pp. 553–558.

[9] E. Robeischl, M. Schroedl, and M. Krammer, "Position-sensorless biaxial position control with industrial PM motor drives based on INFORM- and back EMF model," in *IECON 02 Industrial Electronics Society, IEEE 2002 28th Annual Conference of the*, vol. 1, 2002, pp. 668–673.

[10] A. Eilenberger and M. Schroedl, "Extended back EMF model for PM synchronous machines with different inductances in d- and q-axis," in *Power Electronics and Motion Control Conference, 2008. EPE-PEMC 2008. 13th*, 2008, pp. 945–948.

[11] Freescale, "Sensorless PMSM Vector Control with a Sliding Mode Observer for Compressors Using MC56F8013," Freescale Semiconductor, Tech. Rep., 09/2008.

[12] M. Corley and R. Lorenz, "Rotor position and velocity estimation for a salient-pole permanent magnet synchronous machine at standstill and high speeds," *Industry Applications, IEEE Transactions on*, vol. 34, no. 4, pp. 784–789, 1998.

[13] R. Kennel, "Encoderless control of synchronous machines with permanent magnets - impact of magnetic design," in *Optimization of Electrical and Electronic Equipment (OPTIM), 2010 12th International Conference on*, 2010, pp. 19–24.

[14] F. Briz, M. Degner, A. Diez, and R. Lorenz, "Measuring, modeling, and decoupling of saturation-induced saliencies in carrier-signal injection-based sensorless ac drives," *Industry Applications, IEEE Transactions on*, vol. 37, no. 5, pp. 1356–1364, 2001.

[15] ——, "Static and dynamic behavior of saturation-induced saliencies and their effect on carrier-signal-based sensorless AC drives," *Industry Applications, IEEE Transactions on*, vol. 38, no. 3, pp. 670–678, 2002.

[16] P. Garcia, F. Briz, M. Degner, and D. Diaz-Reigosa, "Accuracy, bandwidth, and stability limits of carrier-signal-injection-based sensorless control methods," *Industry Applications, IEEE Transactions on*, vol. 43, no. 4, pp. 990–1000, 2007.

[17] Z. Zhu, Y. Li, D. Howe, and C. Bingham, "Compensation for rotor position estimation error due to cross-coupling magnetic saturation in signal injection based sensorless control of PM brushless AC motors," in *Electric Machines Drives Conference, 2007. IEMDC '07. IEEE International*, vol. 1, 2007, pp. 208–213.

[18] M. Zeraoulia, M. Benbouzid, and D. Diallo, "Electric motor drive selection issues for HEV propulsion systems: A comparative study," *Vehicular Technology, IEEE Transactions on*, vol. 55, no. 6, pp. 1756–1764, 2006.

[19] Control of permanent magnet synchronous motors for automotive applications. [Online]. Available: http://wwwlea.uni-paderborn.de/forschung/pmsm-control.html

[20] G. Dajaku, "Electromagnetic and thermal modeling of highly utilized PM machines," Ph.D. dissertation, University of Federal Defense Munich, 2006.

[21] Optimising new motor designs for electric vehicle. [Online]. Available: http://www.dpaonthenet.net/article/62178

[22] D. Ishak, Z. Zhu, and D. Howe, "Comparison of PM brushless motors, having either all teeth or alternate teeth wound," *Energy Conversion, IEEE Transactions on*, vol. 21, no. 1, pp. 95–103, 2006.

[23] N. Bianchi and E. Fornasiero, "Index of rotor losses in three-phase fractional-slot permanent magnet machines," *Electric Power Applications, IET*, vol. 3, no. 5, pp. 381–388, 2009.

[24] G. Dajaku and D. Gerling, "Magnetic radial force density of the PM machine with 12-teeth/10-poles winding topology," in *Electric Machines and Drives Conference, 2009. IEMDC '09. IEEE International*, 2009, pp. 1715–1720.

[25] ——, "Eddy current loss minimization in rotor magnets of PM machines using high-efficiency 12-teeth/10-slots winding topology," in *Electrical Machines and Systems (ICEMS), 2011 International Conference on*, 2011, pp. 1–6.

[26] ——, "A novel 24-slots/10-poles winding topology for electric machines," in *Electric Machines Drives Conference (IEMDC), 2011 IEEE International*, 2011, pp. 65–70.

[27] ——, “A novel 12-teeth/10-poles PM machine with flux barriers in stator yoke,” in *Electrical Machines (ICEM), 2012 XXth International Conference on*, 2012, pp. 36–40.

[28] E. Fornasiero, L. Alberti, N. Bianchi, and S. Bolognani, “Considerations on selecting fractional-slot nonoverlapped coil windings,” *Industry Applications, IEEE Transactions on*, vol. 49, no. 3, pp. 1316–1324, 2013.

[29] G. Dajaku, “Elektrische maschine,” Patent DE 102 008 054 284 A1.

[30] G. Dajaku and D. Gerling, “A novel tooth concentrated winding with low space harmonic contents,” in *Electric Machines Drives Conference (IEMDC), 2013 IEEE International*, 2013, pp. 755–760.

[31] L. Xu and S. Li, “Torque control patching and anti-windup and bumpless transfer conditioning of current regulators for high-speed PMSM systems,” in *Power Electronics Specialists Conference, 2001. PESC. 2001 IEEE 32nd Annual*, vol. 3, 2001, pp. 1679–1682 vol. 3.

[32] J. Holtz, W. Lotzkat, and A. Khambadkone, “On continuous control of PWM inverters in the overmodulation range including the six-step mode,” *Power Electronics, IEEE Transactions on*, vol. 8, no. 4, pp. 546–553, 1993.

[33] J. Jung and K. Nam, “A dynamic decoupling control scheme for high-speed operation of induction motors,” *Industrial Electronics, IEEE Transactions on*, vol. 46, no. 1, pp. 100–110, 1999.

[34] I. Takahashi and T. Noguchi, “A new quick-response and high-efficiency control strategy of an induction motor,” *Industry Applications, IEEE Transactions on*, vol. IA-22, no. 5, pp. 820–827, 1986.

[35] I. Takahashi and Y. Ohmori, “High-performance direct torque control of an induction motor,” *Industry Applications, IEEE Transactions on*, vol. 25, no. 2, pp. 257–264, 1989.

[36] J. S. Lee, C.-H. Choi, J.-K. Seok, and R. Lorenz, “Deadbeat-direct torque and flux control of interior permanent magnet synchronous machines with discrete time stator current and stator flux linkage observer,” *Industry Applications, IEEE Transactions on*, vol. 47, no. 4, pp. 1749–1758, 2011.

[37] T. Habetler, F. Profumo, M. Pastorelli, and L. Tolbert, “Direct torque control of induction machines using space vector modulation,” *Industry Applications, IEEE Transactions on*, vol. 28, no. 5, pp. 1045–1053, 1992.

[38] G. Escobar, A. Stankovic, E. Galvan, J. Carrasco, and R. Ortega, "A family of switching control strategies for the reduction of torque ripple in DTC," *Control Systems Technology, IEEE Transactions on*, vol. 11, no. 6, pp. 933–939, 2003.

[39] L. Zhong, M. Rahman, W. Y. Hu, and K. W. Lim, "Analysis of direct torque control in permanent magnet synchronous motor drives," *Power Electronics, IEEE Transactions on*, vol. 12, no. 3, pp. 528–536, 1997.

[40] H. Ziane, J.-M. Retif, and T. Rekioua, "Fixed-switching-frequency DTC control for PM synchronous machine with minimum torque ripples," *Electrical and Computer Engineering, Canadian Journal of*, vol. 33, no. 3/4, pp. 183–189, 2008.

[41] R. Lorenz, "The emerging role of dead-beat, direct torque and flux control in the future of induction machine drives," in *Optimization of Electrical and Electronic Equipment, 2008. OPTIM 2008. 11th International Conference on*, 2008, pp. XIX–XXVII.

[42] D. Reigosa, P. Garcia, D. Raca, F. Briz, and R. Lorenz, "Measurement and adaptive decoupling of cross-saturation effects and secondary saliencies in sensorless controlled IPM synchronous machines," *Industry Applications, IEEE Transactions on*, vol. 44, no. 6, pp. 1758–1767, 2008.

[43] J. Urresty, J. Riba, and L. Romeral, "A back-EMF based method to detect magnet failures in PMSMs," *Magnetics, IEEE Transactions on*, vol. 49, no. 1, pp. 591–598, 2013.

[44] Z. Wang, K. Lu, and F. Blaabjerg, "A simple startup strategy based on current regulation for back-EMF-based sensorless control of PMSM, year=2012, volume=27, number=8, pages=3817-3825, keywords=closed loop systems;electric current control;electric potential;permanent magnet machines;sensorless machine control;synchronous machines;closed-loop current regulation;control simplicity;general design guideline;high machine efficiency;industrial applications;interior PMSM;load conditions;low-cost solution;motor parameter variation;permanent magnet synchronous machines;position estimation;simple startup strategy;simple-structure back-EMF-based sensorless controller;starting method;surface-mounted PMSM;Acceleration;Permanent magnet motors;Rotors;Sensorless control;Switches;Synchronous motors;Torque;Back-EMF;current regulation;permanent magnet synchronous machine (PMSM);sensorless con-

trol;startup strategy, doi=10.1109/TPEL.2012.2186464, issn=0885-8993,," *Power Electronics, IEEE Transactions on*.

[45] K. Lu, X. Lei, and F. Blaabjerg, "Artificial inductance concept to compensate nonlinear inductance effects in the back EMF-based sensorless control method for PMSM," *Energy Conversion, IEEE Transactions on*, vol. 28, no. 3, pp. 593–600, 2013.

[46] R. Hejny and R. Lorenz, "Evaluating the practical low-speed limits for back-EMF tracking-based sensorless speed control using drive stiffness as a key metric," *Industry Applications, IEEE Transactions on*, vol. 47, no. 3, pp. 1337–1343, 2011.

[47] Y. Inoue, Y. Kawaguchi, S. Morimoto, and M. Sanada, "Performance improvement of sensorless IPMSM drives in a low-speed region using online parameter identification," *Industry Applications, IEEE Transactions on*, vol. 47, no. 2, pp. 798–804, 2011.

[48] S. Ichikawa, M. Tomita, S. Doki, and S. Okuma, "Sensorless control of permanent-magnet synchronous motors using online parameter identification based on system identification theory," *Industrial Electronics, IEEE Transactions on*, vol. 53, no. 2, pp. 363–372, 2006.

[49] ——, "Sensorless control of synchronous reluctance motors based on extended EMF models considering magnetic saturation with online parameter identification," *Industry Applications, IEEE Transactions on*, vol. 42, no. 5, pp. 1264–1274, 2006.

[50] S. Bolognani, L. Tubiana, and M. Zigliotto, "Extended kalman filter tuning in sensorless PMSM drives," *Industry Applications, IEEE Transactions on*, vol. 39, no. 6, pp. 1741–1747, 2003.

[51] S. Bolognani, M. Zigliotto, and M. Zordan, "Extended-range PMSM sensorless speed drive based on stochastic filtering," *Power Electronics, IEEE Transactions on*, vol. 16, no. 1, pp. 110–117, 2001.

[52] T.-F. Chan, P. Borsje, and W. Wang, "Application of unscented kalman filter to sensorless permanent-magnet synchronous motor drive," in *Electric Machines and Drives Conference, 2009. IEMDC '09. IEEE International*, 2009, pp. 631–638.

[53] J.-S. Jang, B.-G. Park, T.-S. Kim, D. M. Lee, and D.-S. Hyun, "Parallel reduced-order extended kalman filter for PMSM sensorless drives," in *Industrial Electronics, 2008. IECON 2008. 34th Annual Conference of IEEE*, 2008, pp. 1326–1331.

[54] G. Foo and M. Rahman, "Sensorless direct torque and flux-controlled IPM synchronous motor drive at very low speed without signal injection," *Industrial Electronics, IEEE Transactions on*, vol. 57, no. 1, pp. 395–403, 2010.

[55] J. Lee, J. Hong, K. Nam, R. Ortega, L. Praly, and A. Astolfi, "Sensorless control of surface-mount permanent-magnet synchronous motors based on a nonlinear observer," *Power Electronics, IEEE Transactions on*, vol. 25, no. 2, pp. 290–297, 2010.

[56] G. Foo and M. Rahman, "Direct torque control of an IPM-synchronous motor drive at very low speed using a sliding-mode stator flux observer," *Power Electronics, IEEE Transactions on*, vol. 25, no. 4, pp. 933–942, 2010.

[57] A. Yoo and S.-K. Sul, "Design of flux observer robust to interior permanent-magnet synchronous motor flux variation," *Industry Applications, IEEE Transactions on*, vol. 45, no. 5, pp. 1670–1677, 2009.

[58] P. Jansen and R. Lorenz, "A physically insightful approach to the design and accuracy assessment of flux observers for field oriented induction machine drives," *Industry Applications, IEEE Transactions on*, vol. 30, no. 1, pp. 101–110, 1994.

[59] J. Kim and S.-K. Sul, "New stand-still position detection strategy for PMSM drive without rotational transducers," in *Applied Power Electronics Conference and Exposition, 1994. APEC '94. Conference Proceedings 1994., Ninth Annual*, 1994, pp. 363–369 vol.1.

[60] S. Ostlund and M. Brokemper, "Initial rotor position detections for an integrated PM synchronous motor drive," in *Industry Applications Conference, 1995. Thirtieth IAS Annual Meeting, IAS '95., Conference Record of the 1995 IEEE*, vol. 1, 1995, pp. 741–747 vol.1.

[61] D.-W. Chung, J.-K. Kang, and S.-K. Sul, "Initial rotor position detection of PMSM at standstill without rotational transducer," in *Electric Machines and Drives, 1999. International Conference IEMD '99*, 1999, pp. 785–787.

[62] P. Jansen and R. Lorenz, "Transducerless position and velocity estimation in induction and salient AC machines," *Industry Applications, IEEE Transactions on*, vol. 31, no. 2, pp. 240–247, 1995.

[63] M. Degner and R. Lorenz, "Using multiple saliencies for the estimation of flux, position, and velocity in AC machines," in *Industry Applications Conference, 1997. Thirty-Second IAS Annual Meeting, IAS '97., Conference Record of the 1997 IEEE*, vol. 1, 1997, pp. 760–767 vol.1.

[64] F. Briz, A. Diez, and M. Degner, "Dynamic operation of carrier-signal-injection-based sensorless direct field-oriented AC drives," *Industry Applications, IEEE Transactions on*, vol. 36, no. 5, pp. 1360–1368, 2000.

[65] A. Consoli, G. Scarcella, and A. Testa, "Industry application of zero-speed sensorless control techniques for PM synchronous motors," *Industry Applications, IEEE Transactions on*, vol. 37, no. 2, pp. 513–521, 2001.

[66] F. Briz, M. Degner, P. Garcia, and J. Guerrero, "Rotor position estimation of AC machines using the zero-sequence carrier-signal voltage," *Industry Applications, IEEE Transactions on*, vol. 41, no. 6, pp. 1637–1646, 2005.

[67] C. Wang and L. Xu, "A novel approach for sensorless control of PM machines down to zero speed without signal injection or special PWM technique," *Power Electronics, IEEE Transactions on*, vol. 19, no. 6, pp. 1601–1607, 2004.

[68] H. Kim, M. Harke, and R. Lorenz, "Sensorless control of interior permanent-magnet machine drives with zero-phase lag position estimation," *Industry Applications, IEEE Transactions on*, vol. 39, no. 6, pp. 1726–1733, 2003.

[69] J.-I. Ha and S.-K. Sul, "Sensorless field-orientation control of an induction machine by high-frequency signal injection," *Industry Applications, IEEE Transactions on*, vol. 35, no. 1, pp. 45–51, 1999.

[70] J.-I. Ha, K. Ide, T. Sawa, and S.-K. Sul, "Sensorless rotor position estimation of an interior permanent-magnet motor from initial states," *Industry Applications, IEEE Transactions on*, vol. 39, no. 3, pp. 761–767, 2003.

[71] J. Guerrero, M. Leetmaa, F. Briz, A. Zamarron, and R. Lorenz, "Inverter nonlinearity effects in high-frequency signal-injection-based sensorless control methods," *Industry Applications, IEEE Transactions on*, vol. 41, no. 2, pp. 618–626, 2005.

[72] C.-H. Choi and J.-K. Seok, "Compensation of zero-current clamping effects in high-frequency-signal-injection-based sensorless pm motor drives," *Industry Applications, IEEE Transactions on*, vol. 43, no. 5, pp. 1258–1265, 2007.

[73] W. Hammel and R. Kennel, "Integration of alternating carrier injection in position sensorless control without any filtering," in *Energy Conversion Congress and Exposition, 2009. ECCE 2009. IEEE*, 2009, pp. 3830–3836.

[74] C.-H. Choi and J.-K. Seok, "Pulsating signal injection-based axis switching sensorless control of surface-mounted permanent-magnet motors for minimal zero-current clamping effects," *Industry Applications, IEEE Transactions on*, vol. 44, no. 6, pp. 1741–1748, 2008.

[75] Y. Yoon and S. Sul, "Sensorless control for induction machines based on square-wave voltage injection," *Power Electronics, IEEE Transactions on*, vol. PP, no. 99, pp. 1–1, 2013.

[76] Y.-D. Yoon, S.-K. Sul, S. Morimoto, and K. Ide, "High-bandwidth sensorless algorithm for ac machines based on square-wave-type voltage injection," *Industry Applications, IEEE Transactions on*, vol. 47, no. 3, pp. 1361–1370, 2011.

[77] A. Linder, R. Kanchan, R. Kennel, and P. Stolze, *Model-Based Predictive Control of Electric Drives*. Cuvillier Verlag Göttingen, Munich, Germany, 2010.

[78] R. Kennel and D. Schöder, "A predictive control strategy for converters," in *IFAC Control Power Electron. Elect. Drives*, 1983, pp. 415–422.

[79] P. Cortes, M. Kazmierkowski, R. Kennel, D. Quevedo, and J. Rodriguez, "Predictive control in power electronics and drives," *Industrial Electronics, IEEE Transactions on*, vol. 55, no. 12, pp. 4312–4324, 2008.

[80] E. F. Camacho and C. Bordons, *Model Predictive Control*. NewYork:Springer-Verlag, 1999.

[81] J. M. Maciejowski, *Predictive Control With Constraints*. Englewood Cliffs, NJ: Prentice-Hall, 2002.

[82] A. Linder and R. Kennel, "Model predictive control for electrical drives," in *Power Electronics Specialists Conference, 2005. PESC '05. IEEE 36th*, 2005, pp. 1793–1799.

[83] H. Miranda, P. Cortes, J. Yuz, and J. Rodriguez, "Predictive torque control of induction machines based on state-space models," *Industrial Electronics, IEEE Transactions on*, vol. 56, no. 6, pp. 1916–1924, 2009.

[84] P. Cortes, G. Ortiz, J. Yuz, J. Rodriguez, S. Vazquez, and L. Franquelo, "Model predictive control of an inverter with output LC filter for UPS applications," *Industrial Electronics, IEEE Transactions on*, vol. 56, no. 6, pp. 1875 –1883, june 2009.

[85] P. Cortes ands, A. Wilson, S. Kouro, J. Rodriguez, and H. Abu-Rub, "Model predictive control of multilevel cascaded H-bridge inverters," *Industrial Electronics, IEEE Transactions on*, vol. 57, no. 8, pp. 2691 –2699, aug. 2010.

[86] H. Huang, E. Fuchs, and J. White, "Optimization of single-phase induction motor design. II. the maximum efficiency and minimum cost of an optimal design," *Energy Conversion, IEEE Transactions on*, vol. 3, no. 2, pp. 357–366, 1988.

[87] M. Benbouzid and N. Nait Said, "An efficiency-optimization controller for induction motor drives," *Power Engineering Review, IEEE*, vol. 18, no. 5, pp. 63–64, 1998.

[88] C. Liu, K. Chau, W. Li, and C. Yu, "Efficiency optimization of a permanent-magnet hybrid brushless machine using dc field current control," *Magnetics, IEEE Transactions on*, vol. 45, no. 10, pp. 4652–4655, 2009.

[89] H. Rehman and L. Xu, "Alternative energy vehicles drive system: Control, flux and torque estimation, and efficiency optimization," *Vehicular Technology, IEEE Transactions on*, vol. 60, no. 8, pp. 3625–3634, 2011.

[90] M. Hajian, J. Soltani, G. Markadeh, and S. Hosseinnia, "Adaptive nonlinear direct torque control of sensorless IM drives with efficiency optimization," *Industrial Electronics, IEEE Transactions on*, vol. 57, no. 3, pp. 975–985, 2010.

[91] A. Taheri, A. Rahmati, and S. Kaboli, "Efficiency improvement in DTC of six-phase induction machine by adaptive gradient descent of flux," *Power Electronics, IEEE Transactions on*, vol. 27, no. 3, pp. 1552–1562, 2012.

[92] W. Xie, F. Wang, X. Wang, G. Dajaku, D. Gerling, and R. Kennel, "Analysis of high efficiency and low cost drive system of ipmsm by using two-steps model predictive torque control," in *Control Conference (CCC), 2013 32nd Chinese*, 2013, pp. 4114–4119.

[93] S. Morimoto, Y. Tong, Y. Takeda, and T. Hirasa, "Loss minimization control of permanent magnet synchronous motor drives," *Industrial Electronics, IEEE Transactions on*, vol. 41, no. 5, pp. 511–517, 1994.

[94] H. Kouns, J.-S. Lai, and C. Konrad, "Analysis of a traction induction motor drive operating under maximum efficiency and maximum torque per ampere conditions," in *Applied Power Electronics Conference and Exposition, 2004. APEC '04. Nineteenth Annual IEEE*, vol. 1, 2004, pp. 545–551 Vol.1.

[95] C. Cavallaro, A. Di Tommaso, R. Miceli, A. Raciti, G. Galluzzo, and M. Trapanese, "Efficiency enhancement of permanent-magnet synchronous motor drives by online loss minimization approaches," *Industrial Electronics, IEEE Transactions on*, vol. 52, no. 4, pp. 1153–1160, 2005.

[96] C. Mi, G. Slemon, and R. Bonert, "Modeling of iron losses of surface-mounted permanent magnet synchronous motors," in *Industry Applications Conference, 2001. Thirty-Sixth IAS Annual Meeting. Conference Record of the 2001 IEEE*, vol. 4, 2001, pp. 2585–2591 vol.4.

[97] ——, "Modeling of iron losses of permanent-magnet synchronous motors," *Industry Applications, IEEE Transactions on*, vol. 39, no. 3, pp. 734–742, 2003.

[98] X. Wang, R. Kennel, Z. Ma, and J. Gao, "Analysis of permanent-magnet machine for sensorless control based on high-frequency signal injection," in *Power Electronics and Motion Control Conference (IPEMC), 2012 7th International*, vol. 4, June 2012, pp. 2367–2371.

[99] A. A. N. N. A.-S. Ameen and R. Kennel, "Design of a digital system dedicated for electrical drive applications," *EPE Journal*, vol. 20, no. 4, pp. 37–44, 2010.

[100] X. Wang, W. Xie, R. Kennel, and D. Gerling, "Sensorless control of a novel IPMSM based on high-frequency injection," in *Power Electronics and Applications (EPE), 2013 15th European Conference on*, 2013, pp. 1–8.

[101] W. Xie, X. Wang, G. Dajaku, D. Gerling, and R. Kennel, "Improvement and comparison of efficiency and low cost drive system based on DTC and DTC-SVM," in *Electric Machines Drives Conference (IEMDC), 2013 IEEE International*, May 2013, pp. 1261–1266.

[102] D. Reigosa, K. Akatsu, N. Limsuwan, Y. Shibukawa, and R. Lorenz, "Self-sensing comparison of fractional slot pitch winding versus distributed winding for FW- and FI-IPMSMs based on carrier signal injection at very low speed," *Industry Applications, IEEE Transactions on*, vol. 46, no. 6, pp. 2467–2474, 2010.

[103] S.-C. Yang and R. Lorenz, "Analysis of iron and magnet losses in surface-permanent-magnet machines resulting from injection-based self-sensing position estimation," *Industry Applications, IEEE Transactions on*, vol. 48, no. 6, pp. 1901–1910, 2012.

[104] J. Hu, J. Liu, and L. Xu, "Eddy current effects on rotor position estimation and magnetic pole identification of PMSM at zero and low speeds," *Power Electronics, IEEE Transactions on*, vol. 23, no. 5, pp. 2565–2575, Sept 2008.

[105] D. Reigosa, P. Garcia, F. Briz, D. Raca, and R. Lorenz, "Modeling and adaptive decoupling of high-frequency resistance and temperature effects in carrier-based sensorless control of PM synchronous machines," *Industry Applications, IEEE Transactions on*, vol. 46, no. 1, pp. 139–149, 2010.

[106] N. Bianchi and S. Bolognani, "Influence of rotor geometry of an interior PM motor on sensorless control feasibility," in *Industry Applications Conference, 2005. Fourtieth IAS Annual Meeting. Conference Record of the 2005*, vol. 4, 2005, pp. 2553–2560 Vol. 4.

[107] X. Wang, R. Kennel, W. Xie, and D. Gerling, "Analysis of losses in a novel IPMSM resulting from high-frequency injection for sensorless control," in *Sensorless Control for Electrical Drives and Predictive Control of Electrical Drives and Power Electronics (SLED/PRECEDE), 2013 IEEE International Symposium on*, Oct 2013, pp. 1–5.

[108] Z. Zhu, K. Ng, N. Schofield, and D. Howe, "Improved analytical modelling of rotor eddy current loss in brushless machines equipped with surface-mounted permanent magnets," *Electric Power Applications, IEE Proceedings* -, vol. 151, no. 6, pp. 641–650, Nov 2004.

[109] F. Deng, "Improved analytical modeling of commutation losses including space harmonic effects in permanent magnet brushless DC motors," in *Industry Applications Conference, 1998. Thirty-Third IAS Annual Meeting. The 1998 IEEE*, vol. 1, Oct 1998, pp. 380–386 vol.1.

[110] B-h curve. [Online]. Available: http://www.electronics-micros.com/electrical/b-h-curve/

[111] N. West and R. Lorenz, "Digital implementation of stator and rotor flux-linkage observers and a stator-current observer for deadbeat direct torque control of induction machines," *Industry Applications, IEEE Transactions on*, vol. 45, no. 2, pp. 729–736, March 2009.

[112] D. Luenberger, "An introduction to observers," *Automatic Control, IEEE Transactions on*, vol. 16, no. 6, pp. 596–602, Dec 1971.

[113] T. Batzel and K. Lee, "Electric propulsion with the sensorless permanent magnet synchronous motor: model and approach," *Energy Conversion, IEEE Transactions on*, vol. 20, no. 4, pp. 818–825, Dec 2005.

[114] H. Kim, "On-line parameter estimation, current regulation, and self-sensing for IPM synchronous machine drives," Ph.D. dissertation, University of Wisconsin-Madison, 2004.